

Abstract

KISS, MIKLOS ZOLTAN. Application of diffraction enhanced imaging for obtaining improved contrast of calcifications in breast tissue. (Under the direction of Dale E. Sayers.)

Diffraction enhanced imaging (DEI) has been used to study the improvements in image contrast of calcifications in breast tissue. This new imaging modality has the potential to greatly improve early detection of breast cancer, primarily due to its ability to utilize contrast mechanisms in the breast, which are not possible with existing radiographic methods. Of particular interest is the comparison of the image contrast of calcifications in breast tissue obtained using DEI to those obtained using conventional radiography. The presence of calcifications in breast tissue has been connected to breast cancer, but this relationship is not well understood. The purpose of this dissertation is to study the improvements in image contrast of calcifications in healthy as well as cancerous breast tissue when using synchrotron-based DEI compared to conventional synchrotron-based methods. Image contrast is in part determined by the capabilities of the detector in the imaging system, and this relation was used to determine the effect of the limits of spatial resolution on near-pixel-sized objects, both by experiment and by computer modeling. Consistent definitions for image contrast were presented and applied to test objects, followed by application to breast tissue specimens containing calcifications. In every case, images obtained using DEI exhibited higher image contrast than the corresponding images obtained using normal radiography. The ratio of these contrast values, called the DEI gain, was consistently larger than unity, indicating that DEI does indeed utilize additional contrast mechanisms, such as refraction and scatter rejection, in addition to absorption and provides support for the development of a clinical prototype.

Application of diffraction enhanced imaging for obtaining improved contrast of calcifications in breast tissue

by

Miklos Z. Kiss, B.S., M.S.

A dissertation submitted to the Graduate Faculty of
North Carolina State University
in partial fulfillment of the
requirements for the Degree of
Doctor of Philosophy

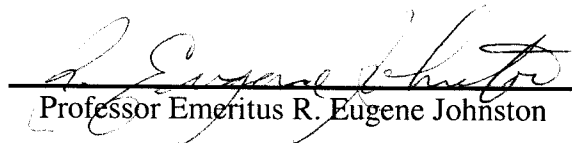
Physics

Raleigh, North Carolina
October 2002

Approved By:



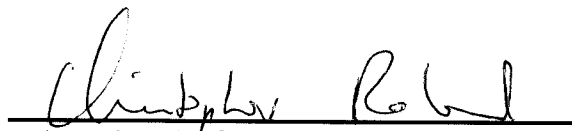
Professor Dale E. Sayers, Chair



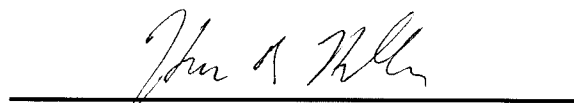
Professor Emeritus R. Eugene Johnston



Professor Mohammed Bourham



Associate Professor Christopher Roland



Associate Professor Hans Hallen

Know whether a problem is worth solving. There will always be dark days, but if your conviction of the value of the problem is such that you go right ahead in spite of the difficulties, the chances are that you will achieve success in the end.

- Charles F. Kettering

Biography

I was born on April 9, 1968 in New Haven, Connecticut. But in way, my story begins long before my life started. My parents both immigrated to the United States from Hungary in 1956 during the October Revolution. They came here to seek refuge, freedom, and liberty from the prevalent communist oppression in Hungary, which had been brought about by the filthy pigs that ran the Soviet Union. They actually met in the United States around 1960 – 61. Married since 1962, my parents have made an enjoyable life for themselves. My father, a former officer in the Hungarian Army (prior to the Revolution) spent 30+ years as a systems analyst and my mother was a media technician, working in the elementary school system in Cheshire, Connecticut, my hometown. Both of my parents are now enjoying retirement.

Growing up in the suburbs, my younger sister (Katalin Anna Kiss was born in 1970) and I had a happy childhood. But instead of playing Little League or junior football as most of my friends were, I was a competitive swimmer, a sport I competed in from 1975 to 1996. While I strove to be an outstanding athlete, I was driven by two major goals in my life: to be a soldier and a scientist. I realized very quickly that this was unusual. Most soldiers I have known had little to no desire to learn about science and the only exposure most scientists get to the military is through their DOD grants and what they might see on television. So, if I were going to succeed at both, it would take quite an effort. The desire to be a soldier must have been hereditary, since both my father and my grandfather were soldiers. From anecdotal accounts, it seems that at least one male from every generation of my ancestry has been a soldier. I also felt a moral obligation to serve my country. The United States had provided my parents freedom and opportunity to make a better life for themselves, neither of

which would have been available in the oppressive communist atmosphere of Hungary. So, I felt that I should give back to my country in return for what it had provided to my parents as well as for me. As for the science, Dad was (and is to this day) a voracious reader. His leisure reading lists includes physics textbooks, economical and philosophical treatises, history, and the occasional novel. His layman's interest in physics rubbed off on me and I discovered I had a passion for physics (though my grades may not have always reflected it!). So, I carefully set out to achieve both goals through the choices I made in high school and college.

I spent my time in high school trying to get into the service academies. Being a relative standout on the Cheshire High School Swim Team and academically in the upper echelon of my class, I thought I had a pretty good chance to get a Congressional appointment to West Point or Annapolis (at that point I hadn't ruled out service in the Navy). I was wrong. I didn't get an appointment, and my hopes were dashed. But, I also had not ruled out attending a regular college as well and decided on Worcester Polytechnic Institute in Massachusetts and majored in physics. As it turns out, I couldn't have made a better choice. While at WPI I tried to accomplish as much as I could. I majored in physics and also studied military science through the Army ROTC program. I was on the WPI Swim Team for four years and managed to be the leading scorer for the team for three years. Swimming provided an outlet when I wasn't studying.

I learned the hard way that a passion for physics is not enough. My academic performance for the first two years was barely above average and I struggled. But by my junior year things started to make better sense. WPI had a graduation requirement that all students spend a year working on a senior thesis, so I worked on a project to study the

focusing capabilities of an electromagnetic lens used for proton beams (for applications such as proton induced x-ray emission (PIXE)) under the tutelage of Professor Raymond Goloskie. I think it was during this time that I started developing an interest in the physics of imaging. So, as I finished my senior year, I thought about life after college. I had a commitment to the Army, but I decided to try to defer that by going to graduate school to get a Master's Degree. The Army said okay, and they deferred my commitment for two years and let me go to graduate school. Upon graduation from WPI, I was commissioned a Second Lieutenant in the Ordnance Corps.

Choosing a graduate school was an interesting challenge. In the end, I opted to go out to New Mexico State University in Las Cruces, New Mexico. The school had a great deal of appeal, in part because I had never been west of the Mississippi River. During the summer immediately after graduation from college, I received a call from the then head of the physics department, Professor George Goedecke. He asked me if I would be interested in working as a research assistant in an Army laboratory, which was located at nearby White Sands Missile Range (WSMR). I said yes and he put me in touch with Dr. Robert Sutherland, senior scientist in the US Army Atmospheric Sciences Laboratory (which is now defunct and its members have been reassigned throughout the US Army Research Laboratory). After a brief telephone interview, I decided that I would report to school early and start work at WSMR.

Dr. Sutherland introduced me to the world of Army science. He specialized in studying the optical properties of aerosols, especially in their use as obscurants on a battlefield. I was quickly put to work on the problem of modeling the light scattering properties of artificially generated fog. At the time, there was interest in the Army to create new forms of obscurants to better mask the battlefield from the enemy. Natural fog clearly

blocked out a large part of the electromagnetic spectrum, so we investigated the possibility of creating fog artificially and studying its electromagnetic radiation extinction capabilities.

After graduation from NMSU, I reported to Redstone Arsenal, Huntsville, Alabama, to attend the Officer Basic Course in the Ordnance Corps, where I learned the basics of being a platoon leader and ammunition management. There is a joke in the Army about ammunition. Every soldier should remember three things about ammunition: 1) the pointy end goes in first, 2) ammunition is heavy and will break your toes if you drop it, and 3) the government gets really upset if you lose it. The entire year of 1993 was spent in Taegu, Korea on my first assignment. I was the executive officer in the Headquarters Company of the 19th Support Command. The 19th SUPCOM was the major logistics support unit for the entire Korean Theater. I had fun on the job and found it interesting, even though I didn't get to do any physics. As the XO I was responsible for oversight of the dining facility, the motor pool, the arms room, and unit training. I even was promoted to First Lieutenant while I was there. I was also the acting company commander for a brief period because the regular company commander was fired for breaking some rules. In my free time, I coached the youth swim team at the base. Since many soldiers had their families with them, the children needed an outlet while out of school. Being on the swim team was one of these outlets and I volunteered my time.

Living in a foreign country was truly an eye-opening experience. Being immersed in culture unlike anything I had experienced before expanded my horizons. Along with this was the enormous responsibility put on my shoulders of being in charge of over 300 soldiers, from their job performance to ensuring their welfare. And coaching a swim team of about 20

children taught me a lot of patience. So, this tour was memorable and valuable for the life lessons I picked up.

After my tour in Korea was completed, I returned to the U.S. and headed to the Left Coast of the U.S., namely the state of Washington, where I spent the remainder of my active duty time at Fort Lewis. I served in logistics organizations, units whose mission was to provide logistics support for combat units. I had the opportunity to develop training exercises for our subordinate units and evaluate them on their wartime missions. I decided to come out of retirement from swimming and spent my free time competing in local swimming tournaments. My performances were well below what I had accomplished in high school and college, but I had a lot of fun doing it.

While I had a desire to serve my country and thoroughly enjoyed doing so, the call wasn't so loud that I wanted to be a career officer. I had every intention of returning to school to get a PhD. So, in mid-1995 I made the decision to leave active duty and apply for graduate school. Getting back into the grind of being a student was more challenging than I had expected, having been away from academia for four years.

But I survived the initial shock. While searching around for a research topic, I decided that I wanted to do some physics for which there was a direct benefit to society, as well as an opportunity to do some travelling and get some exposure. While reading through the department's publications, Dale Sayers' research interests piqued my curiosity and I went to speak to him. I was hooked. I was immediately taken by the variety of projects he was involved in and soon found a niche in the diffraction enhanced imaging (DEI) group. The DEI group was focusing its efforts on the early detection of breast cancer and this led to the dissertation contained herein.

Now that I have gotten to the other side of this hill, I can look around for a moment, and try to see where the path leads. The trials and tribulations I have gone through to get to this point are behind me (and the wounds are healing) and what lies ahead is shrouded in mist. But hopefully not for long...

Acknowledgments

The past six years have been turbulent to say the least. Completing a doctoral dissertation in physics is no small task in itself. It becomes daunting, with the occasional threat of being overwhelming, when the stress of troubling distractions are added in. So, I owe a debt of gratitude to a number of people, both professionally and personally, in helping me achieve this goal, which has been a dream since I was sixteen years old.

First and foremost, I would like to thank my advisor, Dale Sayers for his guidance, insight and near-infinite patience. As my advisor he gave a challenging and rewarding project to do, and taught me a lot of the nuances of physics that aren't found in a textbook, such as dealing with grant proposals, journal referees and conference chairmen, and how to look beyond the obvious results for the real essence of a problem. I would also like to thank my committee for their support and input: Drs. Gene Johnston, Mohammed Bourham, Christopher Roland, Hans Hallen, and Kuruvilla Verghese. Additionally, I would also like to acknowledge and thank other members of my research group, colleagues, and friends (in no particular order): Etta Pisano, Dean Chapman, Martin Yaffe, Chris Parham, Al Thompson, Dean Hesterberg, Elizabeth Rieg, Claudette Hathorne, and Jenny Allen. Finally, I would be remiss if I didn't mention my friend and colleague, Zhong Zhong at the National Synchrotron Light Source. He was also something of a mentor to me. When it came to running experiments and analyzing the data, Zhong's guidance and input were invaluable.

On the personal side, I could not have gotten through the past few years without the help of a few individuals. Working on the thesis was challenging enough, but my life was further complicated by a failed marriage. Recovering from that devastation could not have been possible without the love and support of my family; my parents, Jozsef and Ilona, and

my sister Kati, have stood by me and helped me in ways that only family members can. They never stopped believing in me and constantly offered words of encouragement both in dealing with my personal trials as well as the academic ones. Family is truly the most important thing. I would be in a world of shit if it weren't for them. There were others who had a part in my recovery. Dr. Grace Finkle was a great person to talk to and she helped me get back on my feet. I also owe a debt of gratitude to my friends, in particular, James Burnette, Dan McDevitt, David Pierson, and Vincent Woods for putting up with the worst I could be during this ordeal. After life returned to normal, I was blessed to have a wonderful person come into my life, my angel, Nooduan Muangsan (now Dr. Muangsan and a future renowned molecular biologist). Her love and devotion have made me a better person (and her incredible Thai cooking have made me a bigger person!). Finally, there are three people in my life without whom I would be lost. My dogs, Nova and Cosmo, and my cat Oreo have been my steadfast companions. They have given me so much and often made better companions than most humans.

A final note of acknowledgment is due to the organization that made this research possible. I was funded through the US Army's Breast Cancer Research Program, grant number DAMD-17-99-1-9329. But the Army has been more to me than just a source of funding. I have been associated with the Army my entire adult life. This association started as a cadet in Army ROTC at WPI. The research I did for my Master's Degree at New Mexico State University was carried out at the White Sands Missile Range and funded by the Army. Then I spent time in uniform and was an active member of the greatest military force in the history of civilization. So, being funded by the Army to do this dissertation only

seemed to fit a pattern of the past fifteen or sixteen years. I have been proud to serve in uniform and am thankful for the opportunities presented to me by them as a civilian.

Table Of Contents

List of Tables	xiv
List of Figures	xv
1. Introduction	1
1.1 Early Detection	2
1.2 Early Detection Technology	4
1.3 Calcifications in Breast Tissue	5
1.4 The Physics of Medical Imaging	7
2. Comparison of X-ray Detectors for a Diffraction Enhanced Imaging System	13
Abstract	13
2.1 Introduction	13
2.2 Theory	14
2.3 Experiment	15
2.4 Results	19
2.5 Conclusions	22
Acknowledgements	22
References	23
3. Measurement of Image Contrast Using Diffraction Enhanced Imaging	24
Abstract	24
3.1 Introduction	24
3.2 Theory	27
3.2.1 DEI Theory	27
3.2.2 Contrast and Gain	31
3.3 Methods	34
3.3.1 Computer Model Considerations	34
3.3.2 Experiment	38
3.4 Results and Discussion	40
3.5 Conclusions	47
Acknowledgements	47
References	48
4. Improved Image Contrast of Calcifications in Breast Tissue Specimens Using Diffraction Enhanced Imaging	50
Abstract	50
4.1. Introduction	50
4.2 Theory	52
4.3 Experiment	54
4.4 Results	56
4.5 Conclusions	64
Acknowledgements	65

References	65
5. Conclusion and a Look to the Future	68
6. Bibliography	70
Appendix A. IDL Code for Modeling DEI Images of Cylindrical Objects	75
A.1. Program DEI2D	75
A.2. Procedure TVSIZE	90
A.3. Function DOSHIFT	90
A.4. Function COLOR_VALUE	91
A.5. Function LORENTZ	92

List of Tables

Table	Page
1.1. Status of technologies used in breast cancer detection	4
2.1. Comparison of basic detector characteristics for the three detectors being considered	17
2.2. Results for dynamic range and dark noise effects	20
2.3. FWHM values for detector LSFs	21
3.1. Characteristics of samples used for imaging, listed by the real part of the refractive index ($n - 1$), linear attenuation coefficient, and density.	40
4.1. Summary of samples imaged	56
4.2. Statistical results for calcification size histogram (figure 4.5)	59
4.3. Slope values for regression lines in figures 4.6 – 4.7, and average gain values for figure 4.8.	62

List of Figures

Figure	Page
1.1. Medical imaging concept overview	8
2.1. Schematic of experimental apparatus at NSLS X-15A beamline	16
2.2. Natural logarithm of the image of the Lucite step wedge phantom taken at 20 keV using the Fuji system	17
2.3. Linearity response of the detectors measured at 20 keV.	17
2.4. Edge phantom for measuring the LSF and presampling MTF	18
2.5. Images from each detector taken at 20 keV	19
2.6. Comparison of LSFs for three detectors normalized to 1.	21
2.7. Comparison of the MTFs for the three detectors.	22
3.1. Ray trace through a cylindrical object of radius r	28
3.2. Normalized rocking curve for 18 keV x-rays on a 10-mm thick Si crystal at the [333] plane	29
3.3. Schematic representation of the DEI apparatus on the X-15A beamline at NSLS	39
3.4. Experimental images of Nylon wires and a Lucite cylinder	41
3.5. Vertical line profiles of the 6.35-mm diameter Lucite cylinder	42
3.6. Simulated images of Nylon wires and a Lucite cylinder at the same diameters as shown in figure 3.4	43
3.7. Graph of peak and radiographic contrast as a function of diameter-to-pixel-ratio	44
3.8. Signal-to-noise ratio plotted as a function of diameter-to-pixel ratio for refraction and radiograph	45
3.9. DEI gain as a function of diameter-to-pixel ratio	46
4.1. Schematic diagram of DEI imaging apparatus at beamline X-15A, National Synchrotron Light Source.	55
4.2. Images of sample 1.	57
4.3. Images of sample 2	57
4.4. Region of interest in sample 2 with corresponding line profiles.	58

4.5. Histogram of calcification size distribution.	59
4.6. Plot of image contrast as a function of calcification size.	60
4.7. Plot of SNR as a function of calcification size.	61
4.8. Plot of gain values as a function of calcification size.	63

1. Introduction

This dissertation is an investigation into a new imaging modality, diffraction enhanced imaging (DEI), and its application to screening mammography. DEI has the potential to greatly improve early detection of breast cancer, primarily due to its ability to utilize contrast mechanisms in the breast which are not possible with existing radiographic methods. Of particular interest is the comparison of the image contrast of calcifications in breast tissue obtained using DEI to those obtained using conventional radiography. The results suggest that contrast of calcifications are generally enhanced using DEI, thereby making them easier to detect than in a mammogram. This reinforces the notion that DEI may be a viable imaging modality, perhaps the future standard, in screening mammography.

In order to better understand how the contrast of calcifications may be enhanced, one should be aware of the importance of early detection of breast cancer and the relationship between calcifications in the breast with breast disease. This chapter covers both of these topics briefly, as well as an introduction into the concepts behind DEI and medical imaging. Any clinical mammography device utilizing DEI will require some sort of digital detector which has well-characterized attributes. Resolving small calcifications will be determined in part by the spatial resolution limits of the detector. Chapter two investigates some of the relevant features of a digital detector needed for DEI. Chapter three is a study on the ability of DEI to resolve small (pixel-sized or near-pixel-sized) objects of simple geometry. Consistent definitions for contrast were presented and applied to test objects. In chapter four, the definitions and analysis presented in chapter three are applied to DEI images of breast tissue specimens containing calcifications, and comparing the images to conventional radiographs. Chapter five is a summary and a look to the future of the development of DEI.

1.1. Early detection

The early detection of breast cancer has been gaining a great deal of attention in recent years. In 2002 approximately 203,500 American women will have been diagnosed with invasive breast cancer. The incidence rate had been increasing at about 4.5% per year in the 1980s, but the rate of increase has since slowed. Additionally, there will be 54,000 cases of in situ breast cancer (of these, approximately 88% will be ductal carcinoma in situ (DCIS)). Approximately, 39,600 women will die of breast cancer in 2002, second only to lung cancer in the number of deaths caused among women, and it is the leading cause of death among women between the ages of 40 and 55. One woman in eight will be diagnosed with breast cancer by their 85th birthday. It is also the most common non-skin related malignancy among American women (American Cancer Society). This is quite a chilling portrait of a killer. However, the situation is not all bad. Breast cancer mortality has been on the decline in recent years, largely due to early detection. The National Breast Cancer Foundation (NBCF) has stated that there has been a two-percent annual decrease in breast cancer deaths over the past decade. It has also stated that the 5-year survival rate for a positive early detection of breast cancer is 96%. Ongoing research may result in a cure for, or a method to prevent, breast cancer, but until then, it is widely believed that early detection is the best hope fighting this disease. While new techniques for imaging and early detection are being proposed, screening mammography remains the best method at this time (Nass et al, 2001).

Screening mammography is a successful means of assessing risk of breast cancer, but it is not without limitations. It is used to determine whether a woman possesses any abnormalities in her breasts that may be characteristic of a cancer, not to diagnose disease.

The overall goal is to reduce mortality due to breast cancer (Harris et al, 1996). In light of this, routine clinical trials resulted in a 25 to 30 percent decrease in breast cancer mortality among women between the ages of 50 and 70. A lesser benefit was seen in women between the ages of 40 and 49. For women over the age of 70, the lack of clinical trial data makes the determination of the benefit of screening mammography more difficult (Nass et al, 2001). Another limitation is that screening mammography cannot eliminate all deaths because it cannot detect all abnormalities. Mammograms from women with dense breasts are more likely to mask abnormalities associated with tumors, leading to a higher rate of false-positive and false-negative readings. Furthermore, the consistent production of high quality mammograms is technically challenging, and interpretation is subjective and variable among radiologists (Nass et al, 2001).

The successes and challenges of mammography continue. The current false-negative reading rate is around 10% (Singletary, 1999), and by one reckoning, up to 75% biopsies of suspicious breast lesions turn out to be benign (false-positive reading). Despite this, improvements in screening technology has resulted in a higher rate of detection in small abnormalities, such as DCIS. But the current methods of classification of such lesions and abnormalities as detected by mammography, and the ability to determine the potential of lethality of these lesions and abnormalities, are in need of improvement (Nass et al, 2001).

Table 1.1 Status of technologies used in breast cancer detection (adapted from MAB).

Technology	Current Status		
	Screening	Diagnosis	FDA approved for breast imaging/detection
Film-screen mammography (FSM)	3	3	Yes
Full-field digital mammography (FFDM)	2	3	Yes
Computer-aided diagnosis (CAD)	2	0	Yes
Ultrasound (US)	1	3	Yes
Novel US methods (compound, 3-D, Doppler, harmonic)	0	0	No
Elastography	0	0	No
Magnetic resonance imaging (MRI)	1	2	Yes
Magnetic resonance spectroscopy (MRS)	X/0 ^a	1/0 ^a	No
Scintimammography	0	1	Yes
Positron emission tomography	0	0	Yes
Optical imaging	0	1	No
Optical spectroscopy	X	0	No
Thermography	0	1	Yes
Electrical potential measurements	0	1	No
Electrical impedance imaging	0	1	Yes
Electronic palpation	0	NA	No
Thermoacoustic computed tomography, microwave imaging, Hall effect imaging, magnetomammography	NA	NA	No

Explanation of codes

^aEx vivo analysis of biopsy material/in vivo MRS

X - Technology is not useful

NA: Data are not available regarding use of the technology

0 - Preclinical data are suggestive that the technology might be useful for breast cancer detection, but clinical data are absent or very sparse

1 - Clinical data suggest that the technology could play a role in breast cancer detection, but more study is needed to define a role in relation to existing technologies

2 - Data suggest that technology could be useful in selected situations because it adds (or is equivalent) to existing technologies, but not currently recommended for routine use

3 - Technology is routinely used to make clinical decisions for the given application

1.2. Early detection technology

While screening mammography may be the current leading technology for early detection of breast cancer, the Food and Drug Administration FDA has approved other technologies for breast imaging. Table 1.1 summarizes these technologies.

It is possible that ideal detection performance may result from multimodality imaging, since a single modality is incapable of detecting all significant lesions. For example, the combination of ultrasound and MRI has shown potential, particularly for women with dense breasts. The combination of positron emission tomography (PET) with computed tomography (CT) has also shown some potential. There are a number of other technologies in earlier stages of development. But it is possible that improved imaging modalities may not ultimately lead to a reduction in breast cancer mortality and may lead to overtreatment of women (Nass et al, 2001). It is apparent that improvements in early detection are not without challenges. The recent appearance of DEI in the research arena has led some to believe that it may provide the best chance for improved detection without being hampered by physiological limitations such as dense breasts, breast compression, or dosage (Hempel, 2000). DEI does not appear in table 1.1 because it is still in its infancy as a modality and is not yet used in preclinical trials.

1.3. Calcifications in breast tissue

The link between calcifications and breast disease was first noted in 1951 by Leborgne (Leborgne, 1951). They have been linked to both benign and malignant processes and their composition and morphology are distinct for each. Morphology has been determined to be the most important element in the analysis of calcifications (Harris et al, 1996). This is because the shape of these particles is more apparent from a mammogram than the composition. Mammograms are non-specific for chemical composition, at least by current technology. Calcifications that form arc-like or rod-like structures are virtually always benign, as well as solid or lucent-centered spheres, and crescent-shapes. These calcifications are all typical 0.5 mm in diameter and larger. Benign calcifications are present

in breast tissue as the result of secretions into the acinar structures of the lobule or sedimentation of calcium onto the bottom of cysts formed by dilated acini. It is also possible to form a calcification by secretions around benign debris, which may collect in ducts.

Calcifications that are less than 0.5 mm in size and vary in shape are a cause for concern. Cancer-associated calcifications are either due to cellular secretion or to the calcification of necrotic cancer cells. They tend to form in the intraductal portion of the cancer. They are formed as cell necrosis occurs in the center of a duct. As cells near the center become hypoxic due to the increased distance from their blood supply, the calcifications form as very small and irregularly shaped particles (Harris et al, 1996).

The distribution of calcifications is indicative of the type of processes occurring. Calcifications associated with cancer form in nonspecific patterns. They tend to be arranged in clusters, but diagnosis of cancer is further hampered by the fact that these clusters can also lead to benign breast disorders such as hyperplasia or adenosis. Proper diagnosis after detection can only be accomplished through biopsy (Harris et al, 1996). Other distributions include segmental in which the calcifications are arranged along a single duct network and are a cause for concern. Finally, calcifications associated with benign processes tend to be randomly distributed throughout large volumes of the breast.

The chemical composition of calcifications is also important, but it cannot be easily be determined from a mammogram. Shape, size, and distribution can imply a certain composition as benign or malignant processes create calcifications of different calcium species. In general, there are two types of calcifications that have been identified. Type 1 calcifications, associated with benign processes, are colorless, birefringent, and are composed of calcium oxalate (CaC_2O_4) (Surratt, 1991). Type 2 calcifications are associated with both

malignant and benign processes. They too are birefringent, but basophilic and are composed of calcium phosphate, primarily hydroxyapatite ($\text{Ca}_5(\text{PO}_4)_3(\text{OH})$) (Surratt, 1991).

1.4. The physics of medical imaging

In order to understand conventional mammography and DEI, a foundation of the medical imaging must be first laid out. This section briefly covers the physics of medical imaging, DEI, and synchrotrons. Historically, Wilhelm Roentgen created the first medical image using x-rays in 1895 by exposing his wife's hand to an x-ray source and onto a photographic plate. Roentgen won the very first Nobel Prize for physics in 1901, "...for the discovery with which his name is linked for all time: the ... so-called Roentgen rays or, as he himself called them, x-rays" (Fenner et al, 1999). Imaging via x-rays once again reached Nobel status when Allan Cormack and Godfrey Hounsfield won the 1979 Nobel Prize in Physiology or Medicine for their development of computed tomography.

The basic principle of medical imaging is to exploit the contrast mechanisms of the object being imaged, so that it appears clearly against a background. There are several methods to image the human body, with each modality filling many applications. Table 1.1 showed the ones most common in mammography. The focus in this dissertation is x-ray based imaging. The conventional x-ray image is essentially a two-dimensional map of the attenuation by the object and surrounding tissue of x-rays. The more highly attenuating the object is, the fewer number of photons which will exposed the detector (film, image plate, CCD, etc.) directly behind it.

The ability of tissue to absorb or scatter an incoming x-ray can be expressed in terms of its probability to attenuate the photon per thickness of attenuator. This is referred to as the linear attenuation coefficient, μ , typically expressed in terms of cm^{-1} . In diagnostic energy

ranges, m varies inversely with energy, except at attenuation edges. Soft tissue has a μ , which ranges from ~ 0.35 - ~ 0.16 cm^{-1} for photon energies ranging from 30 to 100 keV (Bushberg, 1994). The relation between the attenuated intensity and the incident intensity is given by the well-known equation:

$$I = I_0 \exp(-\mu x) \tag{1-1}$$

where x is the path length of the x-rays through the tissue.

With this in mind, there are three basic concepts used to describe a medical image: contrast, spatial resolution, and noise. These fundamental concepts are tied together with intermediate concepts: the modulation transfer function (MTF), the Wiener spectrum, and the

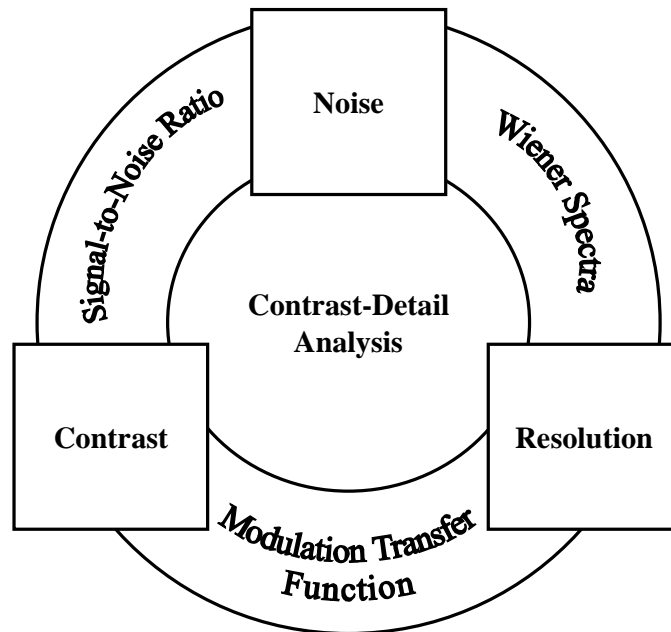


Figure 1.1 Medical imaging concept overview. Adapted from Hasegawa.

signal-to-noise ratio (SNR). Finally, at the center of it all is a unifying concept, called contrast-detail analysis. Figure 1.1 illustrates how these concepts are held together (Hasegawa, 1991).

The fundamental concepts are shown in three boxes, which are connected by the intermediate concepts. Contrast detail analysis lies at the center of the figure because it includes elements of all the surrounding concepts. These concepts will appear again in more detail in the proceeding chapters, but basic definitions are provided here. The spatial resolution of an imaging system is defined by the smallest distance that two objects can be separated and remain distinct. Noise can be regarded as the uncertainty with which a signal is recorded. In an imaging application this means that an image recorded using relatively few photons will be noisier than an image which is acquired using many more photons. Contrast is the difference in optical density between areas in a medical image. In a radiograph, there is high contrast between bone and soft tissue, but low contrast between a lesion such as lobular carcinoma and the surrounding breast tissue. Several factors comprise the radiographic contrast: chemical composition of the object, the technology used in acquiring the image, incident energy (or energy spectrum) of the x-rays, the presence of scattered x-rays, and the presence of a baseline signal in the imaging device (Hasegawa, 1991). The mathematical definition of image contrast is given by

$$C = \frac{\langle I \rangle - I_{object}}{\langle I \rangle}, \quad (1-2)$$

Where $\langle I \rangle$ is the average signal from the background, and I_{object} is the signal from the object, as measured by the detector. These basic concepts are tied together by the intermediate concepts. The modulation transfer function (MTF) describes the frequency response of the system. In other words, it measures how well the imaging system preserves the spatial modulation of an object. Signal-to-noise ratio is a measure of how well an observer can see an object in an image. The final intermediate concept is the Wiener spectrum, which

represents the level of noise as a function of the spatial frequency or spatial resolution in an image. Finally, the unifying concept of contrast-detail analysis is a study of how well an imaging system can resolve the smallest observable objects as a function of their contrast at given noise levels. This is a very simplified approach to the basics of medical imaging. The diagram borrowed from Hasegawa has been abridged to highlight the most relevant concepts here.

As mentioned in the previous section, there are several modalities available for use in mammography. One new modality currently being researched, which is absent from table 1.1 is DEI. DEI, as it will be seen throughout this dissertation, produces high contrast images with little or no degradation from scattered radiation. DEI first appeared in publication in 1997 (Chapman et al, 1997) and since then the collaboration has published a number of papers covering the subject and its application to mammography (Zhong et al, 2000, Pisano et al, 2000, Hasnah et al, 2002). It is hoped and expected that as more research is conducted with DEI, and its potential is fully realized, the mammography community will be put in a position to re-evaluate the standard modality for screening patients for breast cancer, with DEI emerging as the new standard. It is also the personal hope of the author that this dissertation somehow contributes to this goal.

References

American Cancer Society: <http://www.cancer.org>.

Baruchel J., Lodini A., Romanzetti S., Rustichelli F., Scrivani A., “Phase-contrast imaging of thin biomaterials,” *Biomaterials* **22** (2001) 1515 – 1520.

Bushberg J.T. Seibert J.A., Leidholdt E.M., Boone J.M., *The Essential Physics of Medical Imaging*. Philadelphia: Lippincott, Williams & Wilkins, 1994.

Carroll F.E., Waters J.W., Andrews W.W., Price R.R., Pickens D.R., Willcott R., Tompkins P., Roos C., Page D., Reed G., Ueda A., Bain R., Wang P., Bassinger M., “Attenuation of

monochromatic x-rays by normal and abnormal breast tissues,” *Investigative Radiology* **29** (1994) 266 – 272.

Chapman D., Thomlinson W., Johnston R.E., Washburn D., Pisano E., Gmür N., Zhong Z., Menk R., Arfelli F., and Sayers D., “Diffraction Enhanced x-ray Imaging,” *Phys. Med. Biol.* **42** (1997) 2015 – 2025.

Colonna S., D’Acapito F., Mobilio S., Onori S., Pugliani L., Romanzetti S., Rustichelli F., “Curved Optics for x-ray phase contrast imaging by synchrotron radiation,” *Phys. Med. Biol.* **46** (2001) 967-974.

Fenner R.B., Picologlou S., Shenoy G.K., Eds., *Nobel Prizes for X-ray Science*. Argonne National Laboratory: Advanced Photon Source, 1999.

Harris J.R., Lippman M.E., Morrow M., Hellman S. Eds., *Diseases of the Breast*. Philadelphia: Lippincott-Raven, 1996.

Hasegawa B.H., *The Physics of Medical X-ray Imaging, 2d ed.* Madison: Medical Physics Publishing, 1991.

Hasnah M.O., Zhong Z., Oltulu O., Pisano E., Johnston R.J., Sayers, D.E., Thomlinson W., Chapman D., “Diffraction enhanced imaging contrast mechanism in breast cancer specimen,” *Medical Physics*, **29** (2002) 2216 – 2221.

Hempel C., “Bright idea – scientists seek a better look at cancer,” *The News & Observer*, 17 April 2000, 1D.

Ingal V.N., Beliaevskaya E.A., Brianskaya A.P., Merkurieva R.D., “Phase mammography – a new technique for breast investigation,” *Phys. Med. Biol.* **43** (1998) 2555 – 2567.

Ishisaka A., Hiromu O., Honda C., “A new method of analyzing edge effect in phase contrast imaging with incoherent x-rays,” *Optical Review* **7** (2000) 566-572.

Keyrilainen J., Fernandez M., Suortti P., “Refraction contrast in x-ray imaging. *Nucl. Instr. and Meth. A*, **480** (2002) 419-427.

Kotre C.J., Birch I.P., “Phase contrast enhancement of x-ray mammography: a design study,” *Phys. Med. Biol.* **46** (1999) 2853 – 2866.

Nass S.J., Henderson C., Lashof J.C., eds., *Mammography and Beyond: Developing Technologies for the Early Detection of Breast Cancer*. Washington: National Academy Press, 2001.

National Breast Cancer Foundation: <http://www.nationalbreastcancer.org>.

National Synchrotron Light Source: <http://nslsweb.nsls.bnl.gov/nsls/Default.htm>.

Pisano E.D., Johnston R.E., Chapman D., Geradts J., Iacocca M., Livasy C.A., Washburn D.B., Sayers D.E., Zhong Z., Kiss M.Z., Thomlinson W.C., “Human Breast Cancer Specimens: Diffraction Enhanced Imaging with Histologic Correlation – Improved Conspicuity of Lesion Detail Compared with Digital Radiography,” *Radiology* **214** (2000) 895-901.

Singletary S.E., *Breast Cancer*. New York: Springer, 1999.

Surratt J.T., Monsees B.S., Mazoujian G., “Calcium oxalate microcalcifications in the breast,” *Radiology* **181** (1991) 141 – 142.

Warren, B.E., *X-Ray Diffraction*. New York: Dover, 1969.

Zachariasen, W.H., *Theory of X-Ray Diffraction in Crystals*. New York: Dover (1945).

Zhong Z., Thomlinson W., Chapman D., Sayers D., “Implementation of Diffraction Enhanced Imaging Experiments at the NSLS and APS,” *Nucl. Instr. and Meth. A*, **450** (2000) 556 – 567.

Chapter 2. Comparison of X-ray Detectors for a Diffraction Enhanced Imaging System



ELSEVIER

Nuclear Instruments and Methods in Physics Research A 491 (2002) 280–290

NUCLEAR
INSTRUMENTS
& METHODS
IN PHYSICS
RESEARCH
Section A

www.elsevier.com/locate/nima

Comparison of X-ray detectors for a diffraction enhanced imaging system

Miklos Z. Kiss^{a,*}, Dale E. Sayers^a, Zhong Zhong^b

^aDepartment of Physics, North Carolina State University, Box 8202, 27695 Raleigh, NC, USA

^bNational Synchrotron Light Source, Brookhaven National Laboratory, Upton, NY 11973, USA

Received 5 December 2001; received in revised form 21 May 2002; accepted 23 May 2002

Abstract

Three digital detector systems—a Fuji BAS2500 Image Plate Reader, a prototype charge-coupled device (CCD) from Mar USA and the MicroPhotonics XQUIS 1000 were compared with respect to format, dynamic range, dark noise, and spatial resolution. Experiments were conducted using highly collimated monochromatic X-rays at 20 keV, produced at the National Synchrotron Light Source. This study characterized digital detectors being considered for integration into a synchrotron-based diffraction enhanced imaging (DEI) apparatus used for medical imaging research, particularly mammography. These detectors are also being considered for integration into a proposed clinical prototype for DEI-based mammography. While all three systems had comparable image quality, the CCDs had faster readout time than the image plate system. However, the Fuji system had the largest dynamic range ($\sim 10^5$ compared to 10^4 for CCDs) and the largest active area. The MicroPhotonics XQUIS 1000 had the best spatial resolution as characterized by the point spread function. © 2002 Elsevier Science B.V. All rights reserved.

PACS: 07.05.Pj; 07.85.-m; 07.85.Fv; 07.85.Qe

Keywords: Digital detector; Image plate; CCD; Point spread function; Synchrotron; Modulation transfer function; Diffraction enhanced imaging

1. Introduction

Three detector systems have been characterized to determine their relative strengths and weaknesses for quantitatively recording X-ray images. With recent developments in Diffraction Enhanced Imaging (DEI) there is an initiative to integrate a digital detector into the imaging system [1–4]. As part of the effort to determine an

optimum digital detector for the system, a comparison between three detectors has been made. The effort has revealed certain limitations and challenges relevant to acquiring high quality radiographic images. This paper will give a brief discussion of relevant detector characteristics, specifications of the detectors studied, the results of the measurements, and the analysis. Similar studies comparing detectors have been conducted in the past [5–7], and several studies on new detectors for use in digital mammography have been published (for example, see Refs. [8–10]), but none with the express intent for evaluating them

*Corresponding author. Tel.: +1-919-515-5017; fax: +1-919-515-7331.

E-mail address: mzkiss@unity.ncsu.edu (M.Z. Kiss).

for integration into a DEI system. The other studies typically used conventional X-ray sources, while the results presented here used X-ray synchrotron radiation. Also, the detectors used in the other studies had also been optimized for full breast digital mammography, while this study centered on off-the-shelf technology for general scientific and medical research. As a result of this study, the criteria for digital detector systems for the synchrotron-based DEI system at the National Synchrotron Light Source (NSLS), and for a clinical prototype for DEI-based mammography are being refined.

The systems studied here were the Fuji BAS2500 Image Plate Reader, a prototype charge-coupled device (CCD) from Mar USA, and the Micro-Photonics XQUIS 1000. The detectors were compared with respect to overall image quality, dynamic range, dark noise, line spread function, and modulation transfer function, using highly collimated 20 keV X-rays produced at the X-15A beamline at the NSLS. While there are other parameters that determine the performance of a detector, such as the detective quantum efficiency (DQE) and noise power spectrum (NPS), this study was limited to the aforementioned parameters, because these were the most relevant for the high flux X-ray source used here.

Conventional digital radiography and other techniques such as digital subtraction angiography requires detectors with excellent spatial frequency-dependent DQE characteristics in order to resolve pixel-sized features or features low in contrast. Chapman et al. [1] report that the synchrotron-based DEI images of a mammography phantom from the American College of Radiography (ACR) have a contrast 27 times greater than in conventional synchrotron-based radiography images. Another group reports images of a carbon fiber 200 μm in diameter had about 8 times more contrast than its conventional radiographic counterpart [11]. This suggests that the spatial frequency characteristics of a detector are of particular importance because it is not well understood how these characteristics will affect the contrast in DEI images of pixel-sized (or near pixel-sized objects). Improvements in lesion detectability using conventional digital radiography

often involve the use of anti-scatter grids in the apparatus, as well as novel image-processing algorithms, all to compensate for limiting factors in contrast. The increased contrast in DEI arises from the refractive index gradient as well as absorption in the object and the inherent scatter-rejection, so there is a reduced demand in the use of anti-scatter grids and novel image processing techniques.

2. Theory

The detectors were compared with respect to dynamic range, dark noise, and spatial resolution. Each is discussed below. There are other criteria for judging a detector, which were not used in this study because they are not the most relevant in our current research efforts. Yaffe and Rowlands [12], among others, have discussed these in detail.

(a) *Dynamic range and dark noise*: The dynamic range of a detector can be defined as the ratio of the maximum usable signal of the detector (i.e., the highest signal level producing a linear response in the detector) to the detector noise, or

$$\text{DR} = \frac{I_{\text{max}}}{I_{\text{noise}}} \quad (1)$$

where I_{max} is the maximum usable signal of the detector and I_{noise} is the detector noise. I_{max} can also be taken as the saturation level. The detector noise comes from several sources, such as thermal noise, readout noise, background noise (e.g., dark current, residual noise, and device luminescence), and charge-transfer noise. For details on the various types of detector noise, the reader is referred to Janesick et al. [13]. The noise was measured by using the output of the detector with no incident X-rays. In the case of the image plate, this was accomplished by scanning the plate after it was erased but prior to any additional X-ray exposure.

(b) *Spatial resolution*: Spatial resolution is an important parameter of a detector. It determines how well an imaging system can detect very small objects. The classic definition of spatial resolution is related to the minimum separation distance between two objects such that they can be

distinguished from each other by the imaging system [14]. There are several methods for determining the spatial resolution. The method used here for processing the data is described by Hasegawa [15], and is summarized here. The point-spread function (PSF) of a detector defines the spatial resolution. In theory, the PSF is an image of an infinitesimal point object, but in practice it is difficult to measure. A good estimate of the PSF can be obtained in a practical manner. Instead of attempting to get an image of an infinitesimal point object, it is easier to obtain the Line Spread Function (LSF), which is a one-dimensional representation of the PSF. The LSF can be measured experimentally by one of two means. First, a narrow slit with a width much less than the detector's resolution ($< 10 \mu\text{m}$ wide in the current case) can be cut in an opaque sheet and imaged. The resulting image then approximates the LSF of the slit. The second method involves imaging an opaque edge. Obtaining the LSF by this method requires an intermediate step in its calculation, but it is much easier to carry out experimentally. The image formed on the detector by the opaque edge is called the edge-spread function (ESF), or edge response function (ERF). The LSF is then obtained by taking the derivative of the ESF. The full-width at half-maximum (FWHM) value of the LSF is approximately equal to that of the PSF and it is common to see the LSF used as an approximation for the PSF [16].

A second characteristic of the detector's spatial resolution is the modulation transfer function (MTF). It is a graphical representation of the resolution capabilities of an imaging system [14,15]. Mathematically, the MTF is expressed as the magnitude of the two-dimensional modulus of the Fourier transform of the PSF. The maximum spatial frequency that can be resolved is the Nyquist frequency at $f = (2d)^{-1}$, where d is the spacing of the detector elements [12]. An image containing spatial frequencies higher than the Nyquist frequency suffers from a condition known as aliasing, in which these higher components are translated below the Nyquist frequency. Care must be taken when experimentally determining the MTF to minimize the effects of aliasing [16,17]. A

good method for determining the MTF is discussed in the next section.

3. Experiment

Experiments were carried out at the X-15A beamline, at the NSLS, Brookhaven National Laboratory, Upton, New York. A diagram of the apparatus used in the experiment is shown in Fig. 1. White radiation from the synchrotron radiation source passed through a double crystal Silicon [1 1 1] Bragg monochromator and a series of slits that produced an imaging beam 1-mm high and 8-cm wide. For these measurements 20 keV X-rays were used. The energy resolution $\Delta E/E$ of the beam produced this way was 6×10^{-4} as determined from the Darwin width of the [1 1 1] crystal reflection and the opening angle of the incident beam. The imaging beam was monitored by an ionization chamber to measure the entry dose to the various phantoms used in the experiments. Lucite and aluminum absorbers were used to control the dose to the phantoms. A fast shutter system was used to control the exposure of the detector. The shutter opened when the scanning stage was at a constant velocity and was closed at the end of the scan range before the stage was slowed to a stop. The dose was additionally controlled by the scanning speed. The sample stage is located about 18 m from the X-ray source in the storage ring. The CCDs were located 1 m behind the sample stage while the image plate was fastened to the sample stage during image acquisition.

The Fuji BAS2500 Image Plate Reader uses a Fuji HR V image plate for acquisition. This plate is approximately 0.5 mm in thickness and is composed of a flexible plastic plate coated with a photostimulable phosphor (BaFBr:Eu^{2+}) combined with an organic binder. The image plate absorbs incident X-rays by ionizing some of the Eu^{2+} ions to Eu^{3+} . This liberates electrons to the conduction bands of the phosphor crystals. The electrons are then trapped in bromine vacancies, which were introduced in the manufacturing of the phosphor crystals. It can later be read out by visible radiation, which releases the trapped

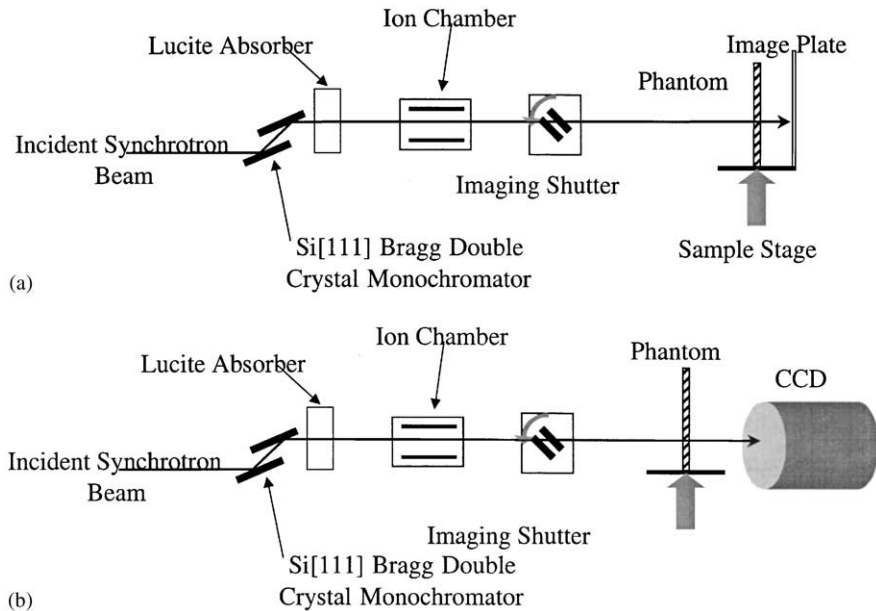


Fig. 1. Schematic of experimental apparatus at NSLS X-15A beamline (diagram is not to scale): (a) Arrangement for the image plate detector, (b) arrangement for the CCD detectors.

electrons back to the conduction band, converting the Eu^{3+} ions to Eu^{2+} ions and thereby emitting photostimulated luminescence (PSL) [19]. The intensity of the PSL is proportional to the absorbed radiation energy [19,20]. The PSL is then detected by a photomultiplier whose output signal is logarithmically amplified and digitized. The gain of the logarithmic amplifier, which determines the range of the latitude, and the photomultiplier sensitivity (high voltage) are scaled according to the exposure level and the image contrast [21]. The user can set the pixel size to either 50 or 100 μm . The gray level can be set as high as 16-bit and the dynamic range latitude and sensitivity can be varied as well. The values used in these experiments were 50 μm pixel size using 16-bit gray level with latitude=5 and sensitivity=4000. This reader converted raw intensities to the output data according to the following relation:

$$I_{\text{lin}} = \frac{4000}{S} 10^{L(I_{\text{raw}}/G-0.5)} \quad (2)$$

where L is the latitude, S is the sensitivity, and G is the number of gray levels (65,535 at 16-bit). The

image plate is a phosphor $20 \times 40 \text{ cm}^2$ in size. Raw images were $20 \times 25 \text{ cm}^2$, resulting in a 4000×5000 pixel digital image. The readout time for each image was about 5 min. The regions of the raw image containing useful data were extracted using image processing techniques and subjected to further investigation, while the remaining regions were discarded.

The second imaging device was a prototype CCD from Mar USA. The CCD chip is permanently bonded to a fiber optic taper, and has a 2048×2048 pixel layout, with each pixel 64.4 μm in size, and an image area of $131 \times 131 \text{ mm}^2$. This device also has a 16-bit gray scale and one frame can be read out in 10 s. The operating temperature was -78°C .

The final detector was the MicroPhotonics XQUIS1000. This device is also a bonded fiber-optic taper device. It has a 1024×1024 pixel layout with a pixel size of 50 μm . The image area was $51.2 \times 51.2 \text{ mm}^2$. The CCD has a 12-bit gray scale, but the frame grabber that is part of the system converts the data to a 16-bit format. The frame readout speed was about 0.1 s. For the experiments the device was operated at 10°C .

Table 1

Comparison of basic detector characteristics for the three detectors being considered

	Fuji BAS2500	Mar USA prototype	MicroPhotonics XQUIS 1000
Pixel size, μm	50	64.3	50
Pixel format, pixel	4000×5000	2048×2048	1024×1024
Image area, mm^2	200×250	131.7×131.7	51.2×51.2
Gray level	16-bit	16-bit	12-bit ^a
Readout time	5 min	10 s	0.1 s

^aThe MicroPhotonics CCD has a 12-bit gray scale, but the frame grabber that is part of the system converts the signal to a 16-bit format.

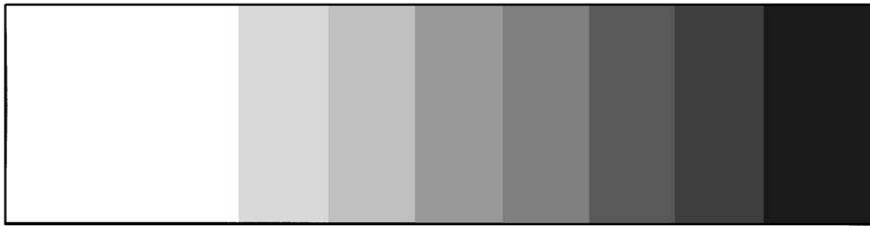


Fig. 2. Natural logarithm of the image of the Lucite step wedge phantom taken at 20 keV using the Fuji System. Three steps on the left-hand side of the phantom appear white due to saturation.

Table 1 summarizes the basic characteristics of the three detectors.

The dynamic range was measured by imaging a Lucite step wedge at 20 keV. The step wedge consisted of ten blocks of Lucite of varying thickness from 0.85 to 5.35 cm in 0.5-cm increments. Each step would then attenuate a uniform X-ray beam by a different amount. The incident radiation on the detector attenuated according to the well-known relation:

$$I(x) = I_0 e^{-\mu x} \quad (3)$$

where x is the thickness of each step of the wedge, μ is the linear absorption coefficient of Lucite (in cm^{-1}), and I_0 is the incident intensity. The average intensity (represented as a dimensionless quantity) in a 100×100 -pixel area (40×40 for the Mar CCD and MicroPhotonics CCD) over each step was plotted as a function of the step thickness. This revealed both the linear response regions for the detector as well as the saturation level. It was determined that the linear response extended up to the saturation level for all three detectors. Fig. 2 is the natural logarithm of an image of step wedge phantom recorded by the Fuji system. The three

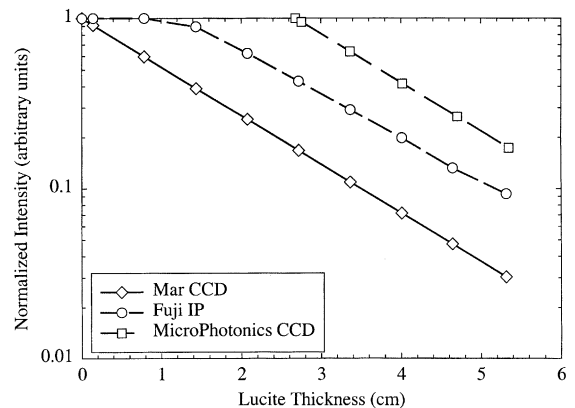


Fig. 3. Linearity response of the detectors measured at 20 keV. The vertical axis has been normalized to 1 (the saturation level) and is plotted against the thickness of the Lucite step wedge. Saturation was reached at approximately 3 cm for the MicroPhotonics CCD, while the Fuji image plate reached saturation at 1 cm, and the Mar CCD did not reach saturation for the X-ray intensities used in this experiment.

leftmost steps appear white due to saturation. This compares well with the plots in Fig. 3. This graph shows the normalized intensity as a function of step thickness on all three detectors at 20 keV

showing the linearity of the respective systems. Several data points are clustered at the top of the graph, indicating the minimum thickness of Lucite for which the detector was saturated. It can also be seen from the graph that each detector achieved saturation at a different thickness of Lucite. This is due to the individual characteristics of each detector. The MicroPhotonics CCD clearly has the highest saturation level and the Mar CCD has the lowest. In other words, the MicroPhotonics CCD requires a higher photon count to saturate it than the Mar CCD.

In order to compare the intensities from one detector to another, the data was converted to photons per pixel. This was achieved by measuring the average intensity of a 200×200 -pixel region on the detector. The following relation was used to determine the average number of photons incident on a pixel

$$N = A\Phi \frac{h_{\text{beam}}}{v} e^{-\mu t} \quad (4)$$

where A is the area of a pixel in mm^2 , Φ is the X-ray flux rate, measured in photons/ mm^2/s , h_{beam} is the beam height in mm, v is the scan speed of the stage holding the phantom in mm/s, μ is the attenuation coefficient of the phantom in cm^{-1} , and t is the Lucite thickness in cm. The response, R , by each pixel to N incident photons was then determined by dividing the average pixel value by N resulted in the average intensity generated by one incident photon on a pixel, or

$$R = \frac{I_p}{N} \quad (5)$$

where I_p is the signal generated in a pixel responding to N incident photons. Since the number of photons incident on a pixel was determined by the step thickness, the saturation level could be determined by observing the steps for which the intensity was a constant. Thus, the saturation level intensity could be converted into a number of photons per pixel.

Detector noise for the CCDs was measured by reading out the detector after an exposure time from 1 to 100 s. Measuring the noise level in the Fuji system was accomplished by reading out a blank image plate at the standard settings (latitude = 5, sensitivity = 4000). The blank image plate

was “erased” prior to readout by exposing it to fluorescent lights for 5 min. The plate eraser is part of the Fuji system. The noise was defined as the standard deviation of the pixel value in a 200×200 -pixel region on each detector. This too was converted using the above procedure into photons per pixel. The two numbers were then applied to Eq. (1) to obtain the dynamic range.

The method used for measuring the ESF, LSF, and the pre-sampling MTF is the knife-edge technique for digital devices adapted from Refs. [17,18,22], and is summarized here. The ESF was measured by masking a Lucite sheet with Pb tape, and imaging it at 20 keV. The edge was aligned slightly off perpendicular to the scan direction ($1-9^\circ$), so that the location of the edge shifted from one scan to the next. The “angulated” knife-edge target improves the sampling rate and reduces the effects of aliasing [22]. Fig. 4 shows diagrams of

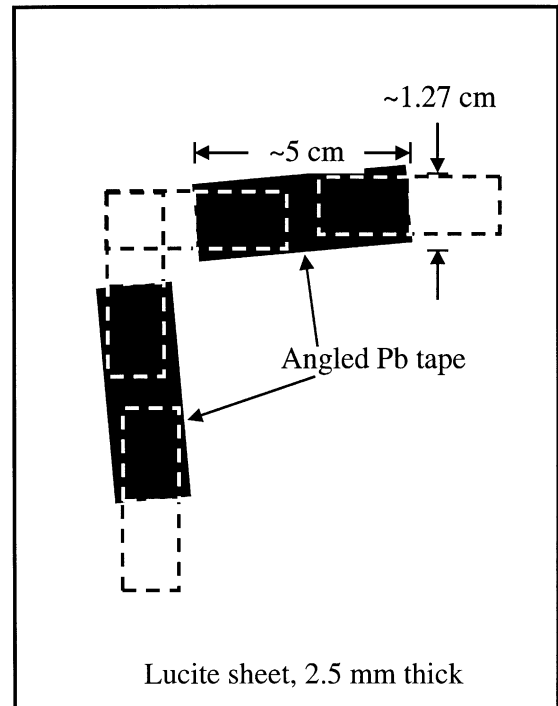


Fig. 4. Edge phantom for measuring the LSF and presampling MTF. Horizontally and vertically oriented pieces of lead tape were affixed to a Lucite sheet and imaged. The boxed regions (----) indicate where the ESF was obtained.

the so-called edge phantom. In processing the data from each set of scans, a composite ESF was created by the superposition of several scan lines. This served to reduce the effective sampling interval to a fraction of the pixel size according to the relation $\Delta x' = \Delta x \tan \theta$, where Δx is the pixel size and θ is the angle between the scan direction and the edge. The noise in the composite scan was suppressed by smoothing and resampling. The LSF was determined in both the horizontal and vertical directions by taking a derivative of the smooth composite scan. For each direction, several scans were averaged together (3–8), and the MTF was then obtained by applying a FFT to the LSF. Care was taken to limit the leakage of frequency components from adjacent bins by applying a Hanning window to the data [16].

It has been noted that the knife-edge technique has some inherent challenges, which may effect the results of the MTF [17,18], namely the need to take a derivative of the ESF and to smooth the result. Small fluctuations in the ESF can result in large errors when determining the LSF. Smoothing and resampling corrects these errors at the expense of loss of frequency resolution and may introduce aliasing. But for the purposes of estimating detector performance the errors due to these effects were deemed acceptable [18].

4. Results

Fig. 5 is a qualitative comparison of the three detectors using a section of a digital mammography phantom from the International Digital

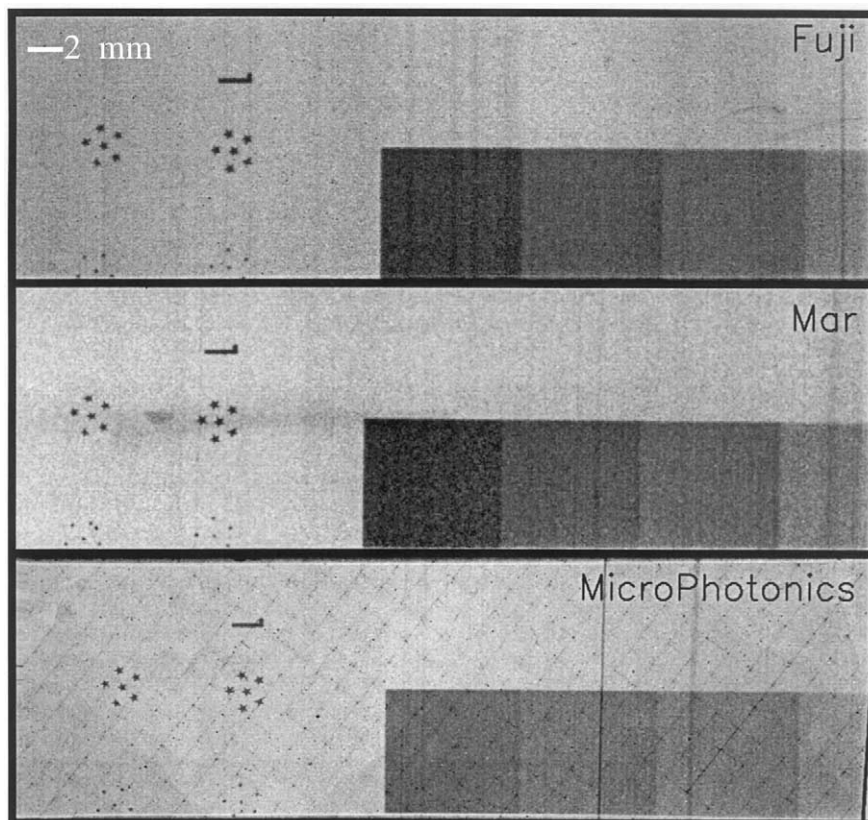


Fig. 5. Images from each detector taken at 20 keV. The images depict a section of the IDMDG digital mammography phantom. Star patterns represent clusters of microcalcifications of various sizes.

Mammography Detector Group (IDMDG). The left-hand side of each image shows clusters of star-shaped simulated microcalcifications, and the lower right shows part of a gray scale. The phantom was exposed to 20 keV X-rays for each detector and the images are displayed with post-processing being limited to histogram clipping and gamma correction. The Fuji and MicroPhotonics images are each 1024×310 pixels while the Mar image was originally 800×242 pixels but it has been scaled to the same size as the other two. A direct consequence of the minimal image post-processing is the overall apparent graininess of the images. Vertical streaks are visible in each image as well as the nonuniformity of the background intensity in the horizontal direction. The vertical streaks have been attributed to multiple scattering by the monochromator crystal and the Be window on the X-15A. Multiple scattering is the result of X-rays, which have been diffracted off crystal planes other than the [111], due to slight misalignment in the monochromator crystals. Some images (not shown) have exhibited nonuniform brightness in the vertical direction as well, due to periodic oscillations of the translation stage, or instability of the beam. In practice, nonuniformities are removed in image post-processing. Also visible in the MicroPhotonics image is a checkerboard grid, which is actually part of the CCD system. This too can be removed during post-processing of the image.

In the time since these experiments have been conducted, improvements have been made to the apparatus to reduce these artifacts. A good

benchmark for the detectors is how well they rendered the simulated calcifications in the left-hand side of each image. The MicroPhotonics system presents the sharpest results. The Mar system also reproduces the calcifications well, particularly when compared to the Fuji system. The blurriness of the calcifications in the Fuji image is consistent with the large broadening of the LSF (see below). The gray scale in the lower right of each image as well as the overall brightness varies as well. The differences are in part, the result of different skin entry doses used on the phantom, ranging from 300 mrad for the Fuji up to 1200 mrad for the MicroPhotonics system.

Results for the dark noise and dynamic ranges for the dynamic ranges for the three detectors are shown in Table 2. The dark noise of the detectors was measured, with the X-ray off, using various exposure times. The dark noise for the Fuji system was independent of exposure time, indicating that it came from the readout process, not from accumulation by the image plate. For the two CCD detectors, dark noise increased slightly with exposure time, due to accumulation of CCD leakage current. The Mar detector's CCD was cooled to -78°C , resulting in very small increase of dark noise with exposure time. The dark noise levels measured with 10-s exposure time, typical for a DEI image acquisition, were used to calculate the dynamic range of the detectors. The Fuji system clearly has the largest dynamic range and has very low dark noise levels in part to it being optimized for medical research applications. The MicroPhotonics CCD had the lowest dynamic

Table 2
Results for dynamic range and dark noise effects

	Integration time (s)	Noise (photon/pixel)	Dynamic range
Mar CCD	1	0.7303	6.4×10^4
Saturation level:	10	0.7815	6.0×10^4
47×10^3 photon/pixel	100	0.8430	5.5×10^4
MicroPhotonics CCD	1	53.84	1.5×10^3
Saturation level:	10	63.60	1.3×10^3
81×10^3 photon/pixel	100	182.85	0.5×10^3
Fuji IP	($L = 5, S = 4000$)	0.101	1.4×10^5
Saturation level:			
14×10^3 photon/pixel			

range, but this is consistent with the 12-bit acquisition of the CCD.

The comparison of LSFs for all three detectors in both the horizontal and vertical directions is shown in Fig. 6, and Table 3 summarizes the FWHM values. The MicroPhotonics system clearly had the narrowest LSF, with a FWHM value of $105\ \mu\text{m}$ in the horizontal direction and $98\ \mu\text{m}$ in the vertical direction. The Mar CCD prototype had the broadest LSF, with a FWHM value of $154\ \mu\text{m}$ in the horizontal direction and $173\ \mu\text{m}$ in the vertical direction. It is important to note that when comparing the LSF in terms of pixel size, the Mar CCD shows a better result than the Fuji image plate, since its pixel size was larger than that of the image plate system. The widths of the LSFs are approximately 2–3 times the pixel

size. In the case of the image plate, broadening of the LSF is due to the fact that ion traps are located throughout the phosphor, requiring the readout laser to penetrate the phosphor. This results in scattering of the light, in which ion traps are released in a larger image area than the size of the incident laser beam [12]. For the CCDs the reduction in spatial resolution can be due to low transfer efficiency. That is, as the signal is shifted across many pixels as it is being read out, low transfer efficiency will smear out the image in the readout direction [12,22].

Results for the normalized MTF are shown in Fig. 7. It is clear from the graph that the MicroPhotonics system has the best MTF. This can actually be implied from the LSF, since a narrower peak would have a broader Fourier

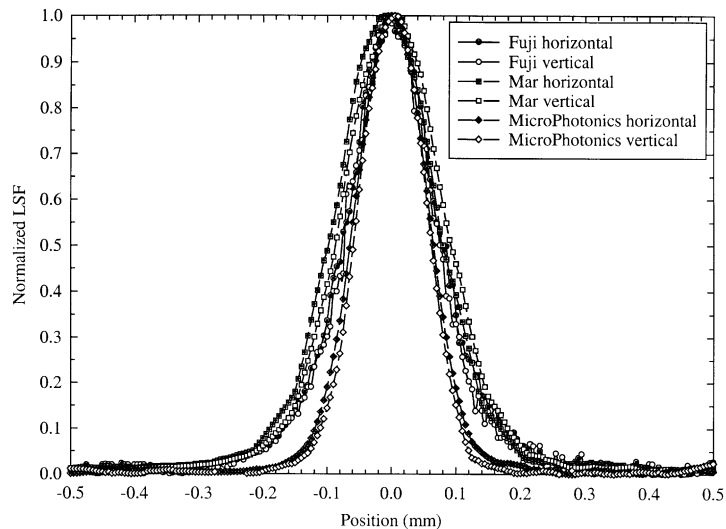


Fig. 6. Comparison of LSFs for three detectors normalized to 1. The data was collected at 20 keV.

Table 3
FWHM values for detector LSFs

Detector	Horizontal FWHM (μm)	Horizontal FWHM (pixels)	Vertical FWHM (μm)	Vertical FWHM (pixels)
Mar CCD	155 ± 8	2.4 ± 0.1	154 ± 5	2.4 ± 0.1
MicroPhotonics CCD	105 ± 2	2.10 ± 0.04	98 ± 3	2.0 ± 0.02
Fuji IP	145 ± 1	2.9 ± 0.1	138 ± 1	2.8 ± 0.1

Detector LSFs were measured at an energy of 20 keV. The FWHM in pixels is obtained by dividing the FWHM in μm by the pixel sizes given in Table 1. Uncertainties are one standard deviation from the average value.

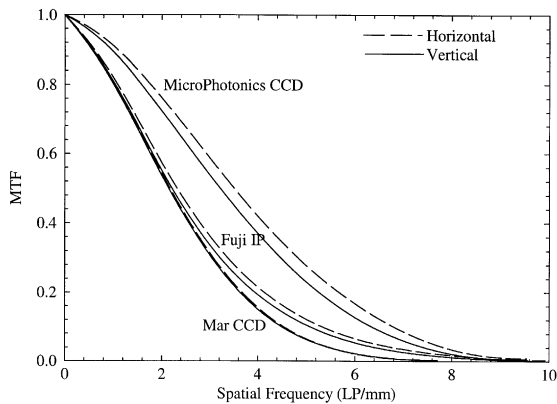


Fig. 7. Comparison of the MTFs for the three detectors. Data for the Mar CCD extends out only to about 8 LP/mm since it has a lower Nyquist frequency than the other two (7.76 LP/mm compared to 10 LP/mm).

transform than a wide peak. The MTFs for both the MicroPhotonics and Fuji systems go to zero at 10 LP/mm, the Nyquist frequency for those two detectors. The Mar system goes to zero at 7.76 LP/mm, its Nyquist frequency.

5. Conclusions

This study has characterized digital detectors being considered for integration into a synchrotron-based mammographic research program, as well as for a proposed clinical prototype for DEI-based mammography. A visual comparison of images generated by each detector suggests that the MicroPhotonics system had the best image quality, even with the presence of the grid and its lowest dynamic range. The Fuji system performed very well and is a reliable detector and has continued to fulfill the imaging needs at the X-15A beamline. It had the best dynamic range and the largest active area. This is a far larger active area than in either CCD. It was also the only detector studied that had been developed specifically for medical imaging applications. But it suffered from having a poorer MTF when compared to the MicroPhotonics CCD, which had the same pixel size, and the readout time was the longest of the three. The CCDs also

performed well. Clearly, the MicroPhotonics system had the best spatial resolution but its active area and dynamic range were limiting factors. The Mar CCD also performed well. It had a good dynamic range and spatial resolution qualities. As indicated, this was a prototype device and Mar currently markets a production model of this system. However, it had the largest pixel size, and its active area also would preclude it from being used for full-field digital mammography.

While this study did not result in a choice for a detector system for integration, it has provided an indication of certain performance standards for such a detector. Spatial resolution will continue to be one of the most important criteria because future efforts will concentrate on modeling DEI imaging of lesions, spiculations, clusters of microcalcifications. These effects provide unique challenges to the detectors acquiring the images. By modeling the imaging characteristics and conducting subsequent imaging experiments, the requirements of a detector will be fully realized.

Acknowledgements

The authors wish to thank G. Allan Johnson of the Duke University Center for In Vivo Microscopy for use of the MicroPhotonics CCD, Darren O'Connor of North Carolina State University for assistance in taking data, and Etta Pisano and Gene Johnston of the Department of Radiology, University of North Carolina-Chapel Hill, Mark Williams of the Department of Radiology, University of Virginia and Martin Yaffe of the Sunnybrook and Women's College Health Sciences Center, University of Toronto, for helpful discussions and suggestions. This work was supported in part by US Army grant DAMD 17-99-1-9329 and US DOE grant DE-AC02-76CH00016. This research has been carried out (in part) at the National Synchrotron Light Source, Brookhaven National Laboratory, which is supported by the US Department of Energy, Division of Materials Sciences and Division of Chemical Sciences.

References

- [1] D. Chapman, W. Thomlinson, R.E. Johnston, D. Washburn, E. Pisano, N. Gmür, Z. Zhong, R. Menk, F. Arfelli, D. Sayers, *Phys. Med. Biol.* 42 (1997) 2015.
- [2] E.D. Pisano, R.E. Johnston, D. Chapman, J. Geradts, M. Iacocca, C.A. Livasy, D.B. Washburn, D.E. Sayers, Z. Zhong, M.Z. Kiss, W.C. Thomlinson, *Radiology* 214 (2000) 895.
- [3] Z. Zhong, W. Thomlinson, D. Chapman, D. Sayers, *Nucl. Instr. and Meth. A* 450 (2000) 556.
- [4] D. Chapman, E. Pisano, W. Thomlinson, Z. Zhong, R.E. Johnston, D. Washburn, D. Sayers, K. Malinowska, *Breast Dis.* 10 (3,4) (1998) 197.
- [5] E.F. Eikenberry, M.W. Tate, D.H. Bilderback S.M. Gruner, X-ray detectors: comparison of film, storage phosphors and CCD detectors, in: B.L. Morgan (Ed.), *Photoelectronic Image Devices 1991*, IOP, London, 1991.
- [6] K.-W. Jee, L.E. Antonuk, Y. El-Mohri, M. Maolinbay, Q. Zhao, Evaluation of direct detection and indirect detection active matrix flat-panel imagers (AMFPIs) for digital mammography, in: L.E. Antonuk, M.J. Yaffe (Eds.), *Medical Imaging 2001: Physics of Medical Imaging*, SPIE, San Diego, CA, 2001.
- [7] S. Vedantham, A. Karellas, S. Suryanarayanan, D. Albagli, S. Han, E.J. Tkaczyk, C.E. Landberg, B. Opsahl-Ong, P.R. Granfors, I. Levis, C.J. D’Orsi, R.E. Hendrick, *Med. Phys.* 27 (3) (2000) 558.
- [8] P.R. Granfors, R. Aufrechtig, *Med. Phys.* 27 (6) (2000) 1324.
- [9] M.B. Williams, L.L. Fajardo, G.P. Otto, J.M. Tran, *RSNA Electron. J.* 1 (1997); <http://ej.rsna.org/Ej.0.96/0020-96.fin/ms.htm>.
- [10] L.E. Antonuk, M.J. Yaffe (Eds.), *Medical Imaging 2001: Physics of Medical Imaging*, SPIE, San Diego, CA, 2001.
- [11] S. Colonna, F. D’Acapito, S. Mobilio, S. Onori, L. Pugliani, S. Romanzetti, F. Rustichelli, *Phys. Med. Biol.* 46 (2001) 967.
- [12] M.J. Yaffe, J.A. Rowlands, *Phys. Med. Biol.* 42 (1997) 1.
- [13] J.R. Janesick, T. Elliot, S. Collins, M.M. Blouke, *Opt. Eng.* 26 (8) (1987) 692.
- [14] J.T. Bushberg, et al., *The Essential Physics of Medical Imaging*, Williams & Wilkins, Baltimore, 1994, p. 749.
- [15] B.H. Hasegawa, *The Physics of Medical X-ray Imaging*, 2nd edition, Madison Physics Publishing, Madison, 1991.
- [16] S.W. Smith, *The Scientist and Engineer’s Guide to Digital Signal Processing*, 2nd edition, California Technical Publishing, San Diego, CA, 1999.
- [17] H. Fujita, D.-Y. Tsai, T. Itoh, K. Doi, J. Morishita, K. Ueda, A. Ohtsuka, *IEEE Trans. Med. Imaging* 11 (1) (1992) 34.
- [18] E. Samel, M.J. Flynn, *Med. Phys.* 25 (1) (1998) 102.
- [19] Y. Amemiya, J. Miyahara, *Nature* 336 (3) (1988) 89.
- [20] Y. Amemiya, *Synchrotron Radiat. News* 3 (2) (1990) 21.
- [21] F. Arfelli, C. Burns, D. Chapman, N. Gmür, R.E. Johnston, R. Menk, E. Pisano, D. Sayers, W. Thomlinson, D. Washburn, Z. Zhong, Data acquisition and analysis of mammography images at the NSLS June–August 1995, National Synchrotron Light Source, Brookhaven National Laboratory, 1995, p. 21.
- [22] S.E. Reichenbach, S.K. Park, R. Narayanswamy, *Opt. Eng.* 30 (2) (1991) 170.

Chapter 3. Measurement of Image Contrast Using Diffraction Enhanced Imaging

A modified version of this chapter has been submitted as a paper for publication in *Physics in Medicine and Biology*.

Abstract

Refraction contrast of simple objects obtained using diffraction enhanced imaging (DEI) was studied and compared to conventional radiographic contrast. Lucite cylinders and nylon wires were imaged using monochromatic synchrotron radiation at the National Synchrotron Light Source at the Brookhaven National Laboratory. The DEI images were obtained by placing a silicon analyzer crystal tuned to the [333] diffraction plane in the beam path between the sample and the detector. To compare the DEI images with conventional radiographic images requires a consistent definition of refraction and absorption contrast. Conventional definitions of contrast favor conventional radiography, and DEI contrast is defined to emphasize the specific characteristics of DEI. The proposed definitions were then used to find the DEI gain (the ratio of the DEI contrast with respect to the conventional image contrast). The results presented here show that the DEI gain is consistently greater than one, indicating that DEI provides more contrast information than conventional radiography.

3.1 Introduction

In order to make quantitative comparisons between normal radiography and DEI, systematic definitions of the contrasts used in each technique must be developed. Several reports on the enhanced contrast of objects using DEI or phase contrast imaging have been published recently (Chapman et al, 1997, Pisano et al, 2000, Zhong et al, 2000, Colonna et al, 2001, Kotre and Birch, 1999, Ingal et al, 1998, Ishisaka et al, 2000, Baruchel et al, 2001,

Keyrilainen et al, 2002, Hasnah et al, 2002). However, none of the reports actually compare contrast values of DEI and conventional radiography in a quantitative way. The definition of DEI contrast is an important step in understanding the imaging mechanisms in DEI. These results can be used to quantify earlier results that, showed DEI images obtained using synchrotron radiation exhibited increased edge enhancement and improved signal-to-noise through reduced scattered radiation, when compared to images obtained using synchrotron-based conventional radiography (Chapman et al 1997, Pisano et al, 2000, Hasnah et al, 2002).

This study is part of an effort to develop DEI as viable imaging modality in mammography. Images obtained using DEI possess higher contrast when compared to conventional radiography. This contrast is due to the ability of DEI to exploit several contrast mechanisms, such as refraction (leading to edge enhancement), scatter rejection, and absorption, while conventional radiography derives its contrast from only absorption. In a conventional mammogram, objects such as calcifications and spiculations can be difficult to distinguish from the surrounding soft tissue. Photon scatter may further compound the problem. DEI has a demonstrated ability to filter out much of this scatter, thereby improving the signal-to-noise ratio as well as the contrast. Conventional mammography relies on collimators or anti-scatter grid to filter out the noise due to scatter, or via secondary image processing.

The application of DEI to imaging breast tissue specimens (Pisano et al, 2000, Hasnah et al, 2002) was successful in that it showed improved contrast of breast tissue specimens containing spiculations and other large lesions associated with breast cancer. For example, Pisano et al reported that 86% of the cases investigated showed enhanced visibility

of surface spiculations that had direct correlation with histopathologic information, and, Hasnah et al report that DEI images (acquired using the peak reflectivity of the analyzer crystal) exhibited 8 – 33 times higher contrast than normal radiographs. The next logical step would be to investigate calcifications in breast tissue.

The presence of clusters of calcifications in breast tissue has been connected to breast cancer (Fandos-Morera et al 1988, Galkin et al, 1977, Suratt et al, 1991, Olson et al, 1988, Radi, 1989, Winston et al, 1993, Galkin et al, 1982). It is believed that current mammographic limits can be improved upon by using DEI in order to enhance detection of smaller calcifications. Improvements to the early detection of breast disease depend partly on the conspicuity of calcifications in screening mammograms. Suspicious calcifications can range in size $< 50 - > 300 \mu\text{m}$ (Winston et al, 1993). Many of these calcifications may not be detected in mammograms because their image contrast is too low. Therefore, the current study investigates the ability of DEI in resolving small (near-pixel-size) objects and compares the results to conventional radiography. It is intended that the lessons learned here will be applied to breast tissue specimens containing calcifications associated with malignancies as well as benign processes.

The experiments were carried out at the X-15A beamline at the National Synchrotron Light Source (NSLS), Brookhaven National Laboratory, Upton, New York using monochromatic synchrotron radiation to obtain DEI images and conventional radiographs of weakly absorbing cylindrical objects. The conventional radiographs and the DEI images were compared with respect to their contrast. The conventional radiographic contrast has a simple definition (Hasegawa, 1991). This definition does not allow a direct comparison with DEI contrast since they are based on different contrast mechanisms. Until now, the

quantitative definition has not been applied to DEI in a meaningful way. The well-known contrast relation and how it relates to DEI are stated below, and comparisons between the conventional contrast and the DEI contrast are made using these relations. While the definition of contrast is a fairly general one and can be used to evaluate images acquired by any means, the results and conclusions stated here are specific to DEI.

In this paper, a model for forming images of a cylindrical object by the DEI method is presented. Image formation starts with ray tracing x-rays from the source to the detector. An algorithm is developed which accounts for the finite source size, detector point spread function (PSF), and the rocking curve of the analyzer crystal. The algorithm is used to create a computer model of the images created by the phantom. Two sets of comparisons are made. First, comparisons between the conventional radiographic images and the DEI images are made. Second, the experimental results are compared to the simulations.

It should be noted that this model represents a fairly simple system. The objects were imaged against a uniform background. In biomedical applications such as mammography, the environment is not so simple. However, this present study is a necessary step for a systematic evaluation of the application of DEI to mammography. DEI studies of calcifications have recently been completed and will appear in a future article.

3.2 Theory

3.2.1 DEI Theory

In a DEI experiment, x-rays from a synchrotron pass through a double crystal monochromator which selects the x-ray energy required. These monoenergetic x-rays then traverse a sample and undergo diffraction by a Bragg analyzer crystal, and are finally recorded at a detector. While the x-rays traverse the sample they may undergo refraction due

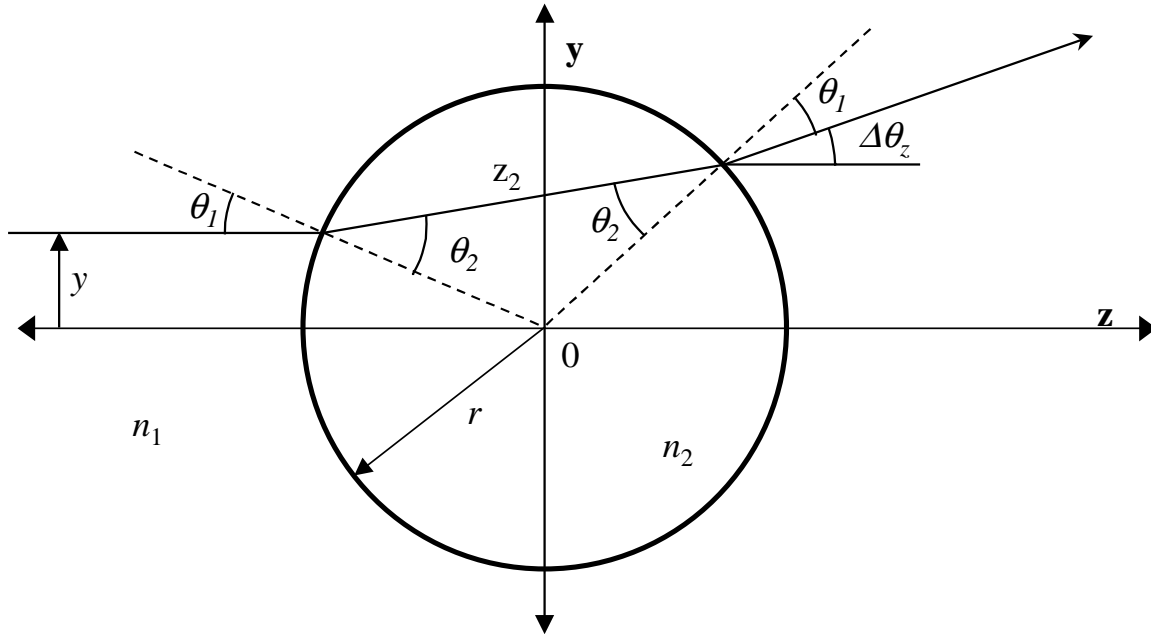


Figure 3.1. Ray trace through a cylindrical object of radius r . An incident beam in air (refractive index n_1) impinges on a cylindrical object of refractive index n_2 at a height, y , above the horizontal diameter of the cylinder and an incident angle θ_1 with respect to the surface normal. The refraction angle inside the cylinder is θ_2 and the path length in the cylinder is z_2 . The ray emerges on the far side of the cylinder at an angle $\Delta\theta_z$ with respect to the horizontal.

to refractive index gradients present in the sample. This causes the x-rays to change direction by a small amount, $\Delta\theta_z$. For the x-ray energies and samples used here, this deflection angle is on the order of microradians. The x-rays will also be attenuated by $\exp(-\mu x)$, where μ is the x-ray absorption coefficient along the path in the sample of length x , and may also undergo scattering at larger angles (i.e., greater than several microradians).

The important feature of a DEI apparatus is the analyzer, a perfect diffraction crystal which can be tuned to various angles. This crystal can almost completely eliminate radiation scattered by the sample, since only x-rays aligned within the angular acceptance angle of the analyzer will be diffracted onto the detector. The angular acceptance angle is known as the rocking curve (Chapman et al, 1997, Zachariasen, 1945). When the analyzer is tuned to the full width half maximum (FWHM) position on either side of the peak of the rocking curve (hereafter referred to as the low angle side or the high angle side), the intensity of the beam

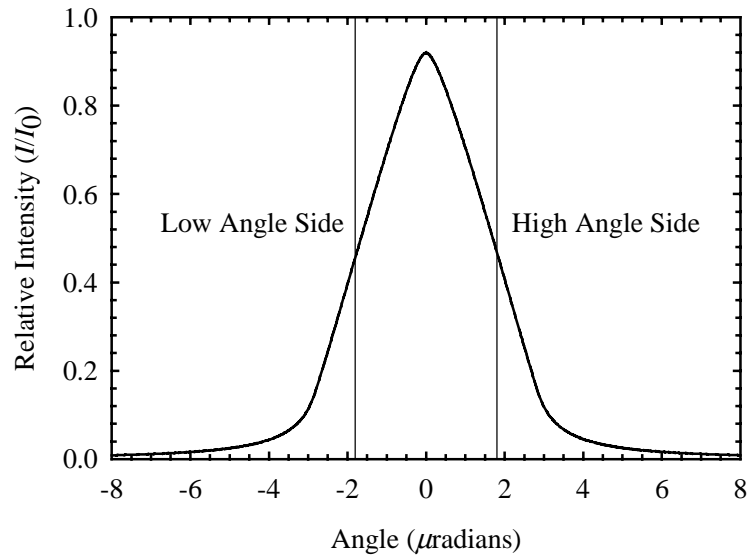


Figure 3.2. Normalized rocking curve for 18 keV x-rays on a 10-mm thick Si crystal at the [333] plane. An angle of 0 on the horizontal scale corresponds to the Bragg angle for this arrangement.

emerging from the sample is affected depending on the incident angle onto the crystal. Rays emerging from the object undeflected will impinge on the analyzer crystal at the tuning angle and be diffracted with the corresponding reflectivity. X-rays that are deflected upwards by the object will impinge at an angle less than the tuning angle while the x-rays that are deflected downwards by the object will impinge at an angle greater than the tuning angle. The reflected intensities of the deflected x-rays will then be higher or lower than the undeflected x-rays, depending on both the tuning angle for undeflected x-rays and the angle at which the deflected x-rays impinge on the analyzer crystal. Figure 3.1 is a schematic of x-rays traversing a homogeneous cylindrical object of radius r and refractive index n_2 . The height of the incident beam y is measured relative to the center of the cylinder. The x-rays incident on the top half of the cylinder are deflected up. Figure 3.2 shows the rocking curve of the [333] reflection of a silicon crystal with 18 keV incident x-rays. The horizontal axis shows the angular deviation from the Bragg angle. It is roughly triangular in shape, as expected from consideration of the dynamical diffraction of x-rays by the monochromator

and analyzer, which are assumed to be perfect crystals (Zachariassen 1945, Warren 1969, Zhong et al 2000). If the analyzer crystal is tuned to the low angle side or the high angle side, undeflected x-rays incident on the crystal will be diffracted with an intensity of half the peak intensity. Since the resulting refraction contrast originates from the slope of either shoulder of the triangular-shaped rocking curve, it depends on the FWHM of the rocking curve as well as the tuning angle.

The intensity of x-rays reaching the detector that have traversed a sample and been diffracted by the analyzer can be expressed as (Chapman *et al*, 1997)

$$I = I_R R(\theta_0 + \Delta\theta_z), \quad (3-1)$$

where, I_R is the intensity through the sample after attenuation is considered, $R(\theta)$ is the reflectivity of the crystal, θ_0 is the tuning angle of the analyzer and $\Delta\theta_z$ is the deflection angle.

From figure 3.2 it can be seen that the slope at the low angle side or the high angle side the rocking curve is the steepest, the rocking curve can be approximated by:

$$R(\theta_0 + \Delta\theta_z) = R(\theta_0) + \left. \frac{dR}{d\theta} \right|_{\theta=\theta_0} \Delta\theta_z. \quad (3-2)$$

In DEI, two images are acquired, one from each side of the rocking curve because the absorption will be the same for each image, but the sensitivity to refraction will be of opposite sign due to the difference in the sign of the slopes on the two sides. Thus, denoting I_l and I_h as the recorded intensities from the low and high sides of the curve and using equation 3-2 the following pair of equations are produced:

$$I_L = I_R \left(R(\theta_L) + \left. \frac{dR}{d\theta} \right|_{\theta=\theta_L} \Delta\theta_z \right) \quad (3-3a)$$

$$I_H = I_R \left(R(\theta_H) + \left. \frac{dR}{d\theta} \right|_{\theta=\theta_H} \Delta\theta_z \right). \quad (3-3b)$$

Equations 3-3a and 3-3b can be solved simultaneously for I_R and $\Delta\theta_z$ to produce:

$$\Delta\theta_z = \frac{I_H R(\theta_L) - I_L R(\theta_H)}{I_L \left. \frac{dR}{d\theta} \right|_{\theta=\theta_H} - I_H \left. \frac{dR}{d\theta} \right|_{\theta=\theta_L}} \quad (3-4a)$$

$$I_R = \frac{I_L \left. \frac{dR}{d\theta} \right|_{\theta=\theta_H} - I_H \left. \frac{dR}{d\theta} \right|_{\theta=\theta_L}}{R(\theta_L) \left. \frac{dR}{d\theta} \right|_{\theta=\theta_H} - R(\theta_H) \left. \frac{dR}{d\theta} \right|_{\theta=\theta_L}}. \quad (3-4b)$$

Equation 3-4a, when applied on a pixel-by-pixel basis to the DEI images, will produce a map of the refraction angle, referred to as the refraction image. Equation 3-4b produces the apparent absorption image, because it contains both absorption and other extinction information about the sample (Chapman et al, 1997, Hasnah et al, 2002).

3.2.2 Contrast and Gain

The image as recorded by the detector contains information about the absorption and refraction characteristics of the sample. In conventional radiography, contrast is a measurement of the absorption of a sample compared to the average background. If I_{smp} denotes the radiation intensity measured at the detector due to absorption of the sample, and \bar{I} denotes the average intensity of the background, then the following well-known relation defines the radiographic contrast for a sample of uniform thickness:

$$C_{rad} = \frac{\bar{I} - I_{smp}}{\bar{I}}. \quad (3-5)$$

For a sample of varying thickness, such as a cylinder, the maximum contrast can be measured at the point of greatest absorption in the sample. Then equation 3-5 becomes

$$C_{rad} = \frac{\bar{I} - I_{min}}{\bar{I}}, \quad (3-6)$$

where I_{min} is the intensity at the detector after absorption of x-rays by the thickest part of the sample. While this definition can be used to compare conventional radiography with the apparent absorption image in DEI, it can not be used to define a refraction contrast.

The radiographic contrast can also be characterized by comparing the difference between the average background and the sample to the noise level of the background. This signal-to-noise ratio (SNR) is defined as,

$$SNR_{rad} = \frac{\bar{I} - I_{min}}{\sigma}, \quad (3-7)$$

where σ is the rms noise level. The noise level in the images was obtained by finding the standard deviation at the signal relative to the background intensity (the pixel values in a region of the image, which should be uniform).

Until now there has been no definition of contrast for DEI images. Two references (Colonna et al, 2001, Keyrilainen et al, 2002) include comments on the contrast of a DEI image by comparing the intensity at the middle of a cylinder to the intensity at the edge. While this is informative, it is impractical from the clinical point of view, since the relationship of the object to the background is often of more importance than its relationship to itself. Since various types of images can be formed using DEI, the definition of contrast varies with the type of image. For images acquired with the analyzer tuned to the peak of the rocking curve, the minimum in intensity could correspond to the region with the greatest refraction, rather than with the largest absorption. Indeed, the region with the largest absorption but no refraction will have comparable intensity as in a conventional radiograph. In the example of a cylinder, the region of greatest refraction is near the top and bottom of

the cylinder, while the region of greatest absorption is across the horizontal diameter. So, the contrast in a peak image is denoted by C_{peak} and is defined by

$$C_{peak} = \frac{\bar{I} - I_{min,peak}}{\bar{I}}, \quad (3-8)$$

where \bar{I} is defined as in equation 3-6, and $I_{min,peak}$ indicates the minimum intensity of the sample as a result of the analyzer crystal being tuned to the peak of the rocking curve.

For the refraction image described by equation 3-4a, the situation presents a unique challenge. There can be no analogous contrast for a refraction image because the average background is zero (i.e., no refraction in the background). However, an SNR can be defined based on the noise level in the background, analogous to equation 3-7:

$$SNR_{ref} = \frac{\theta_{R,max} - \theta_{R,min}}{\sigma_{ref}}, \quad (3-9)$$

where $\theta_{R,max}$ and $\theta_{R,min}$ are respectively, the maximum and minimum values in the refraction image, and σ_{ref} is one standard deviation of the refraction signal from the average background.

Quantitative comparisons between the images created using DEI and the normal radiographs are now possible using equations 3-6 – 3-9. The peak gain, G_{peak} , is defined as the ratio of the peak contrast (equation 3-8) to the radiographic contrast (equation 3-6) and is given by

$$G_{peak} = \frac{C_{peak}}{C_{rad}}. \quad (3-10)$$

The refraction gain, G_{ref} , is defined as the ratio of the refraction SNR (equation 3-9) to the radiographic SNR (equation 3-7) and is given by,

$$G_{ref} = \frac{SNR_{ref}}{SNR_{rad}}, \quad (3-11)$$

which is meaningful only if the doses to the sample are the same in each image, which is how these images were acquired. Details on controlling the doses are discussed below. Ratios greater than unity in equations 3-10 and 3-11 indicate a higher contrast from DEI than from conventional radiography.

3.3 Methods

The comparison between DEI and conventional radiography was investigated in two ways: by computer simulation and experimentally. In this section an algorithm is developed to trace the path of monochromatic x-rays through a cylindrical object, off the analyzer crystal and to the detector. This is followed by the description of the DEI apparatus and the method by which the images were acquired. The resulting images from both the simulations and experiment were then compared using the equations from the previous section.

3.3.1 Computer model simulations

For the computer model, it is assumed that the x-ray source is a bending magnet on a synchrotron. In fact, the computer model simulates the characteristics of the X-15A beamline at NSLS. The x-rays travel through a double crystal monochromator before they reach the object to be imaged. Referring to figure 3.1, the detailed trace of an x-ray through the cylindrical object assumes that source is far away from the object (much larger than the object diameter). The incident angle, θ_1 is measured relative to the surface normal of the cylinder of radius r , whose axis is horizontal and perpendicular to the direction of the x-ray beam. The refractive index gradient and Snell's law determine the change in direction at each interface:

$$n_1 \sin \theta_1 = n_2 \sin \theta_2, \quad (3-12)$$

where n_1 and n_2 are the refractive indices of air and the sample, respectively. It is also important to note that for x-rays, the real parts of the complex refractive indices are less than unity and can be expressed as,

$$n = 1 - \delta, \quad (3-13)$$

where for the high-energy x-rays used and low-Z material imaged, δ is approximately given by,

$$\delta \cong \frac{N\lambda^2 r_e}{2\pi}, \quad (3-14)$$

where N is the number of electrons per unit volume of the sample material, r_e is the classical electron radius and λ is the x-ray wavelength.

Using equations 3-12 and 3-13 it can be shown that for a linear interface between two regions of distinct refractive indices, n_1 and n_2 , respectively, that an incoming x-ray incident in region 1 will be deflected by an angle $\Delta\theta_z$ approximated by

$$\Delta\theta_z \cong \Delta\delta \tan \theta_1, \quad (3-15)$$

where $\Delta\delta = n_1 - n_2$ is the difference in refractive indices. When this relation is extended to the cylinder in figure 3.1, the deflection angle becomes,

$$\Delta\theta_z \cong 2\Delta\delta \tan \theta_1. \quad (3-16)$$

The incident angle can also be expressed as a function of the position of the incident beam height. If y denotes the vertical position relative to the horizontal diameter of the cylinder, then the relation between the incident angle and the height and is

$$\sin \theta_1 = \frac{y}{R}. \quad (3-17)$$

Additionally, the horizontal chord can approximate the path length of the ray inside the cylinder from the point at which the x-ray impinges on the cylinder to where it exits:

$$z_2 = 2\sqrt{R^2 - y^2}, \quad (3-18)$$

Along this path the intensity is reduced by linear attenuation:

$$I = I_0 \exp(-\mu z_2), \quad (3-19)$$

where μ is the linear attenuation coefficient of the cylinder material.

For simulating an image, a ray is traced from the monochromator, through the object, and to the detector. Each ray is traced for a different position relative to the center of the cylinder, resulting in a one-dimensional image at the detector. The object is a cylinder oriented horizontally. The impact point of the deflected ray emitted from the cylinder is obtained by determining the total path length of the ray and the vertical deflection of the ray from horizontal. The intensity measured at the detector is determined by the attenuation of the x-ray through the sample and, for the DEI images, the reflectivity of the analyzer crystal. The detector elements are assumed to be square pixels of side d , which for this study was set at $50 \mu\text{m}$. The resulting two-dimensional image then represents the raw radiographic image. Thus the intensity measured at the pixel with coordinates x and y is given by

$$I_{rad}(x, y) = I_0 \exp(-\mu z(y)). \quad (3-20)$$

The source and detector sizes must also be considered. For the computer simulations, the source was assumed to be finite, with a Gaussian profile, given by

$$I_{source}(x, y) = \exp\left[-\frac{x^2}{2\sigma_x^2} - \frac{y^2}{2\sigma_y^2}\right], \quad (3-21)$$

where, x and y are spatial coordinates, and σ_x and σ_y are the beam width and height, respectively, as it emerges from the storage ring into the beamline. The values for σ_x and σ_y are, respectively, 0.00371 cm and 0.00027 cm. The final image at the detector is described by the convolution of the source function and the object transfer function further convolved with the detector point spread function (PSF). Thus, if the symbol \otimes represents a convolution in one dimension and $\otimes \otimes$ represents a two-dimensional convolution, then the final image can be represented by

$$I = (I_{source} \otimes \otimes I_{rad}) \otimes \otimes \text{PSF}. \quad (3-22)$$

A Gaussian PSF was used for representing the detector using a similar expression to equation 3-20. The FWHM of the PSF were 145 μm in the horizontal direction and 138 μm in the vertical direction (Kiss et al, 2002).

For DEI images, the characteristics of the analyzer crystal are important. In modeling the DEI images, the intensity of the radiation emerging from the object has been modified by the analyzer crystal prior to impinging on the detector. The preceding discussion focused on the interaction of radiation with matter, summarized by the I_R term in equation 3-1. The reflected intensity of the analyzer crystal is now considered (the $R(\theta)$ term). For refraction, the intensity will be affected based on the incident angle as well as the rocking curve characteristics. The incident angle was computed by adding the deflection angle to the analyzer tuning angle. A tuning angle of 0 indicates that the crystal is tuned to the Bragg angle, and $\pm \Delta\theta_D/2$ indicates that the crystal is tuned to the low angle side or the high angle side. The reflectivity of the crystal corresponding to the incident angle is then multiplied by the intensity of the impinging x-ray according to equation 3-1 and this value is recorded at the detector. Thus, equation 3-21 is modified as follows to account for the analyzer crystal:

$$I = (I_{source} \otimes \otimes (I_{object} R(\theta_{incident}))) \otimes \otimes \text{PSF}. \quad (3-23)$$

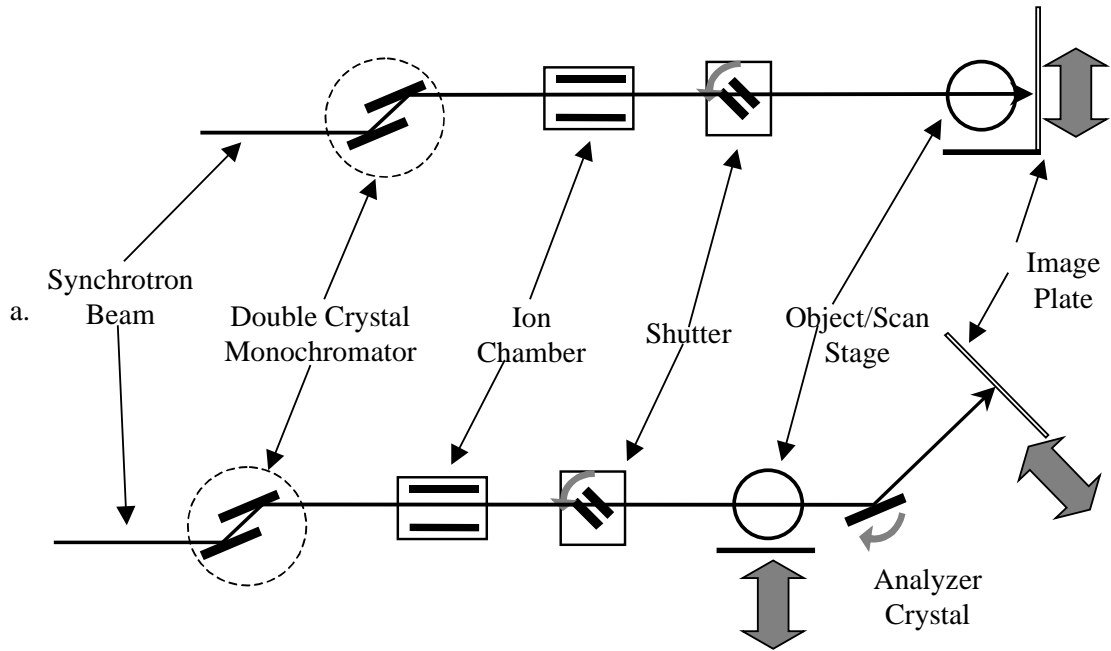
Equation 3-23 actually represents a set of three images, one for each of three points on the rocking curve. The two off-peak images were then combined according to equation 3-4.

The final adjustment to the images was accounting for noise. In order to model the noise of the entire imaging system, the background regions in the experimental images were measured and the noise was defined as one standard deviation from the mean. A random number generator was used in the modeling to represent this noise following a Poisson distribution, with σ_{max} chosen based on empirical results. A random number was added to each pixel in the final image (equations 3-21 and 23). The final set of three images, the radiograph, the refraction image, and the peak image were then analyzed for their respective contrast values according to equations 3-5 – 3-12.

3.3.2 Experiment

Experiments were carried out at the X-15A beamline, at the National Synchrotron Light Source, Brookhaven National Laboratory, Upton, New York. A schematic representation of the apparatus is shown in figure 3.3.

The apparatus consisted of a double crystal Bragg monochromator that prepared an imaging beam of 1-mm height and 8-cm width. Images were obtained at 18 keV (figures 3.3a and 3.3b). This particular energy was used because it represents the mean x-ray energy used in mammography. X-rays energies above 18 keV would reduce the contrast for the conventional radiograph drastically while not affecting the DEI contrast much, thus yielding even higher DEI gains than those reported for 18 keV. Lower x-ray energies would improve the contrast for conventional radiographs, yielding a lower DEI gain, but these energies are irrelevant for clinical applications. The incident photon flux on the sample was measured



b.
 Figure 3.3. Schematic representation of the DEI apparatus on the X-15A beamline at NSLS. a) Radiograph mode. b) DEI mode.

using an ion chamber filled with atmospheric pressure air and biased at -500 V. A fast shutter system was used to control the exposure to the detector. The shutter opened when the scanning stage was at a constant velocity and was closed at the end of the scan range before the stage was slowed to a stop. The dose was controlled by a combination of incident beam Lucite absorbers and the scanning speed. This method of dose control was previously verified and calibrated using TLD dosimetry.

For DEI images, an additional silicon [333] analyzer crystal was placed in the beam path between the sample and the detector (figure 3.3b). The detector was tilted by an angle corresponding to twice the Bragg angle of the analyzer so that it was perpendicular to the beam diffracted by the analyzer. The analyzer was tuned by rotating it about its horizontal axis. A second ionization chamber measured the exit dose and the image was recorded using a Fuji HR5 image plate. The plates were read out using a Fuji BAS2500 Image Plate Reader.

Conventional radiographs were obtained by placing the image plate on the sample stage, perpendicular to the beam, and scanning the sample and plate together through the beam. DEI images were obtained by scanning the sample and the image plate in opposite directions. Raw images were obtained with the analyzer crystal tuned to the Bragg angle (peak images), or at the low angle side or high angle side.

The dose was reduced by a factor of two for each of the DEI images on the sides of the rocking curve. Thus, the dose used for forming the refraction image is that same as the DEI peak image or the conventional radiograph.

The objects to be imaged were nylon fishing line, and Lucite cylinders. Table 1 lists the relevant characteristics of each object. The values for the refractive index and the linear attenuation coefficient were obtained from the Center for X-Ray Optics website (see references). The fishing line diameters are the nominal values stated by the manufacturer.

Table 3.1. Characteristics of samples used for imaging, listed by the real part of the refractive index ($n - 1$), linear attenuation coefficient, and density.

Object	Diameters (mm)	δ	μ (cm ⁻¹)	ρ (g/cm ³)
Nylon fishing line	0.101, 0.2032, 0.5588, 0.7112	8.01×10^{-7}	0.616	1.14
Lucite cylinders	6.35, 12.7, 25.4	8.23×10^{-7}	0.643	1.19

3.4 Results and Discussion

Images of two nylon wires (0.5588 mm and 0.2032 mm diameter) and one of the Lucite cylinders (0.635 cm diameter) are shown in figure 3.4 arranged in columns a, b, and c, respectively. Each row shows, from top to bottom, the conventional radiograph mode, the peak mode, and the refraction mode. The peak and radiographic images are photographic positives, which means that the objects show up darker than the backgrounds. The bright regions in the refraction image indicate refraction below the horizontal and the dark regions indicate refraction above the horizontal. Since the background does not refract the incident

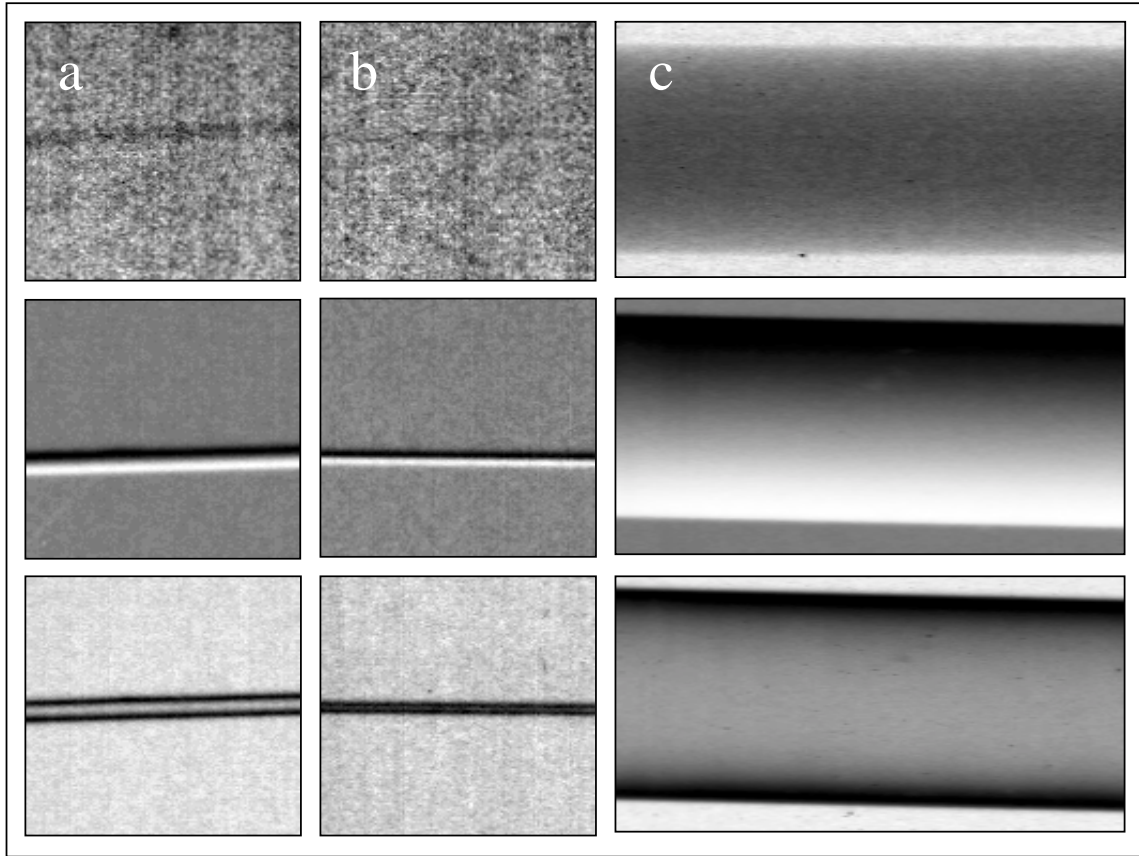


Figure 3.4. Experimental images of Nylon wires (column a – 0.5588 mm and column b – 0.2032 mm) and a Lucite cylinder (column c – 6.35 mm). The top row shows the radiograph. The second row shows the refraction images and the bottom row shows images taken at the peak of the rocking curve.

x-rays, it appears gray in this image. A comparison between the DEI images and radiograph clearly indicate that the DEI image has a less noisy background and enhances the edges of the object. The radiograph of the smaller nylon wire has such low contrast (1.6 % compared to 20.7% for the peak image) that it is barely discernible from the background. These images clearly demonstrate the potential for DEI to resolve pixel-sized objects much better than conventional radiography. Figure 3.5 is a vertical line intensity profile through each of the images. The profile of the peak and the normal radiograph are compared in figure 3.5a, while the refraction is plotted in 3.5b. Figure 3.6 shows the corresponding computer simulation images of these objects. There is good qualitative agreement between the experimental and simulated images.

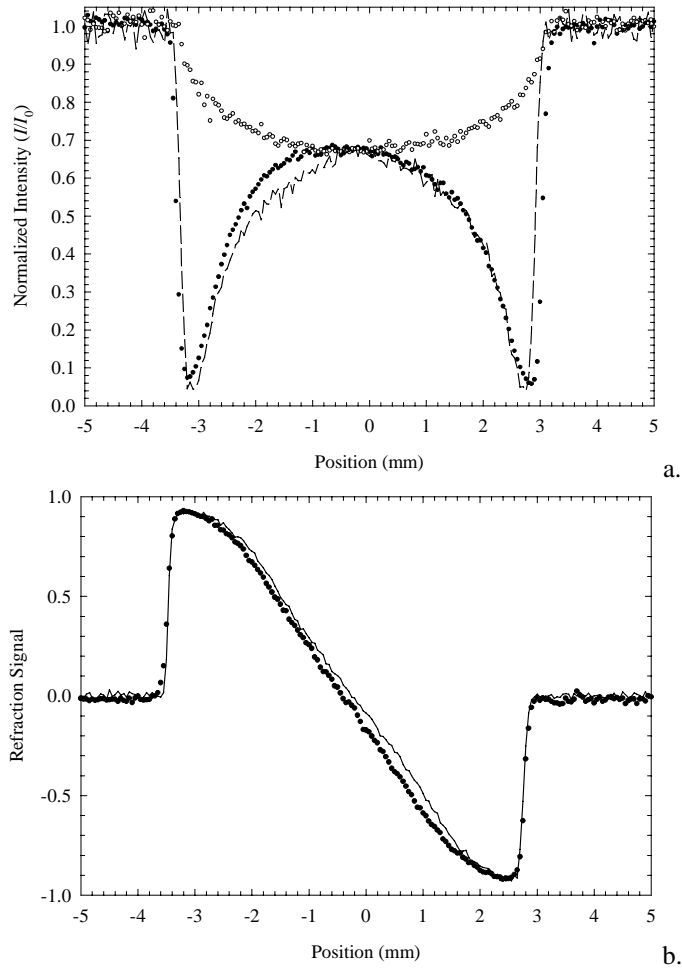


Figure 3.5. Vertical line profiles of the 6.35-mm diameter Lucite cylinder. a) Normalized intensity comparison of peak and radiograph. Experimental results are plotted as data points (solid circles for the peak image and hollow circles for the radiograph). The simulated peak image is superimposed and appears as a dashed line. b) Peak-to-peak refraction signal. The solid circles indicate the experimental points and the solid line represents the simulations.

It is important to note that the radiation dose used for the radiography and the DEI images are the same, viz., 200 mR surface dose. The linear gray scale for each image was adjusted manually to obtain the best contrast for the feature of interest. Since the conventional radiographs have much lower contrast than the DEI refraction or peak images, after this gray scale adjustment, the noise in these images appear much higher than the DEI images.

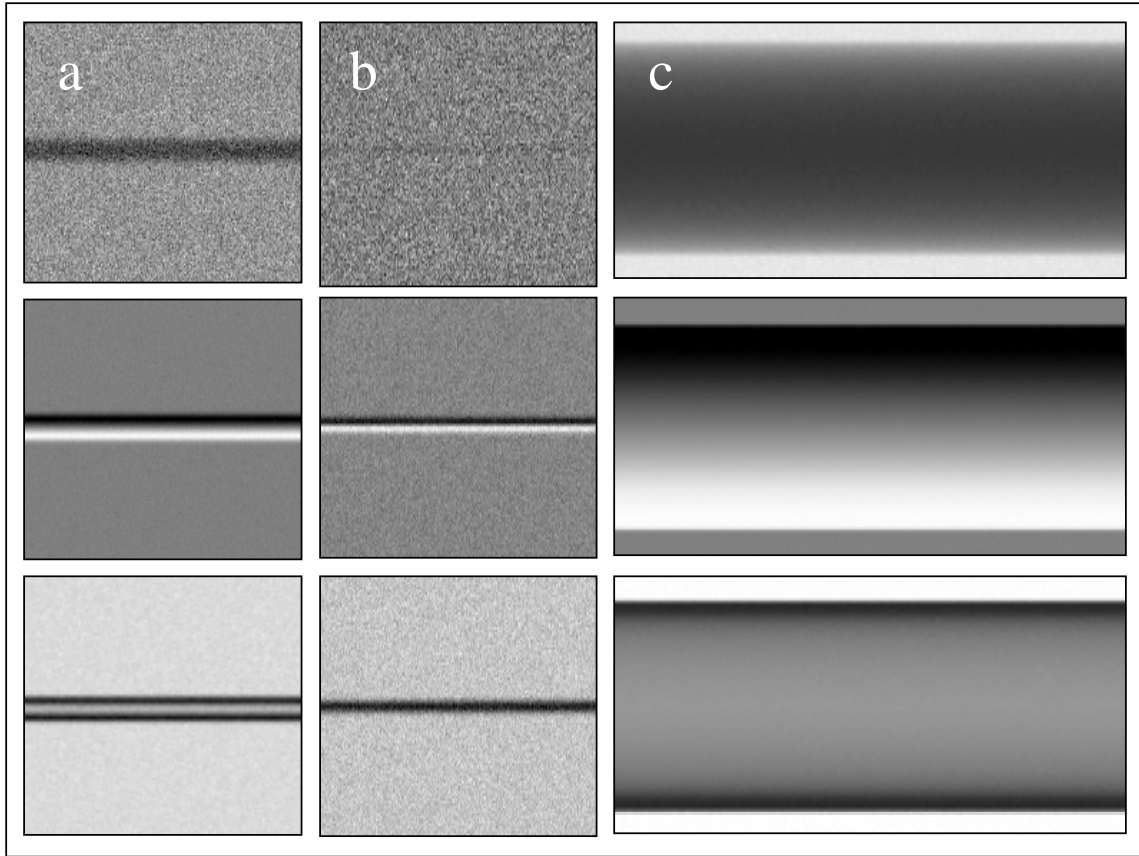


Figure 3.6. Simulated images of Nylon wires and a Lucite cylinder at the same diameters as shown in figure 3.4. Images are arranged identically to figure 3.4.

A more quantitative comparison of contrast is shown in figures 3.7 – 3.9. In figure 3.7, peak and radiographic contrast of Nylon and Lucite objects are plotted as a function of the object diameter-to-pixel size ratio (DPR) as defined in equations 3-6 and 3-8. Simulation results for the Lucite cylinders are graphed from a DPR of 10 to 600, and the results for Nylon are plotted for DPRs of 0.1 to 600. Experimental results are also shown. It is clear that for large diameters, the peak and radiographic contrast approach unity, following an exponential relation, $\sim 1 - \exp(-\mu x)$, where x is the diameter-to-pixel ratio and μ is a constant proportional to the linear attenuation coefficient. The minimum detectable size is approximately $100 \mu\text{m}$, or approximately twice the width of an individual pixel. The peak contrast falls off at a much slower rate and approaches the noise levels at a DPR of less than

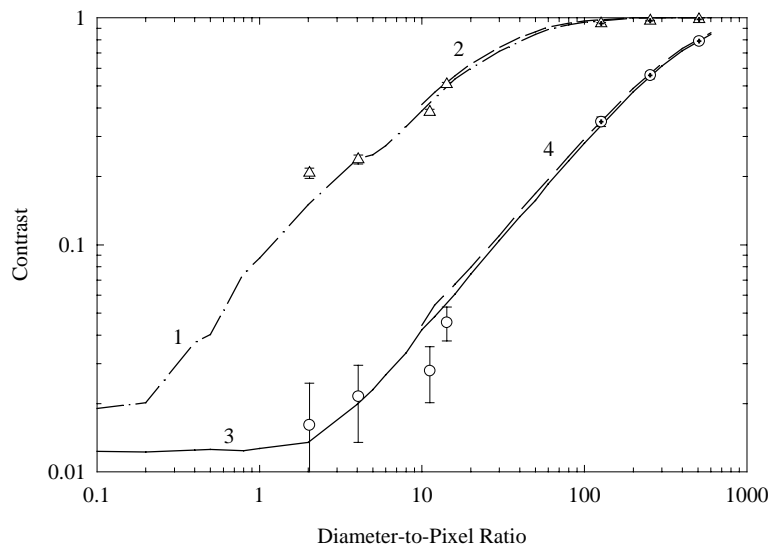


Figure 3.7. Graph of peak and radiographic contrast as a function of diameter-to-pixel ratio. The peak contrast is represented by curves 1 and 2, for Nylon and Lucite respectively. The radiographic contrast is represented by curves 3 and 4. Triangles, with and without crosshairs indicate experimental results for the peak, and circles indicate experimental results for the radiograph.

0.1. This is a direct consequence of the sensitivity to refraction contrast. Experimental results agree with the simulation results to within 20%.

Figure 3.8 is a plot of the SNR of the refraction and the radiographic images as a function of the DPR. There are a few noteworthy features in this graph. First, the SNR for the radiograph behaves in much the same fashion as the radiographic contrast in figure 3.7. The minimum SNR for the radiograph is approximately 0.9, indicating that the object is barely discernible from the background. The refraction SNR has a minimum value of approximately 5.8 at a DPR of 1 and it gradually increases to a constant level of 132. It is important to note that objects smaller than a DPR of 1 will not be visible in a refraction image due to the effect of the numerator in equation 3-4a. The contributions from both sides of the rocking curve in one pixel will cancel out. The constant SNR for large DPR corresponds to the maximum deflection angle allowed by the analyzer crystal. Experimental results for the Nylon and Lucite samples clearly follow the trend of the simulation results. It should also be noted that the overall higher SNR for the Lucite

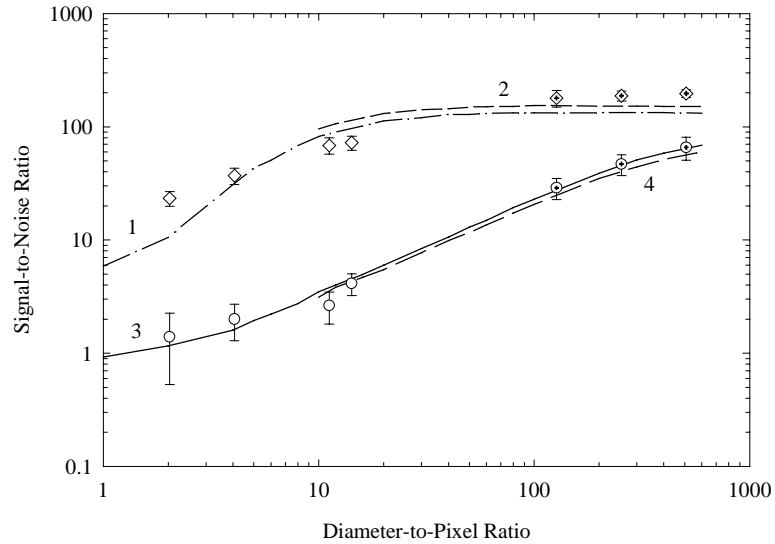


Figure 3.8. Signal-to-noise ratio plotted as a function of diameter-to-pixel ratio for refraction and radiograph. The refraction SNR is represented by curves 1 and 2, for Nylon and Lucite respectively. The radiographic SNR is represented by curves 3 and 4. Diamonds, with and without crosshairs, indicates experimental results for the refraction, and circles indicate experimental results for the radiograph.

cylinders compared to the Nylon wires is due to a larger dose used during the experiments. The simulations have accounted for this.

The gain values as defined by equations 3-9 and 3-10 are shown in figure 3.9. The peak gains for Nylon and Lucite are plotted in the same range as in figure 3.7, while the refraction gains are plotted in the same range as in figure 3.8. The results are consistently larger than unity for all objects that were imaged. The locations of the maxima in the two curves occur at a DPR of 4 for the peak gain and 10 for the refraction gain. They are directly related to the inflection point of the contrast curves in figures 3.7 and 3.8. Absorption tends to dominate at larger diameters since in this case the x-rays travel a longer path through the cylinder and are therefore undergo greater attenuation. Larger objects attenuate more radiation through absorption than smaller objects, which in turn results in high contrast, but little improvement is achieved using DEI. As the diameter is decreased, the path length through the cylinder also decreases, resulting in lower attenuation through absorption and refraction becomes the dominant contrast mechanism. For pixel-sized objects, the refraction

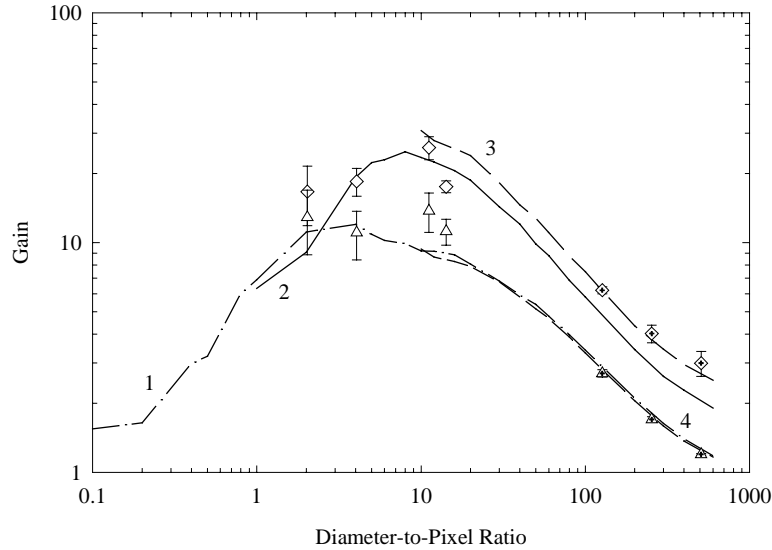


Figure 3.9. DEI gain as a function of diameter-to-pixel ratio. The peak gain is represented by curves 1 and 4, for Nylon and Lucite, respectively. The refraction gain is represented by curves 2 and 3. Diamonds, with and without crosshairs, indicate experimental results for the refraction, and triangles indicate experimental results for the peak.

and peak gains are approximately equal and the refraction achieves a minimum level of 6.3 at a DPR of 1 while the peak gain approaches unity. The peak gain for small objects indicates that the scatter rejection seems to be the dominant contrast mechanism.

Experimental results in figures 3.7 – 3.9 agree fairly well with the simulations. Discrepancies can be attributed to a few factors. First, values of the refractive index and linear attenuation coefficients of the samples may differ from the values used in the simulations. These values were obtained from semi-empirical calculations based on the density of the samples and their chemical compositions. Second, it was assumed that the samples were homogeneous and of uniform density based on manufacturer’s specifications. It is also possible that slight drift of the analyzer crystal from the prescribed position resulted in erroneous reconstruction of the refraction image. Finally, the Poisson noise characteristics used in the simulations are approximations and do not include other contributing factors to

noise such as electronic noise and noise due to scattered x-rays. But the important features in the graphs are present in both the experimental results as well as in the computer simulations.

3.5 Conclusions

A different definition of contrast has been presented for images acquired using DEI and a conventional radiographic configuration at a synchrotron. Using these definitions, images of homogeneous objects possessing simple geometry with uniform backgrounds were taken and then the contrasts were compared. It has been shown that DEI produces images with higher contrast, regardless of object size. The ratio between the DEI contrast and the conventional radiographic contrast, called the gain value has also shown that different mechanisms dominate the image formation depending on the object size: absorption dominates at the largest diameters due to the longer path length through the object. In the intermediate to small diameter regime, refraction dominates due to the rapidly changing curvature of the incident and exit faces of the object. At the smallest diameter, where the object diameter is approximately the size of a pixel or its PSF, extinction dominates as most of the refracted radiation has been averaged out over the size of the object.

Further investigation is required to understand the image forming mechanisms. Detector characteristics such as PSF, pixel size, and noise levels clearly define a lower limit of detection of small objects. The preceding study has indicated that this lower limit is improved when using DEI compared to conventional radiography.

Acknowledgments

The authors wish to thank Martin Yaffe, Etta Pisano, Gene Johnston, Christopher Parham, Kuruvilla Verghese, Chris Roland, and Hans Hallen for their suggestions and fruitful discussions. The authors also wish to thank the Customer Service Department at

Berkley Fishing for their assistance. This work was supported in part by US Army grant DAMD 17-99-1-9329 (MZK) and US Department of Energy grant DE-AC02-76CH00016 (ZZ). This research has been carried out (in part) at the National Synchrotron Light Source, Brookhaven National Laboratory, which is supported by the U.S. Department of Energy, Division of Materials Sciences and Division of Chemical Sciences.

References

Baruchel J., Lodini A., Romanzetti S., Rustichelli F., Scrivani A., “Phase-contrast imaging of thin biomaterials,” *Biomaterials* **22** (2001) 1515 - 1520.

Carroll F.E., Waters J.W., Andrews W.W., Price R.R., Pickens D.R., Willcott R., Tompkins P., Roos C., Page D., Reed G., Ueda A., Bain R., Wang P., Bassinger M., “Attenuation of monochromatic x-rays by normal and abnormal breast tissues,” *Investigative Radiology* **29** (1994) 266 - 272.

Center for X-Ray Optics: <http://www-cxro.lbl.gov/>.

Chapman D., Thomlinson W., Johnston R.E., Washburn D., Pisano E., Gmür N., Zhong Z., Menk R., Arfelli F., and Sayers D., “Diffraction Enhanced x-ray Imaging,” *Phys. Med. Biol.* **42** (1997) 2015-2025.

Colonna S., D’Acapito F., Mobilio S., Onori S., Pugliani L., Romanzetti S., Rustichelli F., “Curved Optics for x-ray phase contrast imaging by synchrotron radiation,” *Phys. Med. Biol.* **46** (2001) 967-974.

Fandos-Morera A., Prats-Esteve M., Tura-Soteras J.M., Traveria-Cros A., “Breast tumors: composition of microcalcifications,” *Radiology* **169** (1988) 325 – 327.

Galkin M.G., Feig S.A., Patchefsky A.S., Rue J.W., Gamblin W.J., Gomez D.G., Marchant L.M., “Ultrastructure and microanalysis of ‘benign’ and ‘malignant’ breast calcifications,” *Radiology* **124** (1977) 245 – 249.

Galkin M.G., Frasca P, Feig S.A., Holderness K.E., “Non-calcified breast particles: a possible new marker for breast cancer,” *Investigative Radiology* **17** (1982) 119 – 128.

Hasegawa, B.H., *The Physics of Medical X-Ray Imaging*, 2d Ed., (1991), Medical Physics Publishing, Madison.

Hasnah M.O., Zhong Z., Oltulu O., Pisano E., Johnston R.J., Sayers, D.E., Thomlinson W., Chapman D., “Diffraction enhanced imaging contrast mechanism in breast cancer specimens,” *Medical Physics*, **29** (2002) 2216 – 2221.

Ingal V.N., Beliaevskaya E.A., Brianskaya A.P., Merkurieva R.D., “Phase mammography – a new technique for breast investigation,” *Phys. Med. Biol.* **43** (1998) 2555 – 2567.

Ishisaka A., Hiromu O., Honda C., “A new method of analyzing edge effect in phase contrast imaging with incoherent x-rays,” *Optical Review* **7** (2000) 566-572.

Keyrilainen J., Fernandez M., Suortti P., “Refraction contrast in x-ray imaging. *Nucl. Instr. and Meth. A*, **480** (2002) 419-427.

Kiss M.Z., Sayers D.E., Zhong Z., “Comparison of digital detectors for integration into a diffraction-enhanced imaging system,” *Nucl. Instr. and Meth. A*, **491** (2002) 280-290.

Kotre C.J., Birch I.P., “Phase contrast enhancement of x-ray mammography: a design study,” *Phys. Med. Biol.* **46** (1999) 2853 – 2866.

National Synchrotron Light Source: <http://nslsweb.nsls.bnl.gov/nsls/Default.htm>.

Olson S.L., Fam B.W. Winter P.F., Scholz F.J., Lee A.K., Gordon S.E., “Breast calcifications: analysis of imaging properties,” *Radiology* **169** (1988) 329 – 332.

Radi M.J., “Calcium Oxalate Crystals in Breast Biopsies,” *Arch. Pathol. Lab Med.* **113** (1989) 1367-1369.

Pisano E.D., Johnston R.E., Chapman D., Geradts J., Iacocca M., Livasy C.A., Washburn D.B., Sayers D.E., Zhong Z., Kiss M.Z., Thomlinson W.C., “Human Breast Cancer Specimens: Diffraction Enhanced Imaging with Histologic Correlation – Improved Conspicuity of Lesion Detail Compared with Digital Radiography,” *Radiology* **214** (2000) 895-901.

Surratt J.T., Monsees B.S., Mazoujian G., “Calcium oxalate microcalcifications in the breast,” *Radiology* **181** (1991) 141 – 142.

Warren, B.E., *X-Ray Diffraction* (1969), Dover, New York.

Winston J.S., Yeh I.-T., Evers K, Friedman A.K., “Calcium oxalate is associated with benign breast tissue: can we avoid biopsy?” *Anatomic Pathology* **100** (1993) 488 – 492.

Zachariasen, W.H., *Theory of X-Ray Diffraction in Crystals* (1945), Dover, New York.

Zhong Z., Thomlinson W., Chapman D., Sayers D., “Implementation of Diffraction Enhanced Imaging Experiments at the NSLS and APS,” *Nucl. Instr. and Meth. A*, **450** (2000) 556-567.

Chapter 4. Improved Image Contrast Of Calcifications In Breast Tissue Specimens Using Diffraction Enhanced Imaging

A modified version of this chapter has been submitted as a paper for publication in *Physics in Medicine and Biology*.

Abstract

The contrast of calcifications in images of breast tissue specimens using a synchrotron-based diffraction enhanced imaging (DEI) apparatus has been measured and is compared to the contrast in images acquired using a conventional synchrotron-based radiographic imaging modality. DEI is an imaging modality which derives image contrast from x-ray absorption, refraction, and small-angle scatter-rejection, unlike conventional radiographic techniques, which can only derive contrast from absorption. DEI is accomplished by inserting an analyzer crystal in the beam path between the sample and the detector. Two specimens were analyzed: one with benign calcifications and one with calcifications associated with cancer. Results of the image analysis indicate that the DEI contrast of images taken with the analyzer crystal tuned to the peak of its rocking curve, was as much as 27 times that of the conventional radiograph, with an average of 5.5 for all calcifications. This improved image contrast for even near-pixel-size calcifications makes DEI a viable imaging modality in screening mammography.

4.1 Introduction

The presence of clusters of microcalcifications in the breast as revealed by a mammogram is often used as an indicator that the patient may be at risk for developing breast cancer. Several studies have been conducted which focused on the connection of calcifications to breast disease as well as their imaging properties specific to mammogram and their chemical composition (Carroll et al, 1994; Cowen et al, 1997; Fandos-Morera et al

1988; Galkin et al, 1977; Galkin et al 1982; Olson et al, 1988; Radi, 1989; Surratt et al, 1991; and Winston et al, 1993). Calcifications can vary in size, morphology, chemical composition and density (Winston et al, 1993). In Winston's study, calcifications composed of calcium oxalate and calcium phosphate ranged in size from < 0.1 mm to 2 mm, though no correlation was seen with the type of calcification and diagnosis (benign or malignant). In contrast, Surratt et al reported in 1991 that calcium oxalate typically occurred in benign processes in the breast, while calcium phosphate had occurred in both benign and malignant processes. Despite the differences in their respective observations, they reach a common conclusion that the detection of calcifications is a key component in proper diagnosis.

A troublesome feature of calcifications is their detectability in mammogram. A calcification of higher density than the surrounding tissue will be seen more easily than one of lower density or of smaller size. Therefore, quantifying the radiographic contrast of a calcification can be a challenging task even with digital mammography. Sophisticated image processing techniques are often employed (computer aided diagnosis) to improve detectability, since the contrast is often too low for an observer to detect the calcification from the surrounding tissue (for example, Bazzani et al, 2001; Brake and Karssenmeijer, 1999; Chen and Lee, 1997; Cheng and Lui, 1998; Gavrielides and Lo, 2000; Giger, 1999; Li et al, 1996; Netsch and Peitgren, 1999; and Wang and Karayiannis, 1998). Cowen et al (1997) addresses this issue of difficulty of detectability of a calcification from a screen-film-based mammogram. They found that the minimum detectable size of a microcalcification was approximately 130 μm in both screen-film mammography and computed mammography for that particular study.

Diffraction Enhanced Imaging (DEI) is an imaging modality which derives image contrast from absorption, refractive effects, and small-angle scatter-rejection (Chapman et al 1997; Hasnah et al, 2002; Keyrilainen et al 2002; Kiss et al 2002; and Zhong et al 2000). In a study of seven breast cancer specimens using DEI, digital radiography and histologic correlation, Pisano et al, 2000 found that DEI improved conspicuity of lesion detail compared with digital radiography. This study, however, did not address the issue of calcification detection.

In an attempt to quantify the minimum detectable size of calcifications in breast tissue, experiments have been conducted using DEI. The images acquired using DEI were compared to images of the same specimens acquired using conventional radiographic techniques with respect to the contrast of the calcifications in the images. Specimens included two mastectomy breasts, from which the contrasts of 88 calcifications were computed and tabulated. DEI images exhibited a distinct improvement in the contrast of calcifications when compared to the normal radiograph. The resulting improved contrast can potentially improve the clinical diagnosis of breast disease and lead to DEI being accepted as the standard modality in screening mammography.

4.2 Theory

The theory for DEI appears elsewhere in the literature (Chapman et al 1997; Zhong et al 1999) and is summarized here. In order to visualize contrast mechanisms other than absorption in an object, a typical DEI image is acquired with the inclusion of a diffraction crystal between the object and the detector. X-rays impinging on an object will undergo refraction according to Snell's Law, with the refractive index (n) typically less than or equal to unity. The relationship comes from (Zachariassen, 1945):

$$n = 1 - \alpha + i\beta. \quad (4-1)$$

The real term α is approximately,

$$\alpha \cong \frac{N\lambda^2 r_e}{2\pi} \quad (4-2)$$

where N is the number of electrons per unit volume of the sample material, r_e is the classical electron radius (2.82×10^{-15}), and λ is the x-ray wavelength. For most materials and in the x-ray energy range of interest for diagnostic radiology, α is on the order of 10^{-6} .

The x-ray exits the object at some angle $\Delta\theta_z$ (referred to as the deflection angle) with respect to its original direction. While traversing the object, the x-ray is also attenuated by an amount proportional to $\exp(-\mu t)$, where μ is the linear attenuation coefficient of the material and t is the path length through the material. After traversing the object, the x-ray impinges on the analyzer crystal and undergoes diffraction. The intensity of the diffracted x-ray depends on the incident angle and the characteristics of the crystal's diffraction profile (rocking curve). For 18 keV x-rays and a Si [333] analyzer crystal, the rocking curve has a full width half maximum (FWHM) of approximately $3.6 \mu\text{rad}$. If the crystal is tuned to the peak of the rocking curve, the intensity x-rays that arrive with a deflection angle will be reduced, and those at incident angles larger than the FWHM value will be practically diminished. The analyzer crystal thus effectively extinguishes scattered x-rays, with incident angles on the order of milliradians.

A typical DEI experiment also includes images acquired with the analyzer crystal tuned to full width half maximum (FWHM) value on either side of the rocking curve peak of the analyzer crystal. These two images can then be combined to obtain the so-called

apparent absorption image and the refraction image. The algorithm for image reconstruction is given by (Chapman et al, 1997, Zhong et al, 2000):

$$\Delta\theta_z = \frac{I_H R(\theta_L) - I_L R(\theta_H)}{I_L \left. \frac{dR}{d\theta} \right|_{\theta=\theta_H} - I_H \left. \frac{dR}{d\theta} \right|_{\theta=\theta_L}}, \quad (4-3)$$

where I_H and I_L are the recorded intensities at the detector of the image taken at the FWHM positions of the rocking curve (L for low angle side, and H for high angle side), $R(\theta_L)$ and $R(\theta_H)$ are the reflectivities of the analyzer crystal at these positions, and $dR/d\theta$ is the derivative of the rocking curve evaluated at the low angle side and high angle side of the rocking curve. Equation 4-3 is applied on a pixel-by-pixel basis.

4.3 Experiment

Experiments were performed at the X-15A beamline of the National Synchrotron Light Source, Brookhaven National Laboratory, Upton, New York. Figure 4.1 is a diagram of the setup in both the radiography and DEI modes. A double crystal Bragg monochromator provided x-rays at 18 keV in a beam of 1 mm high and 125 mm wide. An ionization chamber (not shown in the figure) monitored this imaging beam to determine the skin entry dose at the sample. Typical dosages used were around 100 – 200 mR. A fast shutter system was used to control the exposure to the detector. The shutter opened when the scanning stage was at a constant velocity and was closed at the end of the scan range before the stage was slowed to a stop. The dose was controlled by a combination of incident beam Lucite absorbers and the scanning speed. For DEI images, an additional silicon [333] analyzer crystal was placed in the beam path between the sample and the detector. The detector was tilted by an angle corresponding to twice the Bragg angle of the analyzer so that it was perpendicular to the beam diffracted by the analyzer. The analyzer was tuned by rotating it

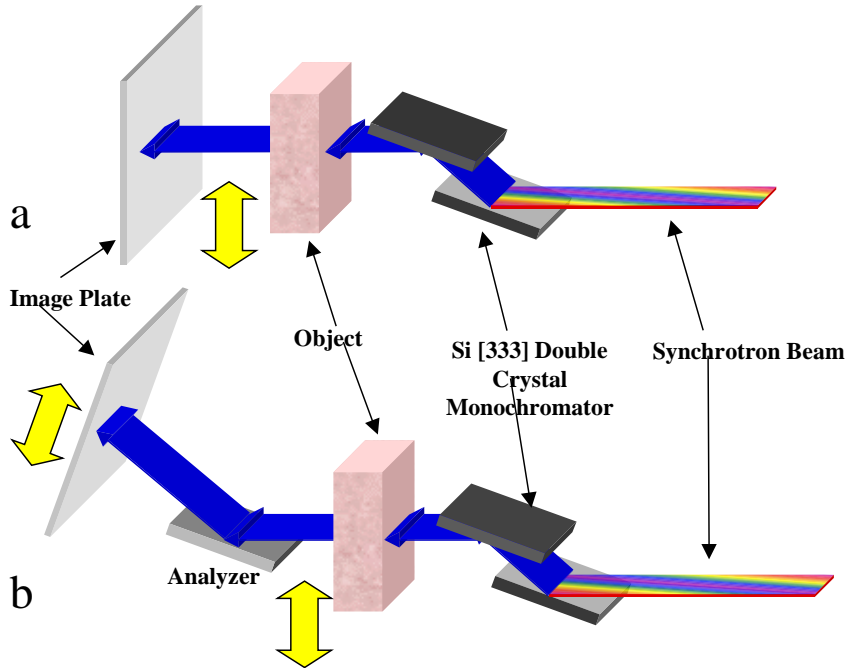


Figure 4.1. Schematic diagram of DEI imaging apparatus at beamline X-15A, National Synchrotron Light Source. a) Radiograph mode. b) DEI mode.

about its horizontal axis. A second ionization chamber measured the exit dose and the image was recorded using a Fuji HR5 image plate. Image plates were read out using a Fuji BAS2500 Image Plate Reader.

Synchrotron-based radiographs were obtained by placing the image plate on the sample stage, perpendicular to the beam, and scanning the sample and plate together through the beam. DEI images were obtained by scanning the sample and the image plate in opposite directions. Raw images were obtained with the analyzer crystal tuned to the Bragg angle (peak images), or on either side of the Bragg peak at angles corresponding to half the FWHM value of the rocking curve.

Two specimens were imaged. The samples were approximately 1 cm thick and were granted exemption by the institutional review boards of the participating institutions. Sample 1 was a pathological sample with no diagnosis of breast disease and the calcifications were not associated with malignant processes. Sample 2 was obtained from a mastectomy

containing ductal carcinoma in situ (DCIS) as well as invasive ductal carcinoma. Both samples were fixed in 10% buffered formalin and imaged in distilled water. Table 4.1 contains a summary of specimen details. The presence of calcifications was verified by a radiologist.

Table 4.1. Summary of samples imaged

Sample	Disease association	Number of calcifications
1	Benign	36
2	Ductal carcinoma in situ, invasive carcinoma	52

4.4 Results

Figures 4.2 and 4.3 show respectively, sample 1 and sample 2. In each figure, image a is the DEI peak, image b is the radiograph, and image c is the refraction image. Determining the contrast for the calcifications was accomplished using the following method: the candidate features were identified in both the radiograph and the corresponding DEI image (peak image). Several vertical line profiles were taken of each feature, from which the minimum pixel value of the feature was recorded. This was then compared to the average background of pixels surrounding the feature. The contrast for both the radiograph and peak images are calculated using:

$$C_{rad, peak} = \frac{I_{background,(rad/peak)} - I_{min,(rad/peak)}}{I_{background,(rad/peak)}}, \quad (4-4)$$

where the subscripts indicate the background or minimum intensity value in the radiograph or peak images. The contrast value for each line profile was calculated and averaged for each calcification. Figure 4.4 shows an example of the line profiles of one of the calcifications in sample 2 from the peak image (figure 4.4a), the radiograph (figure 4.4b), as well as the refraction image (figure 4.4c). The size of each feature was determined by

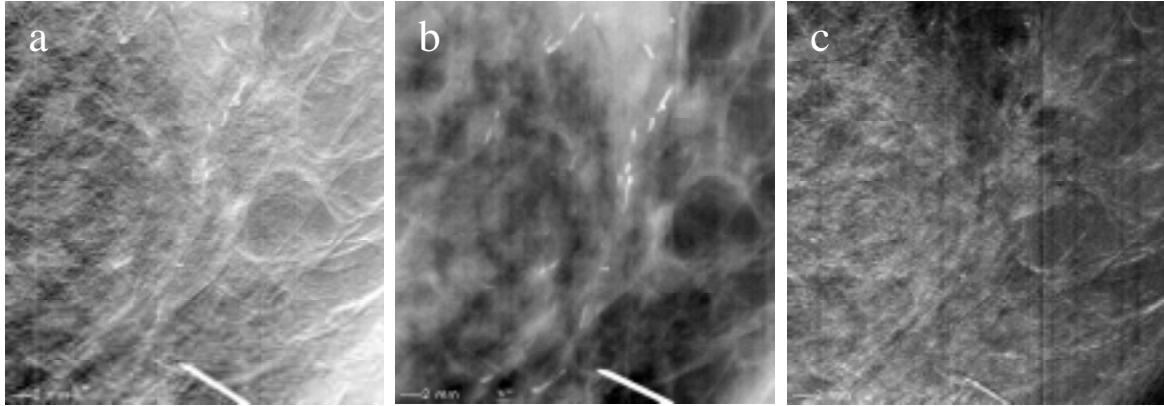


Figure 4.2. Images of sample 1. a) DEI peak. b) Radiograph. c) Refraction. Calcifications are visible throughout the images, as is a biopsy needle at the bottom.

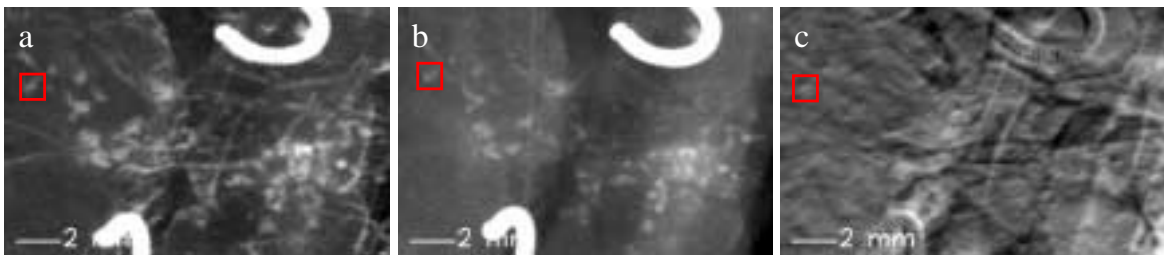


Figure 4.3. Images of sample 2. a) DEI peak. b) Radiograph. c) Refraction. The bright white regions visible at the top and bottom of each image are markers embedded in the tissue to indicate the region of interest. A red box in each image indicates the region of interested shown in figure 4.4.

measuring the average width of the intensity profile perpendicular to the longitudinal axis in several locations (three to seven) along the calcification.

The radiographic contrast can also be characterized by comparing the difference between the average background and the sample to the noise level of the background. This signal-to-noise ratio (SNR) is defined as,

$$SNR_{rad} = \frac{\bar{I} - I_{min}}{\sigma}, \quad (4-5)$$

where σ is the rms noise level. The noise level in the images was obtained by finding the standard deviation at the signal relative to the background intensity. Similarly, a SNR is defined for the refraction image as well. For the refraction image described by equation 4-3,

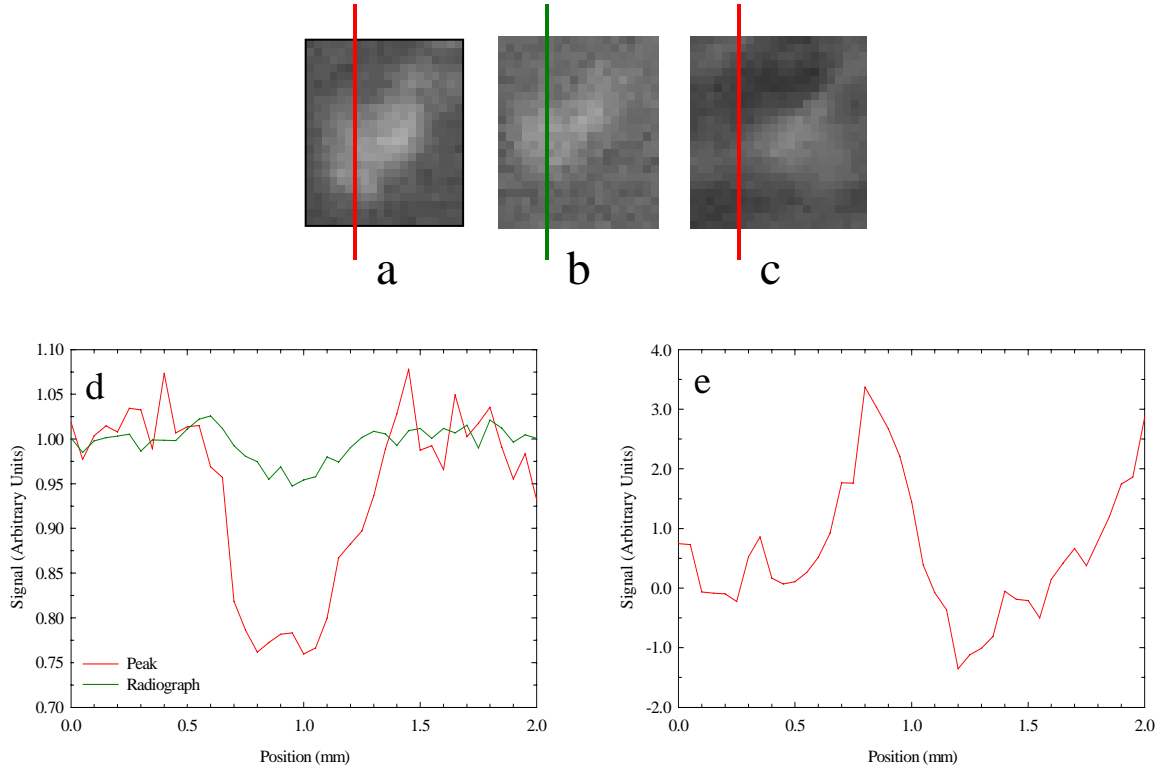


Figure 4.4. Region of interest in sample 2 with corresponding line profiles. a) DEI peak image. b) Radiograph. c) Refraction image. Vertical lines indicate location of line profiles displayed in d) peak and radiograph, and e) refraction. Line profiles are normalized to the respective backgrounds in the images.

there can be no analogous contrast because the average background is approximately zero (Kiss et al, in press). Thus the definition is given by:

$$SNR_{ref} = \frac{\theta_{R,max} - \theta_{R,min}}{\sigma_{ref}}, \quad (4-6)$$

where $\theta_{R,max}$ and $\theta_{R,min}$ are respectively, the maximum and minimum values in the refraction image, and σ_{ref} is one standard deviation of the refraction signal from the average background.

These measurements assume that the calcifications were approximately cylindrical or spherical in shape. Closer observation of peak images revealed that several of the calcifications were actually aggregates of two or more smaller calcifications.

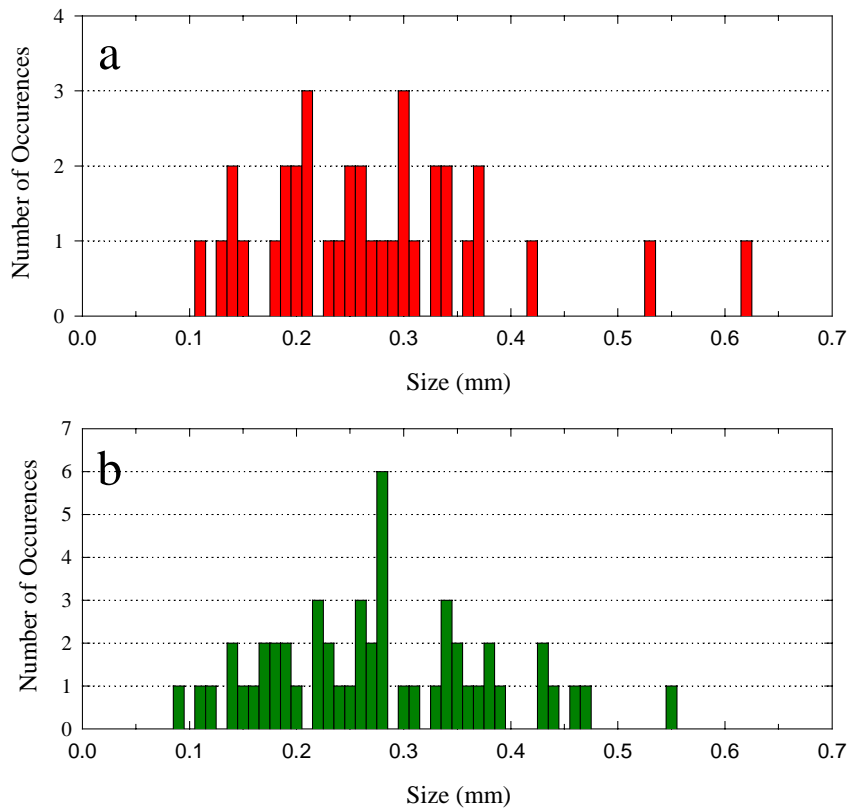


Figure 4.5. Histogram of calcification size distribution. a) Sample 1, b) sample 2.

Histograms of the calcification size distribution are plotted in figure 4.5. Table 4.2 result of a statistical analysis on these distributions. No obvious connections between calcification size and cancer were revealed for these particular samples, but this does not rule out such a relationship. Sample 1 had a larger range of sizes (0.51 mm, compared to 0.46 mm for sample 2), while sample 2 had a higher average particle size (0.28 mm). Sample 1 also had a relatively flat distribution, as indicated by the negative kurtosis value.

Table 4.2. Statistical results for calcification size histogram (figure 4.5)

Sample	No. of calcifications	Range of sizes (mm)	Average size (mm)	Skewness	Kurtosis
1	36	0.11 – 0.62	0.27 ± 0.1	1.2	2.414
2	52	0.09 – 0.55	0.28 ± 0.1	0.41	-0.201

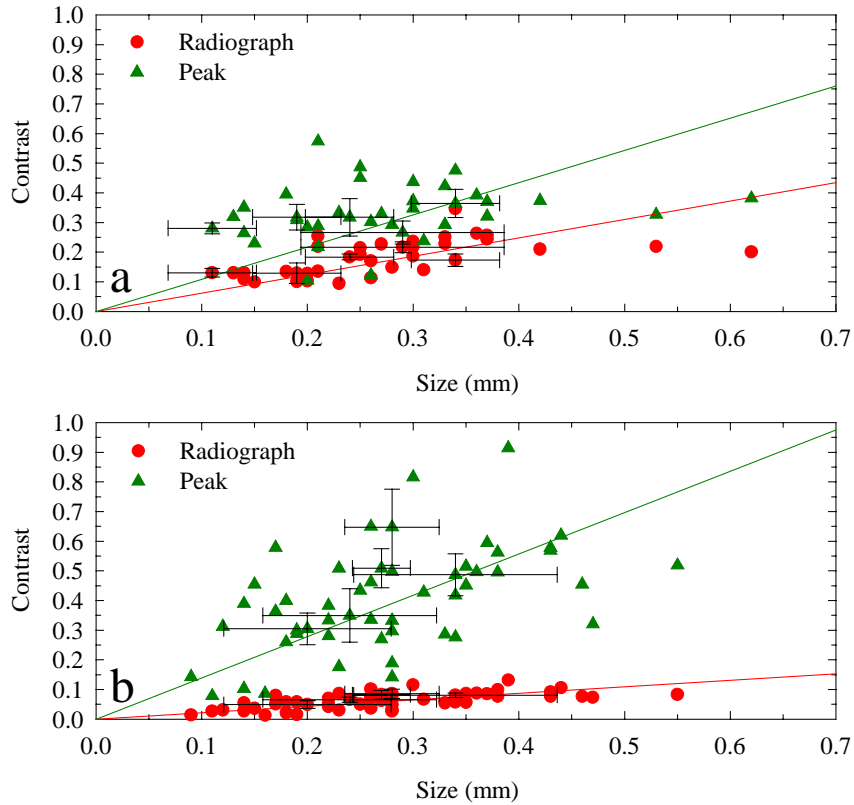


Figure 4.6. Plot of image contrast as a function of calcification size. a) Sample 1. b) sample 2. Linear least squares fitting results are superimposed on the respective scatter plots. Slopes of the lines are given in table 4.3.

Results of the contrast measurements are plotted in figures 4.6 for the two samples for in both radiograph and DEI peak mode. Horizontal and vertical error bars represent one standard deviation from mean values. Regression lines are fitted through the origin, with the slopes given in table 4.3. Two features are readily apparent in the figure. First, contrast in the peak images is consistently higher than that in the radiographs, indicating that DEI improve the contrast, even for pixel-sized and near-pixel-sized calcifications. Second, contrast in the radiograph images, dominated by absorption, tend to lie closer to their regression lines than the DEI images. This is due in part to the fact that DEI is more sensitive to the uniformity of the calcifications. Another contributing factor is the scatter rejection capability of DEI, which results in the exploitation of additional contrast

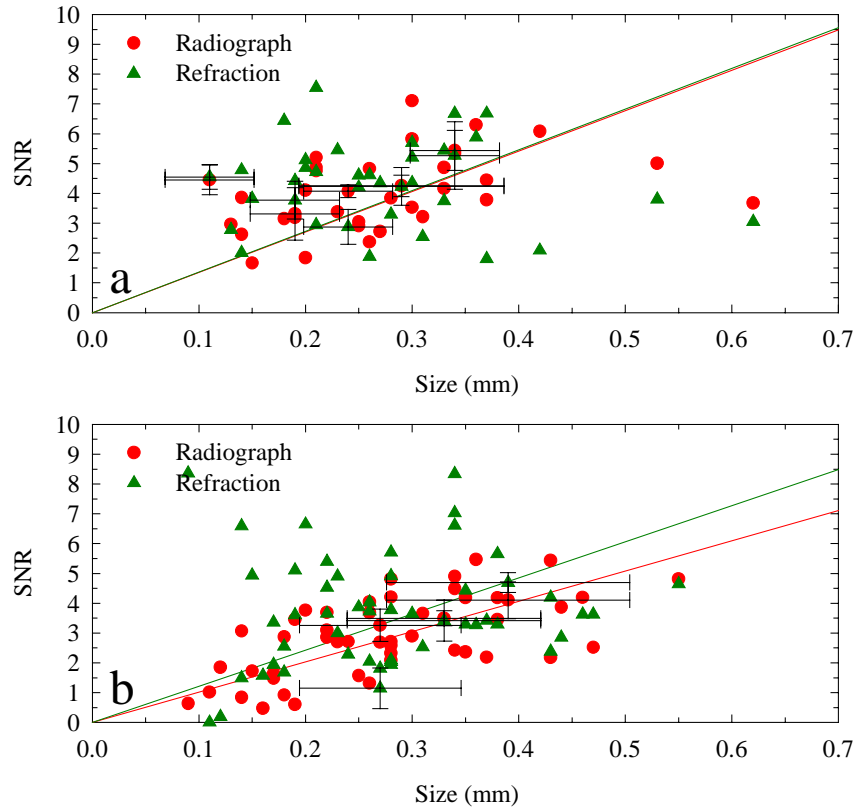


Figure 4.7. Plot of SNR as a function of calcification size. a) Sample 1. b) Sample 2. Linear least squares fitting results are superimposed on the respective scatter plots. Slopes of the lines are given in table 4.3.

mechanisms not possible with conventional radiographic techniques. Calcifications tend to be an agglomeration of material of varying homogeneity, which results in varying degree of scatter-rejection in DEI.

Figure 4.7 is a comparison of the signal-to-noise ratio (SNR) in the refraction and radiograph images as a function of the size of the calcification. The graphs are arranged by sample in the same manner as in figures 4.6 and 4.7. Regression lines are fitted here as well, through the origin and are also given in table 4.3. A comparison of the slopes of the refraction SNR to the radiograph SNR shows that they are approximately equal, suggesting that the improvement in contrast between the refraction and the radiograph is minimal.

Table 4.3. Slope values for regression lines in figures 4.6 – 4.7, and average gain values for figure 4.8.

Image Type	Sample 1	Sample 2
Peak Contrast	1.087	1.394
Radiograph Contrast	0.620	0.218
Ratio of slope	1.8	6.4
Average peak gain	1.9 ± 0.1	6.9 ± 0.4
Refraction SNR	13.6	12.1
Radiograph SNR	13.5	10.1
Ratio of slopes	1.01	1.2
Average refraction gain	1.2 ± 0.1	1.6 ± 0.2

The direct comparison of the DEI to the radiograph, in terms of their ability to visualize calcifications, is accomplished through the ratio of the peak contrast to the radiographic contrast, and the refraction SNR to the radiographic SNR. These two quantities are called the peak gain and refraction gain, respectively, and were introduced in a previous paper (Kiss et al, in press). The peak gain is given by:

$$G_{peak} \equiv \frac{C_{peak}}{C_{rad}}, \quad (4-7)$$

and the refraction gain is given by:

$$G_{ref} \equiv \frac{SNR_{ref}}{SNR_{rad}}. \quad (4-8)$$

Equation 4-8 is only valid if the combined dose used to obtain the two DEI images on the sides of the rocking curve is equal to the dose used to obtain the radiograph. Gains larger than unity would indicate that the DEI technique resolves contrast mechanisms not possible through conventional techniques. Figure 4.8 contains plots of the peak and refraction gain values for both samples as a function of calcification size. It is clear that the DEI peak gain is consistently greater than unity, independent of size, and with average gain values of 1.9 for

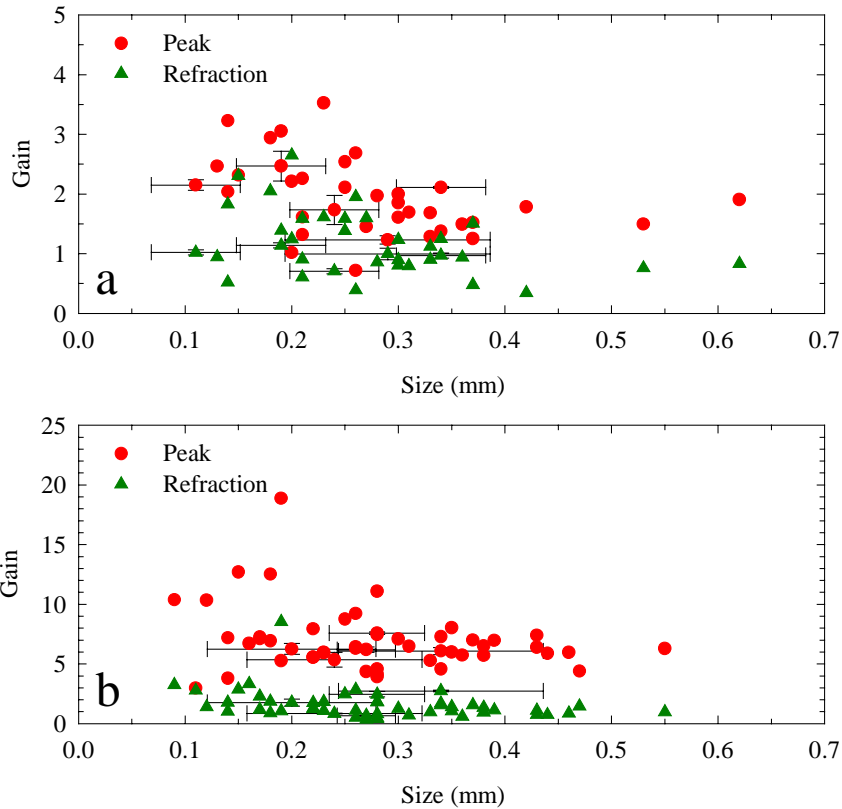


Figure 4.8. Plot of gain value as a function of calcification size. a) Sample 1. b) Sample 2.

sample 1 and 6.9 for sample 2. This is comparable to the ratio of the regression line slopes for each sample and these values are summarized in table 4.3. These average values are noteworthy because the cancerous sample has an average gain value than that of the benign sample, suggesting a possible connection between the additional contrast mechanism(s) specific to DEI and the presence of cancer. Furthermore, the peak gain for both samples is approximately 1.5 for the larger calcifications. The two samples also tend to have higher gain values as the size decreases, with a local maximum around 0.2 – 0.25 mm. A similar feature was noted previously with DEI images of nylon wires (Kiss et al, in press). This behavior is explained in the following manner. Absorption tends to dominate in the larger calcifications since in this case the x-rays travel a longer path through the object and therefore undergo greater attenuation. Larger calcifications attenuate more radiation through

absorption than smaller ones, which in turn results in high contrast, while little improvement is achieved using DEI. As the size of the calcification is decreased, so is the path length through it, resulting in proportionally lower attenuation through absorption and scatter rejection (refraction) becomes the dominant contrast mechanism for DEI.

It is also noteworthy that the refraction gain values was approximately independent of the size of the calcifications in all three samples, with average values of 1.01 in sample 1 and 1.2 in sample 2. These follow the same trend as the peak gain, when comparing benign and cancerous samples. Calcifications will scatter more radiation than a homogeneous object such as fishing line, so the refraction contrast from a calcification will be smaller than that from a nylon wire.

Calcifications that are 0.14 mm in size and smaller may give misleading results in the contrast and gain values. The FWHM value of the point spread function for the detector is approximately 0.14 mm (Kiss et al, 2002), which will limit the accuracy in which the sizes of these small objects can be determined. Therefore, the error in the size measurement tends to be about the size estimate. It is expected that the gain value will decrease from the stated levels for near pixel-sized calcifications. This too is noteworthy because it implies a lower limit on detectability of small objects depends greatly on the detector characteristics, most notably the PSF.

4.5 Conclusions

Studies have been conducted on calcifications in breast tissue specimens to compare the contrast rendered by synchrotron-based DEI to conventional synchrotron-based radiography. The results show an improvement in contrast for diffraction enhanced images over radiographs, especially for the DEI peak images. The gain values for the calcifications

were consistently greater than unity, indicating that the DEI technique is clearly capable of resolving contrast mechanisms associated with the calcifications that normal radiography cannot. Although this gain level decreases for pixel-sized objects, the improved contrast for even the smallest calcifications can provide an additional clinical tool in diagnostic screening. With the possible indicator that calcifications associated with malignancy had higher gain values than those associated with benign processes, future efforts should concentrate on resolving these differences and determining what link exists between image contrast and disease.

Acknowledgements

The authors wish to thank Gene Johnston, and Elodia Cole of the University of North Carolina, and Dean Chapman of the Illinois Institute of Technology for their assistance and useful suggestions. This work was funded in part by the US Army under grant DAMD 17-99-1-9329 and US DOE contract DE-AC02-CH10886. This research has been carried out in part at the National Synchrotron Light Source, Brookhaven National Laboratory, which is supported by the U.S. Department of Energy, Division of Materials Sciences and Division of Chemical Sciences.

References

Bazzani A., Bevilacqua A., Bollini D., Brancaccio R., Campanini R., Lanconelli N., Riccardi A., Romani D., “An SVM classifier to separate false signals from microcalcifications in digital mammograms,” *Physics in Medicine and Biology* 46 (2001) 1651 – 1663.

Brake G.M., Karssenmeijer N., “Single and multiscale detection of masses in digital mammograms,” *IEEE Transactions on Medical Imaging*, 18 (1999) 628 – 639.

Carroll F.E., Waters J.W., Andrews W.W., Price R.R., Pickens D.R., Willcott R., Tompkins P., Roos C., Page D., Reed G., Ueda A., Bain R., Wang P., Bassinger M., “Attenuation of monochromatic x-rays by normal and abnormal breast tissues,” *Investigative Radiology* **29** (1994) 266 - 272.

Chapman D., Thomlinson W., Johnston R.E., Washburn D., Pisano E., Gmur N., Zhong Z., Menk R., Arfelli F., and Sayers D., “Diffraction Enhanced x-ray Imaging,” *Phys. Med. Biol.* **42** (1997) 2015-2025.

Chen C.H., Lee G.G., “Digital mammogram segmentation and microcalcification detection using multiresolution wavelet analysis,” *Graphical Models and Image Processing* 59 (1997) 349 – 364.

Cheng H.-D. Lui Y.M., “A novel approach to microcalcification detection using fuzzy logic technique,” *IEEE Transactions on Medical Imaging* **17** (1998) 442 – 450.

Cowen A.R., Launders J.H., Jadav M., Brettle D.S., “Visibility of microcalcifications in computer and film-screen mammography,” *Physics in Medicine and Biology* **42** (1997) 1533 - 1548.

Fandos-Morera A., Prats-Esteve M., Tura-Soteras J.M., Traveria-Cros A., “Breast tumors: composition of microcalcifications,” *Radiology* **169** (1988) 325 – 327.

Galkin M.G., Feig S.A., Patchefsky A.S., Rue J.W., Gamblin W.J., Gomez D.G., Marchant L.M., “Ultrastructure and microanalysis of ‘benign’ and ‘malignant’ breast calcifications,” *Radiology* **124** (1977) 245 – 249.

Galkin M.G., Frasca P, Feig S.A., Holderness K.E., “Non-calcified breast particles: a possible new marker for breast cancer,” *Investigative Radiology* **17** (1982) 119 – 128.

Gavrielides M.A. Lo J.Y., Vargas-Voracek R., Floyd C.E., “Segmentation of suspicious clustered microcalcifications,” *Medical Physics* **27** (2000) 13 – 22.

Giger M.L., “Computer-aided diagnosis of breast lesions in medical images,” *Computing in Science and Engineering*, Sep/Oct 1999 39 – 45.

Hasnah M.O., Zhong Z., Oltulu O., Pisano E., Johnston R.J., Sayers, D.E., Thomlinson W., Chapman D., “Diffraction enhanced imaging contrast mechanism in breast cancer specimens,” *Medical Physics*, **29** (2002) 2216 – 2221.

Keyrilainen J., Fernandez M., Suortti P., “Refraction contrast in x-ray imaging,” *Nucl. Instr. and Meth. A*, **480** (2002) 419-427.

Kiss M.Z., Sayers D.E., Zhong Z., “Comparison of digital detectors for integration into a diffraction-enhanced imaging system,” *Nucl. Instr. and Meth. A* **491** (2002) 280 – 290.

Kiss M.Z. Sayers D.E., Zhong Z., “Measurement of image contrast using diffraction enhanced imaging,” submitted, *Physics in Medicine and Biology*.

Netsch T., Peitgren H.-O., "Scale-space signatures for the detection of clustered microcalcifications in digital mammograms," *IEEE Transactions on Medical Imaging* **18** (1999) 774 – 786.

Olson S.L., Fam B.W. Winter P.F., Scholz F.J., Lee A.K., Gordon S.E., "Breast calcifications: analysis of imaging properties," *Radiology* **169** (1988) 329 – 332.

Pisano E.D., Johnston R.E., Chapman D., Geradts J., Iacocca M., Livasy C.A., Washburn D.B., Sayers D.E., Zhong Z., Kiss M.Z., Thomlinson W.C., "Human Breast Cancer Specimens: Diffraction Enhanced Imaging with Histologic Correlation – Improved Conspicuity of Lesion Detail Compared with Digital Radiography," *Radiology* **214** (2000) 895-901.

Radi M.J., "Calcium Oxalate Crystals in Breast Biopsies," *Arch. Pathol. Lab Med.* **113** (1989) 1367-1369.

Surratt J.T., Monsees B.S., Mazoujian G., "Calcium oxalate microcalcifications in the breast," *Radiology* **181** (1991) 141 – 142.

Wang T.C., Karayiannis N.B., "Detection of microcalcifications in digital mammograms using wavelets," *IEEE Transactions on Medical Imaging* **17** (1998) 498 – 509.

Winston J.S., Yeh I.-T., Evers K, Friedman A.K., "Calcium oxalate is associated with benign breast tissue: can we avoid biopsy?" *Anatomic Pathology* **100** (1993) 488 – 492.

Zachariasen, W.H., *Theory of X-Ray Diffraction in Crystals* (1945), Dover, New York.

Zhong Z., Thomlinson W., Chapman D., Sayers D., "Implementation of Diffraction Enhanced Imaging Experiments at the NSLS and APS," *Nucl. Instr. and Meth. A*, **450** (2000) 556-567.

Chapter 5. Conclusions and a Look to the Future.

It has been hypothesized elsewhere that the current state of art for screening mammography is in need of updating and that improvements to the technology may have a profound impact on the medical community's early detection capabilities. This dissertation lends credence to this hypothesis. It has been demonstrated that DEI images of breast tissue samples exhibit improved contrast when compared to conventional radiographs. The level of improvement, commonly called the DEI gain, arises from the exploitation of additional contrast mechanisms besides an object's attenuation, namely, scatter rejection, refraction, and extinction. Of particular note is the level of improvement for objects whose size is on the order of a pixel. In radiographs, these objects tend to be barely discernible above the background, while in DEI images, the objects are more conspicuous.

The work does not end here. In order to advance mammography, the research has to pass out of the realm of proof-of-concept, and into pre-clinical and clinical trials. DEI can render calcifications in breast tissue samples more visible, but the relationship between calcifications and breast cancer is not well understood. The size, morphology, and arrangement of calcifications in breast tissue all are indicators of either benign or malignant processes. While a trained radiologist can make an educated guess from looking at a mammogram what a certain arrangement of calcifications may indicate, current imaging modalities are non-specific for chemical composition of calcifications. It is possible that DEI may provide some additional insight into the nature of calcifications without the need for biopsy. To determine this would require a thorough investigation into the imaging properties of calcifications, some of which has been listed in the literature. It would also require a more rigorous model for DEI than that used here. This dissertation was mainly concerned with an

object's image contrast, but to truly unlock the secrets of the objects in question would require a more thorough understanding of the relationships between x-rays, object being imaged and the diffraction optics. Several other steps need to be taken before DEI will become an accepted screening procedure for breast cancer. More systematic studies of DEI images to understand how it images different features in breast tissue, to determine the optimal parameters for imaging, and to develop analytical methods to reliably process and assess images will be needed. In addition, a source capable of doing DEI in a clinic must be developed. Elements of each of these efforts are being studied by other members of our DEI group.

Another challenge is less scientific and more psychological. We have successfully demonstrated a new imaging modality as a possible replacement for conventional mammography, which has remained essentially stagnant for more than 40 years. By indications from the recent Third Era of Hope meeting in Orlando, Florida (26 – 29 September 2002), there seems to be an institutionalized belief that the standard (screen-film mammography) works best and that new technology capable of detecting smaller and smaller lesions is unnecessary. Redefining the paradigm will be a herculean task to accomplish, given that human nature is resistant to change.

Chapter 6. Bibliography

Amemiya Y, Miyahara J, "Imaging Plates Illuminate Many Fields," *Nature* **336** (3) (1988) 89 – 90.

Amemiya, Yoshiyuki, "Imaging plate - x-ray area detector based on photostimulable phosphor," *Synchrotron Radiation News* **3** (2) (1990) 21 – 26.

American Cancer Society: <http://www.cancer.org>.

Antonuk M.J., Antonuk, Yaffe M.J., eds., *Medical Imaging 2001: Physics of Medical Imaging*, in *Medical Imaging 2001: Physics of Medical Imaging*. 2001, SPIE: San Diego, CA.

Arfelli F., Burns C., Chapman D., Gmür N., Johnston R.E., Menk R., Pisano E., Sayers D., Thomlinson W., Washburn D., Zhong Z., Data acquisition and analysis of mammography images at the NSLS June - August 1995. 1995, National Synchrotron Light Source - Brookhaven National Laboratory.

Baruchel J., Lodini A., Romanzetti S., Rustichelli F., Scrivani A., "Phase-contrast imaging of thin biomaterials," *Biomaterials* **22** (2001) 1515 – 1520.

Bazzani A., Bevilacqua A., Bollini D., Brancaccio R., Campanini R., Lanconelli N., Riccardi A., Romani D., "An SVM classifier to separate false signals from microcalcifications in digital mammograms," *Physics in Medicine and Biology* **46** (2001) 1651 – 1663.

Brake G.M., Karssenmeijer N., "Single and multiscale detection of masses in digital mammograms," *IEEE Transactions on Medical Imaging*, **18** (1999) 628 – 639.

Bushberg J.T., Seibert J.A., Leidholdt E.M., Boone J.M., *The Essential Physics of Medical Imaging*. Philadelphia: Lippincott, Williams & Wilkins, 1994.

Carroll F.E., Waters J.W., Andrews W.W., Price R.R., Pickens D.R., Willcott R., Tompkins P., Roos C., Page D., Reed G., Ueda A., Bain R., Wang P., Bassinger M., "Attenuation of monochromatic x-rays by normal and abnormal breast tissues," *Investigative Radiology* **29** (1994) 266 – 272.

Center for X-Ray Optics: <http://www-cxro.lbl.gov/>.

Chapman D., Pisano E., Thomlinson W., Zhong Z., Johnston R.E., Washburn D., Sayers D., Malinowska K., "Medical applications of diffraction enhanced imaging," *Breast Disease* **10** (3, 4) (1998) 197 – 207.

Chapman D., Thomlinson W., Johnston R.E., Washburn D., Pisano E., Gmür N., Zhong Z., Menk R., Arfelli F., Sayers D., "Diffraction enhanced x-ray imaging," *Physics in Medicine and Biology* **42** (1997) 2015 – 2025.

Chen C.H., Lee G.G., "Digital mammogram segmentation and microcalcification detection using multiresolution wavelet analysis," *Graphical Models and Image Processing* **59** (1997) 349 – 364.

Cheng H.-D. Lui Y.M., "A novel approach to microcalcification detection using fuzzy logic technique," *IEEE Transactions on Medical Imaging* **17** (1998) 442 – 450.

Colonna S., D'Acapito F., Mobilio S., Onori S., Pugliani L., Romanzetti S., Rustichelli F., "Curved Optics for x-ray phase contrast imaging by synchrotron radiation," *Phys. Med. Biol.* **46** (2001) 967 – 974.

Colonna S., D'Acapito F., Mobilio S., Onori S., Pugliani L., Romanzetti S., Rustichelli F., "Curved optics for x-ray phase contrast imaging by synchrotron radiation," *Physics in Medicine and Biology* **46** (2001) 967 – 974.

Cowen A.R., Launders J.H., Jadav M., Brettle D.S., "Visibility of microcalcifications in computer and film-screen mammography," *Physics in Medicine and Biology* **42** (1997) 1533 – 1548.

Eikenberry E.F., Tate M.W., Bilderback D.H., Gruner S.M., "X-ray detectors: comparison of film, storage phosphors and CCD detectors" in *Photoelectronic Image Devices 1991*. 1991. London: IOP.

Fandos-Morera A., Prats-Esteve M., Tura-Soteras J.M., Traveria-Cros A., "Breast tumors: composition of microcalcifications," *Radiology* **169** (1988) 325 – 327.

Fenner R.B., Picologlou S., Shenoy G.K., Eds., *Nobel Prizes for X-ray Science*. Argonne National Laboratory: Advanced Photon Source, 1999.

Galkin M.G., Feig S.A., Patchefsky A.S., Rue J.W., Gamblin W.J., Gomez D.G., Marchant L.M., "Ultrastructure and microanalysis of 'benign' and 'malignant' breast calcifications," *Radiology* **124** (1977) 245 – 249.

Galkin M.G., Frasca P, Feig S.A., Holderness K.E., "Non-calcified breast particles: a possible new marker for breast cancer," *Investigative Radiology* **17** (1982) 119 – 128.

Gavrielides M.A. Lo J.Y., Vargas-Voracek R., Floyd C.E., "Segmentation of suspicious clustered microcalcifications," *Medical Physics* **27** (2000) 13 – 22.

Giger M.L., "Computer-aided diagnosis of breast lesions in medical images," *Computing in Science and Engineering*, Sep/Oct (1999) 39 – 45.

Granfors P.R., Aufrichtig R., "Performance of a 41×41 cm² amorphous silicon flat panel x-ray detector for radiographic imaging applications," *Medical Physics* **27** (6) (2000) 1324 – 1331.

H. Fujita, D.-Y. Tsai, T. Itoh, K. Doi, J. Morishita, K. Ueda, A. Ohtsuka, "A simple method for determining the modulation transfer function in digital radiography," *IEEE Transactions on Medical Imaging* **11** (1) (1992) 34 – 39.

Harris J.R., Lippman M.E., Morrow M., Hellman S. Eds., *Diseases of the Breast*. Philadelphia: Lippincott-Raven, 1996.

Hasegawa B.H., *The Physics of Medical X-ray Imaging, 2d ed.* Madison: Medical Physics Publishing, 1991.

Hasnah M.O., Zhong Z., Oltulu O., Pisano E., Johnston R.J., Sayers, D.E., Thomlinson W., Chapman D., "Diffraction enhanced imaging contrast mechanism in breast cancer specimen," *Medical Physics*, **29** (2002) 2216 – 2221.

Hempel C., "Bright idea – scientists seek a better look at cancer," *The News & Observer*, 17 April 2000, 1D.

Ingal V.N., Beliaevskaya E.A., Brianskaya A.P., Merkurieva R.D., "Phase mammography – a new technique for breast investigation," *Phys. Med. Biol.* **43** (1998) 2555 – 2567.

Ishisaka A., Hiromu O., Honda C., "A new method of analyzing edge effect in phase contrast imaging with incoherent x-rays," *Optical Review* **7** (2000) 566 – 572.

Janesick J.R. Elliot T., Collins S., Blouke M.M., "Scientific charge-coupled devices," *Optical Engineering* **26** (8) (1987) 692 – 714.

Jee K.-W., Antonuk L. E., el-Mohri Y., Maolinbay M., Zhao Q., "Evaluation of direct detection and indirect detection active matrix flat-panel imagers (AMFPIs) for digital mammography" in *Medical Imaging 2001: Physics of Medical Imaging*. 2001. San Diego, CA: SPIE.

Keyrilainen J., Fernandez M., Suortti P., "Refraction contrast in x-ray imaging," *Nucl. Instr. and Meth. A*, **480** (2002) 419 – 427.

Kiss M.Z. Sayers D.E., Zhong Z., "Measurement of image contrast using diffraction enhanced imaging," in press, *Physics in Medicine and Biology*.

Kiss M.Z., Sayers D.E., Zhong Z., "Comparison of digital detectors for integration into a diffraction-enhanced imaging system," *Nucl. Instr. and Meth. A*, **491** (2002) 280 – 290.

Kotre C.J., Birch I.P., "Phase contrast enhancement of x-ray mammography: a design study," *Phys. Med. Biol.* **46** (1999) 2853 – 2866.

Nass S.J., Henderson C., Lashof J.C., eds., *Mammography and Beyond: Developing Technologies for the Early Detection of Breast Cancer*. Washington: National Academy Press, 2001.

National Breast Cancer Foundation: <http://www.nationalbreastcancer.org>.

National Synchrotron Light Source: <http://nslsweb.nsls.bnl.gov/nsls/Default.htm>.

Netsch T., Peitgren H.-O., "Scale-space signatures for the detection of clustered microcalcifications in digital mammograms," *IEEE Transactions on Medical Imaging* **18** (1999) 774 – 786.

Olson S.L., Fam B.W. Winter P.F., Scholz F.J., Lee A.K., Gordon S.E., "Breast calcifications: analysis of imaging properties," *Radiology* **169** (1988) 329 – 332.

Pisano E.D., Johnston R.E., Chapman D., Geradts J., Iacocca M., Livasy C.A., Washburn D.B., Sayers D.E., Zhong Z., Kiss M.Z., Thomlinson W.C., "Human Breast Cancer Specimens: Diffraction Enhanced Imaging with Histologic Correlation – Improved Conspicuity of Lesion Detail Compared with Digital Radiography," *Radiology* **214** (2000) 895 – 901.

Radi M.J., "Calcium Oxalate Crystals in Breast Biopsies," *Arch. Pathol. Lab Med.* **113** (1989) 1367 – 1369.

S.E. Reichenbach, S.K. Park, R. Narayanswamy, "Characterizing digital image acquisition devices," *Optical Engineering* **30** (2) (1991) 170 – 177.

Samel E., Flynn M.J., "A method for measuring the presampled MTF of digital radiographic systems using an edge test device," *Medical Physics* **25** (1) (1998), 102 – 113.

Singletary S.E., *Breast Cancer*. New York: Springer, 1999.

Smith, Steven W., *The Scientist and Engineer's Guide to Digital Signal Processing*, 2d Ed. 1999, San Diego: California Technical Publishing.

Surratt J.T., Monsees B.S., Mazoujian G., "Calcium oxalate microcalcifications in the breast," *Radiology* **181** (1991) 141 – 142.

Vedantham S., Karellas A., Suryanarayanan S., Albagli D., Han S., Tkaczyk E.J., Landberg C.E., Opsahl-Ong B., Granfors P.R., Levis I., D'Orsi C.J., Hendrick R.E., "Full breast digital mammography with an amorphous silicon-based flat panel detector: Physical characteristics of a clinical prototype," *Medical Physics* **27** (3) (2000) 558 – 567.

Wang T.C., Karayiannis N.B., "Detection of microcalcifications in digital mammograms using wavelets," *IEEE Transactions on Medical Imaging* **17** (1998) 498 – 509.

Warren, B.E., *X-Ray Diffraction*. New York: Dover, 1969.

Williams M.B. Fajardo L.L., Otto G.P., Tran J.M., "Evaluation of a prototype detector for full breast digital mammography with CCDs and modified Schmidt camera optics," *RSNA Electronic Journal* **1** (1997).

Winston J.S., Yeh I.-T., Evers K, Friedman A.K., "Calcium oxalate is associated with benign breast tissue: can we avoid biopsy?" *Anatomic Pathology* **100** (1993) 488 – 492.

Yaffe M.J. Rowlands J.A., "X-ray detectors for digital radiography," *Physics in Medicine and Biology* **42** (1997) 1 – 39.

Yaffe, M.J., "New trends in the development of detectors for digital radiography," *Physica Medica Supplement 1* **13** (1997) 203 – 210.

Z. Zhong, W. Thomlinson, D. Chapman, D. Sayers, "Implementation of diffraction-enhanced imaging experiments at the NSLS and APS," *Nuclear Instruments & Methods in Physics Research Section A* **450** (2000) 556 – 567.

Zachariasen, W.H., *Theory of X-Ray Diffraction in Crystals*. New York: Dover, 1945.

Zhong Z., Thomlinson W., Chapman D., Sayers D., "Implementation of Diffraction Enhanced Imaging Experiments at the NSLS and APS," *Nucl. Instr. and Meth. A*, **450** (2000) 556 – 567.

Appendix A. IDL Code for modeling DEI images of cylindrical objects

The following program was created using IDL version 5.3. Code for various customized subroutines are also provided as these are not generally available to the IDL community.

A.1 Program DEI2D

```
PRO dei2D, R0

; A modeling program to consider to path dependent intensity through a
; Lucite cylinder accounting for a finite (synchrotron) source and
; imperfect detector (limited by PSF and noise)

COMMON PARAMETERS1, n1, n2, I0, theta1C, n12, alpha1, alpha2
COMMON PARAMETERS2, radius, zms, zss, zsd, zsdR
COMMON PARAMETERS3, bottom, top, center
COMMON PARAMETERS4, radiobkg, peakbkg, lowbkg, highbkg, sumbkg, difbkg
COMMON ROCKINGCURVE, theta, RC, nrc, thetamin, thetamax, RCMax
COMMON FARBEN, red, green, blue, magenta, black, white

InitialTime = SYSTIME(1)
PRINT, 'Initializing Program...'
floatdir = 'E:\Mammography\Calcifications\Floats\'

!P.FONT = 1
DEVICE, SET_FONT = 'Helvetica', /TT_FONT

; Define colors for graphics
red = Color_Value(255, 0, 0)
green = Color_Value(0, 255, 0)
blue = Color_Value(0, 0, 255)
magenta = Color_Value(255, 0, 255)
black = Color_Value(0, 0, 0)
white = Color_Value(255, 255, 255)
yellow = Color_Value(255, 255, 0)

!P.MULTI = 0

filename = 'xxxx'

;R0 = 1.5 ;in cm
R0 = ROUND(R0*1.E+6)/1.E+6 ; for 0.1 cm or larger, use 1.e4

radius = R0
D0 = 2*R0 ; diameter

cmPerPixel = 0.005
cmPerPixel = ROUND(cmPerPixel*1.E+3)/1.E+3
tiny = 1.E-10
PixelFactor = D0/cmPerPixel ; ratio of diameter to pixel

IF (PixelFactor LT 1.) THEN PixelFactor = ROUND(PixelFactor*100.)/100.
IF (PixelFactor GE 1. AND PixelFactor LT 10.) THEN $
    PixelFactor = ROUND(PixelFactor*1000.)/1000.
```

```

IF (PixelFactor GE 10.) THEN PixelFactor = ROUND(PixelFactor*10.)/10.

PRINT, '...Loading analyzer crystal data...'
datadir = 'E:\Mammography\DEI model\'
infile = 'si333rcB.dat'
npts = 20001
theta = FLTARR(npts)
RC = FLTARR(npts)
OPENR, 1, datadir + infile
FOR j = 0, npts - 1 DO BEGIN
    READF, 1, thetaj, rcj
    theta[j] = thetaj
    RC[j] = rcj
ENDFOR
CLOSE, 1

j0 = 9132 ; theta = -249.947
j1 = 10868 ; theta = 249.947

theta = theta[j0:j1]
RC = RC[j0:j1]
nrc = N_ELEMENTS(theta)

thetamin = MIN(theta)
thetamax = MAX(theta)
;Use a Lorentzian to estimate the rocking curve in the wings

RCmax = MAX(RC)
RChigh = ANALYZE(0., 2)
RClow = ANALYZE(0., 0)

TimeStep0 = SYSTIME(1)
PRINT, 'Time Step 0 = ', TimeStep0 - InitialTime
PRINT, 'Cumulative Time = ', TimeStep0 - InitialTime

;stop
factor = 1
; factors:  0 - PMMA in air
;           1 - Nylon in air
; delta1 - sample bulk
; delta2 - sphere in bulk
; mac1, rho1 - mass attenuation coefficient (mu/rho), density of bulk
; mac2, rho2 - mass attenuation coefficient, density of sphere
; values for delta are for 18 keV
; fluxR - radiograph, fluxP - peak, fluxS - side images
CASE factor OF
    0: BEGIN ; PMMA in air
        delta2 = 8.23039E-07 & mac2 = 0.5403 & rho2 = 1.19 ; PMMA
object
;         fluxR = 1.E+07 & fluxP = 1.E+07 & fluxS = 1.E+07
;         fluxR = 8.216E+06 & fluxP = fluxR & fluxS = fluxP
;         etaP = 0.01 & etaS = 0.01 & etaR = 0.01 & etaD = 0.01
;         etaP = 0.017 & etaS = 0.017 & etaR = 0.014 & etaD = 0.0124
        END
    1: BEGIN ; Nylon in air

```

```

        delta2 = 8.00837E-07 & mac2 = 0.540640 & rho2 = 1.14 ; nylon
object
;
        fluxR = 1.E+07 & fluxP = 1.E+07 & fluxS = 1.E+07
        fluxR = 9.64E+06 & fluxP = 4.38E+06 & fluxS = fluxP ;
3.542E+06
;
        etaP = 0.01 & etaS = 0.01 & etaR = 0.01 & etaD = 0.01
;
        etaP = 0.0151 & etaS = 0.017 & etaR = 0.0117 & etaD = 0.0216
        etaP = 0.014 & etaS = 0.030 & etaR = 0.010 & etaD = 0.015
        END
ENDCASE

delta1 = 7.70121E-10 ; refractive index factor in incident region
mac1 = 0.875415282
rho1 = 1.204E-03 ; density in incident region

alpha1 = mac1*rho1 ; attenuation coefficient in incident regime (in units
of cm^-1)
alpha2 = mac2*rho2

n1 = 1. - delta1; refractive index for incident regime
n2 = 1. - delta2 ; refractive index in object

n12 = n1/n2

IF (n1 GT n2) THEN BEGIN
        theta1C = ASIN(1./n12)
ENDIF ELSE BEGIN
        theta1C = !Pi/2. ; Incident critical angle
ENDELSE

yCritical = R0/n12
center = 0.
top = R0
bottom = -R0

yCritical0 = ABS(R0 - yCritical)

dx = cmPerPixel

IF (R0 GE 1.) THEN BEGIN
        xmin = -2. & xmax = 2.
        ymin = -2. & ymax = 2.
ENDIF ELSE BEGIN
        xmin = -1. & xmax = 1.
        ymin = -1. & ymax = 1.
ENDELSE

nx = LONG((xmax - xmin)/dx + 1)
x = FINDGEN(nx)*dx + xmin ; x coordinate in object plane
xR = (xmax - R0)/2.
xc = (xmin + xmax)/2.
yc = (ymin + ymax)/2.

dy0 = cmPerPixel
ny0 = ROUND((bottom - ymin)/dy0 + 1) ; region below wire

```

```

IF (PixelFactor LE 1.) THEN ny1 = CEIL(PixelFactor)*100 + 1

IF (PixelFactor GT 1. AND PixelFactor LE 2.) THEN ny1 = (CEIL(PixelFactor)
+ 1)*100 + 1
IF (PixelFactor GT 2. AND PixelFactor LT 10.) THEN ny1 =
CEIL(PixelFactor)*100 + 1

IF (PixelFactor GE 10.) THEN BEGIN
    ny1 = 2001
    IF (ROUND(PixelFactor) MOD 6 EQ 0) THEN ny1 = 1801
    IF (ROUND(PixelFactor) MOD 16 EQ 0) THEN ny1 = 2401
ENDIF

ny2 = ny0 ; region above wire

ny = ny0 + ny1 + ny2

IF (PixelFactor GT 1. AND PixelFactor LE 2.) THEN $
    dy1 = FLOAT(CEIL(PixelFactor) + 1)*dy0/FLOAT(ny1 - 1) $
ELSE dy1 = FLOAT(CEIL(PixelFactor))*dy0/FLOAT(ny1 - 1)

IF (PixelFactor LT 1.) THEN BEGIN
    y0axis = -dy0 - FINDGEN(ny0)*dy0 & y0axis = REVERSE(y0axis)
    y1axis = FINDGEN(ny1)*dy1 - dy0/2.
    y2axis = FINDGEN(ny2)*dy0 + dy0
ENDIF

IF (PixelFactor GT 1. AND PixelFactor LE 2.) THEN BEGIN
    y1axis = FINDGEN(ny1)*dy1 - FLOAT(CEIL(PixelFactor) + 1)/2.*dy0
    y0axis = MIN(y1axis) - dy0/2. - FINDGEN(ny0)*dy0 & y0axis =
REVERSE(y0axis)
    y2axis = FINDGEN(ny2)*dy0 + MAX(y1axis) + dy0/2.
ENDIF

IF (PixelFactor EQ 1 OR PixelFactor GT 2.) THEN BEGIN
    y1axis = FINDGEN(ny1)*dy1 - FLOAT(CEIL(PixelFactor))/2.*dy0
    y0axis = MIN(y1axis) - dy0/2. - FINDGEN(ny0)*dy0 & y0axis =
REVERSE(y0axis)
    y2axis = FINDGEN(ny2)*dy0 + MAX(y1axis) + dy0/2.
ENDIF

y = FINDGEN(ny)
y[0:ny0 - 1] = y0axis[*]
y[ny0:ny0 + ny1 - 1] = y1axis[*]
y[ny0 + ny1:ny0 + ny1 + ny2 - 1] = y2axis[*]

PRINT, 'dimensions in cm'
PRINT, 'radius = ', R0, ' diameter = ', D0
PRINT, 'ymin = ', ymin, ' ymax = ', ymax
PRINT, 'bottom = ', bottom, ' top = ', top
PRINT, 'ycritical0 = ', ycritical0
PRINT, ' '
PRINT, 'dimensions in microns'
PRINT, 'dx = ', dx*1.E+04
PRINT, 'dy0 = ', dy0*1.E+04, ' dy1 = ', dy1*1.E+04
PRINT, 'Pixel Factor = ', PixelFactor

```

```

PRINT, ' '
PRINT, 'nx = ', nx, '      ny0 = ', ny0, '      ny1 = ', ny1, '      ny2 = ',
ny2
PRINT, ' '
PRINT, 'axis      n      part of ny min      max'
PRINT, 'y0:', ny0, 0, ' -', ny0 - 1, MIN(y0axis), MAX(y0axis)
PRINT, 'y1: ', ny1, ' ', ny0, ' -', ny0 + ny1 - 1, MIN(y1axis),
MAX(y1axis)
PRINT, 'y2:', ny2, ny0 + ny1, ' -', ny0 + ny1 + ny2 - 1, MIN(y2axis),
MAX(y2axis)
PRINT, 'ny = ', ny
;stop

zms = 40. ; Monochromator tank to sample distance in cm 50.
zss = 13000. ; Source to sample distance in cm
zsd = 90. ; Sample to detector distance in cm, Bragg mode 100.
zsdR = 5. ; Sample to detector distance in cm, radiograph 10.

Ms = zsd/zss ; Source magnification
Mo = 1. + Ms ; Object magnification

PixelArea = dx*dy0
PixelFluxR = fluxR*PixelArea ; average intensity of background
"photons/pixel"
PixelFluxP = fluxP*PixelArea
PixelFluxS = fluxS*PixelArea

;stop
I0 = 1.

thetaC = DEFLECT(ycritical)

TimeStep1 = SYSTIME(1)
PRINT, 'Time Step 1 = ', TimeStep1 - TimeStep0
PRINT, 'Cumulative Time = ', TimeStep1 - InitialTime

PRINT, '...run simulation...'
; The main loop for calculating everything
ni = 4 ; number of images per experiment
      ; 0 - minus image
      ; 1 - peak image
      ; 2 - plus image
      ; 3 - radiograph
deflection = FLTARR(ny)
Anglein = FLTARR(ny)
IntzR = FLTARR(ny) ; for sets are used, one for each image (includes
noise)
IntzD = FLTARR(ny) ; R - radiograph, D - DEI images (each has different
detector distance
Rtheta = FLTARR(ny, ni - 1)
detector = FLTARR(ny, ni - 1) ;

profile = FLTARR(ny)
yvalue = FLTARR(1)
ypoint1 = FLTARR(1)
ypoint2 = FLTARR(1)

```

```

ypoint3 = FLTARR(1)
ypoint4 = FLTARR(1)

WINDOW, 4

;PLOT, y, profile, /NODATA, YRANGE = [-thetac, thetac] ; for deflection
;PLOT, y, profile, /NODATA, YRANGE = [0., 1.] ; for intensity
PLOT, y, profile, /NODATA, YRANGE = [1.e-5, 1.], /YLOG ; for intensity,
log scale
;PLOT, y, profile, /NODATA, YRANGE = [ymin, ymax]

FOR j = 0L, ny - 1 DO BEGIN
  IF (j MOD 400 EQ 0) THEN PRINT, 'j = ', j, ' ', ny - 1 - j, ' left
to go'
  yj = y[j] ; Beam height variable

  IF (yj LE bottom) OR (yj GE top) THEN BEGIN
    ; ray does not intersect region of interest
;    z1 = D0
;    I1 = I0*EXP(-alpha1*z1) ; Intensity exiting from sample
    I4d = I0*EXP(-alpha1*(zms + D0 + zsd))
    I4r = I0*EXP(-alpha1*(zms + D0 + zsdR))
    Intzdj = I4d
    Intzrj = I4r
    angleinj = 0.
    deflxnj = 0. ; deflection angle

    lowvalj = RClow
    peakvalj = RCmax
    highvalj = RChigh
;    PRINT, 'j = ', j, ' yj = ', yj
  ENDIF ELSE BEGIN
    Intzdj = INTENSITY(yj, zsd) ; Calculate the path-dependent
intensity profile
    Intzrj = INTENSITY(yj, zsdR)

    angleinj = ASIN(yj/R0)
    deflxnj = DEFLECT(yj) ; Calculate the deflection profile

    lowvalj = ANALYZE(deflxnj, 0)
    peakvalj = ANALYZE(deflxnj, 1)
    highvalj = ANALYZE(deflxnj, 2)
;    IF (j GT 1130 AND j LE 1150) THEN $
;    PRINT, 'j = ', j, ' y = ', yj, ' intzr = ', intzrj, '
defl = ', deflxnj
;    PRINT, ' low = ', lowvalj, ' hi = ', highvalj, ' peak
= ', peakvalj
  ENDELSE

  Rtheta[j, 0] = lowvalj
  Rtheta[j, 1] = peakvalj
  Rtheta[j, 2] = highvalj

  IntzR[j] = Intzrj
  IntzD[j] = Intzdj
  deflection[j] = deflxnj

```

```

    anglein[j] = angleinj

    yvalue[0] = yj
    ypoint1[0] = Deflection[j]
    ypoint2[0] = IntzDj*peakvalj
    ypoint3[0] = IntzR[j]

    IF (j MOD 100 EQ 0) THEN BEGIN
        colortype = red
        symboltype = 4
    ENDIF ELSE BEGIN
        colortype = green
        symboltype = 3
    ENDELSE
;    IF ypoint1[0] GT 1.e3 THEN PRINT, 'j = ', j, ' y = ', yj, ' ypoint
= ', ypoint1[0]
;    IF ypoint1[0] LT -1.e3 THEN PRINT, 'j = ', j, ' y = ', yj, '
ypoint = ', ypoint1[0]
        OPLOT, yvalue, ypoint2, PSYM = symboltype, COLOR = colortype
;    OPLOT, yvalue, ypoint1, PSYM = 3, COLOR = green
;    OPLOT, yvalue, ypoint4, PSYM = symboltype, COLOR = colortype

ENDFOR

TimeStepla = SYSTIME(1)
PRINT, 'Time to run loop = ', TimeStepla - TimeStep1
PRINT, 'Cumulative Time = ', TimeStepla - InitialTime

PRINT, ' '

PeakP = IntzD*Rtheta[*, 1]
LowP = IntzD*Rtheta[*, 0]
HighP = IntzD*Rtheta[*, 2]
stop
PkW = PeakP[ny0:ny0 + ny1 - 1]
LoW = LowP[ny0:ny0 + ny1 - 1]
HiW = HighP[ny0:ny0 + ny1 - 1]
RadW = IntzR[ny0:ny0 + ny1 - 1]
ReduceProfile, PixelFactor, ny1, PkW, Pk1
ReduceProfile, PixelFactor, ny1, LoW, Lo1
ReduceProfile, PixelFactor, ny1, HiW, Hi1
ReduceProfile, PixelFactor, ny1, RadW, Rad1
;ReduceProfile, PixelFactor, ny1, DefW, Def1

nylw = N_ELEMENTS(Pk1)
IF nylw EQ 1 THEN BEGIN
    yal = FLTARR(1) & yal[0] = 0.
ENDIF ELSE BEGIN
    IF (PixelFactor GT 2.) THEN $
        yal = FINDGEN(nylw)*dy0 + MIN(ylaxis) + dy0/2. $
    ELSE yal = FINDGEN(nylw)*dy0 - dy0
ENDELSE
;stop
nye = ny0 + nylw + ny2

Pk = FLTARR(nye)

```

```

Pk0 = PeakP[0:ny0 - 1]
Pk2 = PeakP[ny0 + nyl:ny - 1]
Pk[0:ny0 - 1] = Pk0[*]
Pk[ny0:ny0 + nylw - 1] = Pk1[*]
Pk[ny0 + nylw:nye - 1] = Pk2[*]

Lo = FLTARR(nye)
Lo0 = LowP[0:ny0 - 1]
Lo2 = LowP[ny0 + nyl:ny - 1]
Lo[0:ny0 - 1] = Lo0[*]
Lo[ny0:ny0 + nylw - 1] = Lo1[*]
Lo[ny0 + nylw:nye - 1] = Lo2[*]

Hi = FLTARR(nye)
Hi0 = HighP[0:ny0 - 1]
Hi2 = HighP[ny0 + nyl:ny - 1]
Hi[0:ny0 - 1] = Hi0[*]
Hi[ny0:ny0 + nylw - 1] = Hi1[*]
Hi[ny0 + nylw:nye - 1] = Hi2[*]

Rad = FLTARR(nye)
Rad0 = IntzR[0:ny0 - 1]
Rad2 = IntzR[ny0 + nyl:ny - 1]
Rad[0:ny0 - 1] = Rad0[*]
Rad[ny0:ny0 + nylw - 1] = Rad1[*]
Rad[ny0 + nylw:nye - 1] = Rad2[*]

yImg = FLTARR(nye)
ya0 = y0axis
ya2 = y2axis
yImg[0:ny0 - 1] = ya0[*]
yImg[ny0:ny0 + nylw - 1] = ya1[*]
yImg[ny0 + nylw:nye - 1] = ya2[*]

;stop
showme = 0
IF showme THEN BEGIN
    gray = Color_Value(125, 125, 125)
    IF (PixelFactor LT 10.) THEN BEGIN
        xr0 = bottom - dy0
        xr1 = top + dy0
    ENDIF ELSE BEGIN
        xr0 = 1.1*bottom
        xr1 = 1.1*top
    ENDELSE

    IF (PixelFactor LE 1.) THEN BEGIN
        nlines = 2
        pb = FINDGEN(nlines)*dy0 - dy0/2.
    ENDIF

    IF (PixelFactor GT 1. AND PixelFactor LE 2.) THEN BEGIN
        nlines = CEIL(PixelFactor) + 2
        pb = FINDGEN(nlines)*dy0 - 3.*dy0/2.
    ENDIF

```

```

IF (PixelFactor GT 2.) THEN BEGIN
    nlines = CEIL(PixelFactor) + 1
    pb = FINDGEN(nlines)*dy0 - FLOAT(CEIL(PixelFactor))/2.*dy0
ENDIF

WINDOW, 5
PLOT, y, peakp, xrange = [xr0, xr1], xstyle = 1, $
    yrange = [MIN(peakp), 1.], ystyle = 1, /ylog, linestyle = 1
OPLOTT, ya1, pk1, color = blue, psym = 2

IF (PixelFactor LE 10.) THEN BEGIN
    FOR j = 0, nlines - 1 DO BEGIN
        PLOTS, [pb[j], pb[j]], [MIN(peakp), 1.], COLOR = gray,
/ DATA
        ENDFOR
    ENDFIF

;stop
WINDOW, 6
PLOT, y, Lowp, xrange = [xr0, xr1], xstyle = 1, $
    yrange = [1.e-4, 1.], ystyle = 1, /ylog, linestyle = 1
OPLOTT, y, Highp, linestyle = 1
OPLOTT, ya1, lo1, color = green, psym = 2
OPLOTT, ya1, hi1, color = blue, psym = 2
IF (PixelFactor LE 10.) THEN BEGIN
    FOR j = 0, nlines - 1 DO BEGIN
        PLOTS, [pb[j], pb[j]], [1.e-4, 1.], COLOR = gray, / DATA
    ENDFOR
ENDIF

WINDOW, 7
PLOT, y, Intzr, xrange = [xr0, xr1], xstyle = 1, $
    yrange = [Min(intzr), max(intzr)], linestyle = 1
OPLOTT, ya1, Rad1, color = blue, psym = 2

IF (PixelFactor LE 10.) THEN BEGIN
    FOR j = 0, nlines - 1 DO BEGIN
        PLOTS, [pb[j], pb[j]], [min(intzr), max(intzr)], COLOR =
gray, / DATA
    ENDFOR
ENDIF

;stop
ENDIF
;stop
TimeStep2 = SYSTIME(1)
PRINT, 'Time Step 2 = ', TimeStep2 - TimeStep1a
PRINT, 'Cumulative Time = ', TimeStep2 - InitialTime

TimeStep3 = SYSTIME(1)
PRINT, 'Time Step 3 = ', TimeStep3 - TimeStep2
PRINT, 'Cumulative Time = ', TimeStep3 - InitialTime
;stop

; Account for a finite source
PRINT, 'Accounting for a finite source...'
yImgmin = MIN(yImg)

```

```

XRAYSOURCE, dy0, source ; generates a beam profile

TimeStep4 = SYSTIME(1)
PRINT, 'Time Step 4 = ', TimeStep4 - TimeStep3
PRINT, 'Cumulative Time = ', TimeStep4 - InitialTime

PRINT, 'Convolving Object function with source function...'
RadS = CONVOL(Rad, source, /EDGE_TRUNCATE)
PkS = CONVOL(Pk, source, /EDGE_TRUNCATE)
LoS = CONVOL(Lo, source, /EDGE_TRUNCATE)
HiS = CONVOL(Hi, source, /EDGE_TRUNCATE)

PRINT, 'Accounting for detector PSF...'
PSFCalc, dy0, PSF
TimeStep5 = SYSTIME(1)
PRINT, 'Time Step 5 = ', TimeStep5 - TimeStep4
PRINT, 'Cumulative Time = ', TimeStep5 - InitialTime

PRINT, 'Convolving image with PSF...'
RadSP = CONVOL(RadS, PSF, /EDGE_TRUNCATE)
PkSP = CONVOL(PkS, PSF, /EDGE_TRUNCATE)
LoSP = CONVOL(LoS, PSF, /EDGE_TRUNCATE)
HiSP = CONVOL(Hi, PSF, /EDGE_TRUNCATE)
TimeStep6 = SYSTIME(1)
PRINT, 'Time Step 6 = ', TimeStep6 - TimeStep5
PRINT, 'Cumulative Time = ', TimeStep6 - InitialTime

PRINT, '...calculating absorption and refraction...'
Rh = ANALYZE(0., 2) & Rl = ANALYZE(0.,0)
dR = DERIV(theta, RC)
dRl = MAX(dR) & dRh = MIN(dR)

;difS = -RCmax/(2.*dRl)*(hiS - loS)/(hiS + loS)
difS = (hiS*Rl - loS*Rh)/(loS*dRh - hiS*dRl)
;difSP = -RCmax/(2.*dRl)*(hiSP - loSP)/(hiSP + loSP)
difSPa = (hiSP*Rl - loSP*Rh)/(loSP*dRh - hiSP*dRl)

TimeStep7 = SYSTIME(1)
PRINT, 'Time Step 7 = ', TimeStep7 - TimeStep6
PRINT, 'Cumulative Time = ', TimeStep7 - InitialTime

PRINT, '...Adding in Noise to images...'
ni = nye
lowlS = FLTARR(ni, nye)
highlS = FLTARR(ni, nye)
lowlSP = FLTARR(ni, nye)
peaklSP = FLTARR(ni, nye)
highlSP = FLTARR(ni, nye)
radiolSP = FLTARR(ni, nye)
diflSP = FLTARR(ni, nye)
FOR j = 0, nye - 1 DO BEGIN
    lowlS[* , j] = REPLICATE(loS[j], ni)
    highlS[* , j] = REPLICATE(hiS[j], ni)
    lowlSP[* , j] = REPLICATE(LoSP[j], ni)
    highlSP[* , j] = REPLICATE(HiSP[j], ni)
    peaklSP[* , j] = REPLICATE(PkSP[j], ni)

```

```

        radiolSP[* , j] = REPLICATE(RadSP[j], ni)
    ENDFOR

; Add in photon flux
Low1a = Low1SP/Low1SP[2]*Lo[0]*PixelFluxS
High1a = High1SP/High1SP[2]*Hi[0]*PixelFluxS
Peak1a = Peak1SP/Peak1SP[2]*Pk[0]*PixelFluxP
Radiola = RadiolSP/RadiolSP[2]*Rad[0]*PixelFluxR

ENBL = 0.00411 ; Electronic Noise baseline
EN0 = RANDOMN(seed0, ni, nye, /POISSON)*ENBL + ENBL
EN1 = RANDOMN(seed1, ni, nye, /POISSON)*ENBL + ENBL
EN2 = RANDOMN(seed2, ni, nye, /POISSON)*ENBL + ENBL
EN3 = RANDOMN(seed3, ni, nye, /POISSON)*ENBL + ENBL

low2 = low1a + EN0
peak2 = peak1a + EN1
high2 = high1a + EN2
radio2 = radiola + EN3
;dif2 = (high2*Rl - low2*Rh)/(low2*dRh - high2*dRl)
;dif2 = (low2 - high2)/((low2 + high2)/2.)
;dif2 = -RCmax/(2.*dRl)*(high2 - low2)/(high2 + low2)

; Now add in signal level dependent noise
; Noise is assumed normally distributed around a mean and
; is also dependent on the signal at each pixel. Empirical results
; indicate about 1.2% noise, so this is scaled by the value at each pixel
; create several of each for good statistics

noise0 = RANDOMN(s0, ni, nye)*PixelFluxS*etaS*radiolSP/MAX(radiolSP) ;
for low
noise1 = RANDOMN(s1, ni, nye)*PixelFluxP*etaP*radiolSP/MAX(radiolSP) ;
for peak
noise2 = RANDOMN(s2, ni, nye)*PixelFluxS*etaS*radiolSP/MAX(radiolSP) ;
for high
noise3 = RANDOMN(s3, ni, nye)*PixelFluxR*etaR*radiolSP/MAX(radiolSP) ;
for radio
noised = RANDOMN(s4, ni, nye)*etaD*radiolSP/MAX(radiolSP)
;stop
low3 = low2 + noise0 & low3 = low3 > MIN(EN0)
peak3 = peak2 + noise1 & peak3 = peak3 > MIN(EN1)
high3 = high2 + noise2 & high3 = high3 > MIN(EN2)
radio3 = radio2 + noise3 & radio3 = radio3 > MIN(EN3)

shiftx = 0. & shifty = 0. & shiftangle = 0.
;difS = DOSHIFT(shiftx, shifty, shiftangle, high1S, low1S, sum = sumS)
difSP = DOSHIFT(shiftx, shifty, shiftangle, high1SP, low1SP, sum = sumSP)
;dif1 = DOSHIFT(shiftx, shifty, shiftangle, high2, low2, sum = sum1)
;dif3 = dif1 + noised

;dif3 = dif2 + noised

stop
TimeStep8 = SYSTIME(1)
PRINT, 'Time Step 8 = ', TimeStep8 - TimeStep7
PRINT, 'Cumulative Time = ', TimeStep8 - InitialTime

```

```

;SHOWPLOTS,
PRINT, ' '
TV_Image, dif3, peak3, radio3

TimeStep9 = SYSTIME(1)
PRINT, 'Time Step 9 = ', TimeStep9 - TimeStep8
PRINT, 'Total Time = ', TimeStep9 - InitialTime

stop

END
;


---


FUNCTION DEFLECT, y

COMMON PARAMETERS1, n1, n2, I0, thetalC, n12, alpha1, alpha2
COMMON PARAMETERS2, radius, zms, zss, zsd, zsdR
COMMON PARAMETERS3, bottom, top, center

arg = (y - center)/radius
thetal = ASIN(arg) ; incident angle on wire

; For paths above or below the object
IF (y LE bottom OR y GE top) THEN BEGIN
    angle = 0. ; Intensity arriving at detector

    RETURN, angle
ENDIF

; For paths through the calc
IF (ABS(thetal) LT thetalC) THEN BEGIN
    angle = 2.*(n1 - n2)*TAN(thetal) ; deflection angle in radians
    angle = angle*1.E+06 ; convert to microradians

    RETURN, angle
ENDIF

; For path at critical reflection or above
IF (ABS(thetal) GE thetalC) AND (ABS(thetal) LT !Pi/2.) THEN BEGIN
    angle = !Pi - 2.*thetal
    angle = angle*1.E+06

    RETURN, angle
ENDIF

END

;


---


FUNCTION INTENSITY, y, zs

COMMON PARAMETERS1, n1, n2, I0, thetalC, n12, alpha1, alpha2
COMMON PARAMETERS2, radius, zms, zss, zsd, zsdR
COMMON PARAMETERS3, bottom, top, center

thetal = ASIN((y - center)/radius)
z1 = zms + radius*(1. - COS(thetal)) ; path from monochromator tank to

```

```

; sample, ; accounting for deviation
; from vertical
I1 = I0*EXP(-alpha*z1) ; Intensity incident on the wire

; For paths above or below the object
IF (y LE bottom OR y GE top) THEN BEGIN
    I4 = I0*EXP(-alpha*(zms + radius*2. + zs))

; Intensity arriving at detector
RETURN, I4
ENDIF

; For paths through the calc
IF (ABS(theta1) LT theta1C) THEN BEGIN
    z2 = 2.*SQRT(radius^2 - (y - center)^2) ; path in wire
    z3 = (2.*radius - z2)/2. + zs ; path from wire to detector

    I2 = I1*EXP(-alpha2*z2) ; Intensity exiting wire
    I3 = I2*EXP(-alpha1*z3) ; Intensity arriving at detector

    RETURN, I3
ENDIF

; For path at critical reflection or above
IF (ABS(theta1) GE theta1C) AND (ABS(theta1) LT !Pi/2.) THEN BEGIN
    z3 = radius + zs ; path from reflection point to detector

    I3 = I1*EXP(-alpha1*z3) ; Intensity arriving at detector

    RETURN, I3
ENDIF

END

;


---


FUNCTION ANALYZE, angle, snum

COMMON ROCKINGCURVE, theta, RC, nrc, thetamin, thetamax, RCMax

; FWHM of rocking curve
rcfwhm = 3.64

tune = 0.

CASE snum OF
    0: tune = -rcfwhm/2 ; low side
    1: tune = 0.
    2: tune = rcfwhm/2 ; high side
ENDCASE

delta = angle - tune

IF (delta LT thetamin) THEN BEGIN
    coefs = [RCmax, 4.65306, 0.756470]
    LORENTZ, delta, coefs, Refl
    RETURN, Refl
ENDIF

```

```

IF (delta GT thetamax) THEN BEGIN
    coefs = [RCmax, -3.99930, 0.755517]
    LORENTZ, delta, coefs, Refl
    RETURN, Refl
ENDIF

BiggerIndex = WHERE(theta GT delta)
nBI = N_ELEMENTS(BiggerIndex)
CASE nBI OF
    1: x1 = BiggerIndex[0]
    2: x1 = BiggerIndex[1]
    ELSE: x1 = BiggerIndex[2]
ENDCASE

SmallerIndex = WHERE(theta LT delta)
nSI = N_ELEMENTS(SmallerIndex)

CASE nSI OF
    1: x0 = 0
    2: x0 = SmallerIndex[nSI - 2]
    ELSE: x0 = SmallerIndex[nSI - 3]
ENDCASE

thetax = theta[x0:x1]
RCx = RC[x0:x1]

T = FLTARR(2)
T[0] = delta
T[1] = delta + 1.E-09
result = SPLINE(thetax, RCx, T)
Refl = result[0]

RETURN, Refl

END
;


---


PRO ReduceProfile, PF, ny1, yOld, yNew

IF (PF LE 1.) THEN BEGIN
    nyNew = 1
    yNew = FLTARR(1)
;
    yNew[0] = FLOAT(MEAN(yOld))
ENDIF

IF (PF GT 1. AND PF LE 2.) THEN BEGIN
    npixels = CEIL(PF) + 1
    yNew = FLTARR(npixels)
    npts = (ny1 - 1)/(npixels)
    FOR i = 0, npixels - 2 DO BEGIN ; exclude last pixel, which won't
                                    ; have the same number of points
        y0 = i*npts
        y1 = y0 + npts - 1
;        PRINT, 'i = ', i, ' y0 = ', y0, ' y1 = ', y1
        yNew[i] = MEAN(yOld[y0:y1])
    ENDFOR
ENDIF

```

```

        ENDFOR
;      ; Now, do the last pixel, which has more points than the others
        y0 = (npixels - 1)*npts
        y1 = y0 + npts
;      PRINT, 'i = ', i, ' y0 = ', y0, ' y1 = ', y1
        yNew[npixels - 1] = MEAN(yOld[y0:y1])
ENDIF

IF (PF GT 2.) THEN BEGIN
;      ; separate the points into pixel bins
        npixels = CEIL(PF) ; number of pixels
        yNew = FLTARR(npixels) ; the output
        npts = (ny1 - 1)/(npixels) ; number of points per pixel
        FOR i = 0, npixels - 2 DO BEGIN ; exclude last pixel, which won't
            ; have the same number of points
                y0 = i*npts
                y1 = y0 + npts - 1
;            PRINT, 'i = ', i, ' y0 = ', y0, ' y1 = ', y1
                yNew[i] = MEAN(yOld[y0:y1])
        ENDFOR
;      ; Now, do the last pixel, which has more points than the others
        y0 = (npixels - 1)*npts
        y1 = y0 + npts
;      PRINT, 'i = ', i, ' y0 = ', y0, ' y1 = ', y1
        yNew[npixels - 1] = MEAN(yOld[y0:y1])
ENDIF

END
;


---


PRO XRAYSOURCE, dy, light

COMMON PARAMETERS2, radius, zms, zss, zsd, zsdR
COMMON FARBEN, red, green, blue, magenta, black, white

fwhm = 0.0027 ;in cm

A0 = 1.
A2 = fwhm/2.
ymin = -6.*dy
ny = FIX(2.*(-ymin)/dy)
IF (ny MOD 2 EQ 1) THEN ny = ny + 1

y = FINDGEN(ny)*dy + ymin
light = FLTARR(ny)
FOR j = 0, ny - 1 DO BEGIN
    light[j] = A0*EXP(-y[j]^2/(2.*A2^2))
ENDFOR

END
;


---


PRO TV_IMAGE, dif, peak, radio

COMMON FARBEN, red, green, blue, magenta, black, white

TVSIZE, peak, TITLE = 'Peak'

```

```

TVSIZE, dif, TITLE = 'Refraction'
TVSIZE, radio, TITLE = 'radiograph'

END
;
PRO PSFcalc, dy, PSF

COMMON FARBEN, red, green, blue, magenta, black, white

; Image plate FWHM values for PSF
yfwhm = 0.0138; in cm ;

npsf = 21 ; increase to more points, 21?
IF (npsf MOD 2 EQ 0) THEN npsf = npsf + 1

PSF = FLTARR(npsf)

y = FINDGEN(npsf)*dy - FLOAT(npsf - 1)/2.*dy

A0 = 1.
A2 = yfwhm/2.
FOR j = 0, npsf - 1 DO BEGIN
    PSF[j] = A0*EXP(-y[j]^2/(2.*A2^2))
ENDFOR

; Normalize PSF so its integral equals 1.
PSF = PSF/TOTAL(PSF)

;stop
END

```

A.2. Procedure TVSIZE

```

pro tvsize, image, title=title
IF N_ELEMENTS(title) EQ 0 THEN title = ''
sz = SIZE(image)

IF sz[0] EQ 0 THEN BEGIN
    PRINT, "Warning: Image size = 0"
    return
ENDIF

px = sz[1] & py = sz[2]
nx = px & ny = py
WINDOW, /FREE, XSIZE = nx, YSIZE = ny, TITLE = title
TVSCL, image

END

```

A.3. Function DOSHIFT

```

function doshift, dx, dy, rotation, high, low, sum = sum

```

```

size_high = SIZE(high)
size_low = SIZE(low)

nx = size_high[1]
ny = size_high[2]

nx_slice = nx/5
ny_slice = ny/5

xs = [nx/10, 9* nx/10, nx/10, 9*nx/10]
ys = [ny/10, ny/10, 9*ny/10, 9*ny/10]

x0 = FLOAT(xs)
y0 = FLOAT(ys)

xc = FLOAT(nx/2.)
yc = FLOAT(ny/2.)

delta_x = xs - xc
delta_y = ys - yc

xi = xc + dx + delta_x*COS(rotation/!radeg) - $
      delta_y*SIN(rotation/!radeg)
yi = yc + dy + delta_x*SIN(rotation/!radeg) + $
      delta_y * COS(rotation/!radeg)

POLYWARP, xi, yi, x0, y0, 1, kx, ky

shifted_low = POLY_2D(low, kx, ky, 1)

shifted_low = shifted_low/MEDIAN(low)
my_high = high/MEDIAN(high)
;my_high = high

sum = (shifted_low + my_high)/2.
diff = (shifted_low - my_high)/sum/2.

;drdtheta = 3.05E+05
;Rp = 0.923358
;diffa = -Rp/(2.*drdtheta)*(my_high - shifted_low)/(my_high + shifted_low)
;stop
RETURN, diff

END

```

A.4. Function COLOR_VALUE.

```

; Created by M.Z. Kiss, 15 Sep 98
; Modified, 16 Sep 98
; COLOR_VALUE is a simple function for calculating the integer assigned
; to each color in the IDL color table.
;
; USE: result = COLORVALUE(red, green, blue), where red, green and
; blue are integers ranging from 0 to 255. Colors are determined using
; the following scale: color value = R + 256(G + 256B)).

```

```

; The user has to enter three numbers and the colorvalue is
; returned.

; Inputs:
; red: Integer value for the color red (from 0 to 255)
; green : Integer value for the color green (from 0 to 255)
; blue: Integer value for the color blue (from 0 to 255)

FUNCTION COLOR_VALUE, red, green, blue
    IF (red GT 255) OR (green GT 255) OR (blue GT 255) THEN MESSAGE, $
        'input value exceeds maximum'
    colorvalue = red + 256L*(green + 256L*blue)
    RETURN, colorvalue
END

```

A.5. Function LORENTZ

```

PRO Lorentz, x, coef, y, ypder

;PRINT, 'a: ', N_ELEMENTS(a)
;PRINT, 'x: ', N_ELEMENTS(x)

y = coef[0]/(1. + (x - coef[1])^2/coef[2]^2)

IF N_PARAMS(coef) GE 4 THEN BEGIN
    pder = FLTARR(N_ELEMENTS(x), 3)
    pder[0] = 1./(1. + x^2/coef[1]^2)
    pder[1] = 2.*coef[0]/coef[2]^2*(x - coef[1])/(1. + (x -
coef[1])^2/coef[2]^2)^2
    pder[2] = (2.*coef[0]/coef[1]^3*x^2)/(1. + x^2/coef[1]^2)
ENDIF
;PRINT, 'y: ', N_ELEMENTS(y)
END

```